On the climate variability of tropical cyclone potential intensity and Atlantic hurricane activity

by

Raphaël Rousseau-Rizzi

B.S., École Polytechnique de Montréal (2014)
M.S., McGill University (2016)

Submitted to the Department of Earth, Atmospheric and Planetary Sciences
in partial fulfillment of the requirements for the degree of

Doctor of Philosophy

at the

MASSACHUSETTS INSTITUTE OF TECHNOLOGY

June 2021

Author .....
Department of Earth, Atmospheric and Planetary Sciences
May 12, 2021

Certified by .....
Kerry Emanuel
Cecil & Ida Green Professor of Atmospheric Sciences
Thesis Supervisor

Accepted by .....
Robert D. van der Hilst
Schlumberger Professor of Earth and Planetary Sciences
Head of Department of Earth, Atmospheric, and Planetary Sciences

On the climate variability of tropical cyclone potential intensity and Atlantic hurricane activity

by

Raphaël Rousseau-Rizzi

Submitted to the Department of Earth, Atmospheric and Planetary Sciences
on May 12, 2021, in partial fulfillment of the
requirements for the degree of
Doctor of Philosophy

Abstract

From a meteorological standpoint, the most important questios one needs to answer about a given tropical cyclone is how strong the winds generated by the event can become. From a climatological standpoint, it is critical to predict tropical cyclone activity, or the collective destructive potential of all tropical cyclones in a given basin and during a given period. Potential intensity (PI) is defined as a thermodynamic bound on tropical cyclone maximum wind speeds, and is a good predictor of the intensity of a single event but also of tropical cyclone activity. As such, PI is a useful quantity to help answer both meteorological and climatological pressing questions about tropical cyclones. First, this thesis adresses recent controversies about whether the PI assumptions of inviscid free troposphere and steady-state make it inapplicable. Comparing various forms of the PI bound to the corresponding bounded quantities in low-mixing axisymmetric simulations shows that PI is in fact a valid bound on tropical cyclone intensity. Then, a categorization of definitions of tropical cyclone steady state used in the literature is introduced to clarify the conditions in which simulations can be compared to theories such as PI. It is shown that most intensity theories can be compared to the simulated period surrounding peak tropical cyclone intensity, while theories for the structure of the storm requires the simulated storm to have come into equilibrium with the surrounding environment. Next, turning to climate, a linear model for interannual basin-wide PI variations is developed, which captures almost all the PI variance in reanalysis products and provides a way to partition global and local contributions to PI variations. The model notably shows that tropical North-Atlantic PI variations over the last 40 years have been dominated by local influences. The final part of the thesis evaluates the causes of the Atlantic hurricane drought of the 1970s and 1980s. An anthropogenic nature of the hurricane drought is proposed. Concurrent hemispherically asymmetric anthropogenic sulfate emissions caused a drying of the Sahel region and enhanced the emissions of eolian dust from the Sahara and the Sahel which is shown to be detrimental to hurricane activity.

Thesis Supervisor: Kerry Emanuel
Title: Cecil & Ida Green Professor of Atmospheric Sciences

Acknowledgments

There are so many reasons to be grateful. First and foremost, I am grateful to my advisor, Kerry Emanuel, for his valuable guidance and advice and for his patience and humanity. Perhaps more importantly, I want to thank Kerry for fascinating and uniquely insightful discussions which gave the long process of this PhD its value and its flavor. I am also grateful to my committee members: Tim Cronin for his scientific and academic advice, and Amato Evan and David McGee for their insight on the causes of past and present dust variations. I especially want to thank my committee for their continued support during the past year, which was, at best, stressful and tiring for everyone. I am grateful to Richard Rotunno and George Bryan for welcoming and mentoring me during an ASP graduate student visit at NCAR. I have very fond memories of the time spent there and of working under their supervision. I also want to thank the EAPS community for providing an environment conducive to successful learning and research.

I am grateful to George Bryan for freely providing the CM1 code that was used in chapters 2 and 3, to Brian Tang for freely providing the ASPECH code used in chapter 2, and to Daniel Gilford for providing access to his ERA5 PI dataset which was used in chapter 4 of this thesis. The research presented within this thesis was funded by the Norman C. Rasmussen fellowships, the J.H. and E.V. Wade fellowships, the NSF grant AGS-1520683, the NSF grant AGS-1906768, the Office of Naval Research under grant N00014-18-1-2458 and the Natural Sciences and Engineering Research Council of Canada under grant PGSD3-490041-2016.

I want to thank my friends and colleagues at MIT and abroad for their friendship and scientific advice. In no particular order: Rohini, Julia, Tristan, Tom, Jonathan, Sydney, Henri, Lyssa, Derek, Santi, Genia, Astrid, Sam, Megan, Dan, Margaret, Diamy, Martín, Bruno, David, Katrina, Sylvester and many others all contributed to makes these five years fun and interesting.

I am grateful to my ever-supportive family Jean-Claude, Cécile, Yann et Aude for the love, the regular calls and the occasional visits, which much alleviated the distance and the effort of the PhD. Finally, I could not have done this without my partner, Florence. I am at a loss to find the right words to express how grateful I am for her patience and understanding, so I will leave it at that.

Contents

List of Figures

List of Tables

Chapter 1

Introduction

As far back as 1250, in Konungs Skuggsjá, a didactic book from the kingdom of Norway, the authors ponder the latitudinal structure of climate on a spherical Earth, hypothesizing a cold south pole and symmetry about the equator: *"And if people live as near the cold belt on the southern side as the Greenlanders do on the northern, I firmly believe that the north wind blows as warm to them as the south wind to us. For they must look north to see the midday and the sun's whole course, just as we, who dwell north of the sun, must look to the south."* Hundreds of years before notions of radiative transfer could explain their intuitions, the Norse hinted at fundamental characteristics of our planet's climate.

I like to think that not much has changed since the epoch of speculum literature. The technology and cultural knowledge available to us has dramatically increased, but the quest for understanding remains. Hence, this thesis is meant to take a very small step on the age-old path to understanding a weather phenomenon that strikes the imagination like few others: Tropical Cyclones. Tropical cyclones generate some of the most extreme weather that can be found anywhere on the planet, and strike suddenly in regions of the world where winds are otherwise generally quiescent.

1.1 Tropical Cyclones

1.1.1 General description

Tropical cyclones can be defined as low pressure systems in the tropics, which import energy by turbulent exchange from a sea surface warmer than the overlying air, and export it by radiative cooling to space. Air spiralling around the storm and near the surface is drawn radially inwards by the pressure gradient force, gaining kinetic energy until it reaches the core of the storm, constituted of a radially-sloping eyewall clouds (Houze Jr, 2010). While spiralling near the sea-surface, inflowing air loses angular momentum to the sea surface so that angular momentum in the inflow increases monotonically with radius. In the core of mature TCs, air parcels ascend in a saturated environment, conserving moist entropy and angular momentum. The low values of angular momentum of the ascending air lead to a reversal of the circulation from cyclonic to anticyclonic as the air outflows from the storm at high levels. The outflowing air cools radiatively to space and, on a timescale of a few tens of days, it subsides back towards the surface. Assuming that tropical cyclones are axisymmetric, which they can nearly be (Knaff et al., 2003), the circulation around the cyclones can partitioned into two interdependent components; a primary circulation, spiralling in the horizontal $r - \theta$ plane, and a secondary circulation in the vertical $r - z$ plane. An artist rendition of both circulations along with a contour of the clouds associated with the circulation are drawn in Fig.1-1.

1.1.2 Potential intensity

Similarly to heat engines, the amount of kinetic energy a tropical cyclone can generate is a function of the energy transfer through the system (Emanuel, 1988) and of the temperature difference between hot and cold reservoirs. Based on this idea, one can derive a thermodynamic bound on the maximum wind speeds called poten-

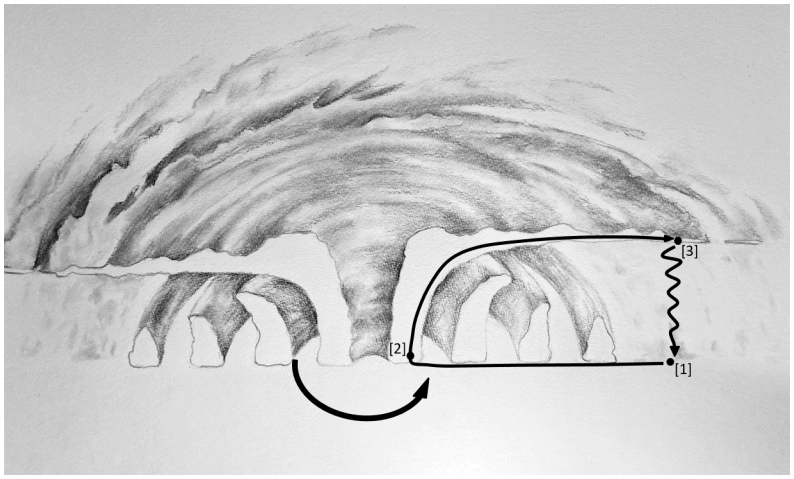

Figure 1-1: Vertical cross section of tropical cyclone clouds, with arrows representing the primary (horizontal plane) and secondary (vertical plane) circulations.

tial intensity. An important control on the rate of energy input to the TC system, and hence on potential intensity, is the enthalpy difference between the sea-surface and the overlying air - or thermodynamic disequilibrium. In general, the larger the temperature difference between the ocean and the surface air, the larger the thermodynamic disequilibrium and the stronger the tropical cyclone can be (Emanuel, 1988).

The tropics are characterized by strong solar radiation, and weak lateral atmospheric energy transport and for that reason, on average, the region can reasonably be assumed to be in a state of radiative-convective equilibrium (RCE, Manabe and Strickler, 1964). In that state, radiative flux divergence in the vertical is balanced by convective heating, and the net radiative heating of the surface is balanced by environmental turbulent enthalpy fluxes. All else equal, the thermodynamic disequilibrium upon which the intensity of tropical cyclones depends is proportional to those environmental turbulent fluxes (Emanuel, 2007). Hence, a change in the net radiative heating of the surface results in a change in the maximum intensity achievable by tropical cyclones, which is why the increasing greenhouse gases in the atmosphere risk increasing the intensity of tropical cyclones (Knutson et al., 2010). The tropics are also characterized by weak values of the coriolis parameter which mean that inertial-gravity waves can propagate very far from their source and that the mid-tropospheric temperature in

the tropics is more or less horizontally uniform (WTG, Sobel and Bretherton, 2000). This constrains the values of enthalpy in the atmospheric boundary layer and means that the near-surface thermodynamic disequilibrium is much more sensitive to local changes in sea-surface temperature than to tropics-wide changes. For that reason, tropical cyclone potential intensity is very sensitive to local changes in sea-surface temperature. Since tropical cyclone activity in a given basin depends on potential intensity, to understand why TC activity varies, one needs to understand what causes the SST to vary locally. For example, understanding the compared effects of ocean heat flux convergence, environmental near surface winds or local aerosol loading on SST is critical to identifying the causes of TC activity variability. Dust aerosol loading over the Atlantic ocean is one such local aerosol which has large effects on TC activity (e.g., Strong et al., 2018).

1.2 Chapter descriptions

In chapter 2, I evaluate the validity of potential intensity theories bounding the magnitude of the surface winds, the azimuthal winds and the gradient winds, by comparing the PI bounds in numerical simulations to the corresponding numerically simulated intensities. Reconciling PI theories with idealized numerical models is key to understanding the mechanism controlling TC maximum intensity, and to improving numerical predictions of tropical cyclones, the skill of which has been stagnating in recent years (e.g., DeMaria et al., 2014). This evaluation is rendered necessary by the results of Hausman (2001) and Persing and Montgomery (2003) who reported that, in high resolution and low-mixing axisymmetric simulations, the simulated wind speeds greatly exceeded potential intensity. This phenomenon was called superintensity and cast doubt on the validity of PI as a bound on wind speed. In this chapter, I find PI to be valid so long as it is compared to the correspondingly defined intensity. This chapter was published by Rousseau-Rizzi and Emanuel (2019) in the Journal of the Atmospheric Sciences. [1] Some follow-up work was included in reponse to comments

[1] Chapter 2 is an edited version of: Rousseau-Rizzi, R., and K. Emanuel, 2019: An evaluation of hurricane superintensity in axisymmetric numerical models. *Journal of the Atmospheric Sciences*,

on that paper (Rousseau-Rizzi and Emanuel, 2020; Emanuel and Rousseau-Rizzi, 2020), but will not be included in this thesis.

In chapter 3, I establish the meaning of steady state in simulated tropical cyclones. Previous work has argued that simulated TCs reach steady state after a few tens of days and cannot be accurately compared to analytical theories at earlier times (Hakim, 2011). This would imply that analytical theories are of limited use in understanding real TCs, which seldom live more than three weeks. Other research has argued that simulated TCs decay by "running out" of angular momentum and infer that real TCs never reach a steady state (Smith et al., 2014). In this chapter, I disambiguate the concept of steady-state in TC simulations by introducing two phenomenological definitions of steady state; one that only requires the core to evolve slowly, which is reached after a few days, and the second which requires the entire TC-environment system to reach equilibrium, which takes tens of days to achieve. Theories that only require steady-state in the core, like PI theories can readily be compared to the first definition, while theories on the steady-state structure of TCs need to be compared to the second definition. I also find that the decay in simulated TCs is not due to a decrease in available angular momentum, but to a decrease in mid-tropospheric environmental entropy. This chapter was published by Rousseau-Rizzi et al. (2021) in the Journal of the Atmospheric Sciences. [2]

Because it limits the maximum wind speeds of TCs, potential intensity is an important predictor of TC activity and of their destructive potential. Hence, to help understand past variations in TC activity, after establishing the validity and domain of applicability of PI theories, in chapter 4, I focus on understanding its climate variability. To do so, I introduce a linear model for PI variations based on two predictors; tropospheric saturation moist static energy, and sea-surface temperature. Assuming

76 (6), 1697–1708.

[2]Chapter 3 is an edited version of: Rousseau-Rizzi, R., R. Rotunno, and G. Bryan, 2021: A thermodynamic perspective on steady-state tropical cyclones. *Journal of the Atmospheric Sciences*, **78 (2)**, 583-593.

that the tropics are on average in a state of radiative-convective equilibrium (RCE), and that horizontal temperature gradients are weak (WTG, Sobel and Bretherton, 2000), variations of the predictors can be partitioned between a correlated component, which is coherent with a variation of the mean state of the tropics, and a decorrelated component, which represents a departure from the RCE state. This in turn allows one to partition PI variations between global forcing and local environmental changes. The linear model explains between 80% and 96% of the interannual PI variance depending on the ocean basin, and shows that, over the last 40 years the contribution of global change has contributed to less than 10% of the North-Atlantic main development region PI variability. I am currently addressing revisions for publishing this chapter in the Journal of Climate.

Having established that local environmental changes are the main driver of recent main development region North-Atlantic PI changes, in chapter 5, I set to understand the local causes of the large Atlantic hurricane activity variations of the recent decades, by understanding local SST anomaly variations. Our goal is to establish whether those variations were due to natural basin-scale variability, or to anthropogenic influences. To that end, I build upon the existing literature which establishes 1) that past Atlantic hurricane variability was in great part controlled by eolian Saharan dust variability (Strong et al., 2018), 2) that Saharan dust lofting and transport correlates well with drought conditions in the Sahel (Prospero et al., 2014) and 3) that the ultimate cause of drought conditions in the Sahel is hemispherically asymmetric sulfate forcing of anthropogenic and volcanic origin (Ackerley et al., 2011; Haywood et al., 2013). I show that the slowest mode of variability of SST in the North-Atlantic, apart from the global warming, is consistent with the so-called Atlantic Multidecadal Oscillation, a mode of variability once believed to be natural and now known to be forced by sulfate aerosols (Bellomo et al., 2018). In addition, this slow mode is consistent with dry conditions over the Sahel and dusty conditions over the Atlantic. I estimate that 40% of the multidecadal SST anomaly variations can be explained by summer dust aerosol direct effect variations. I conclude that dust

cannot be neglected when modelling climate variability of TC activity, and nor can the anthropogenic drivers of dust variability. This chapter is in preparation for publication.

Finally, chapter 6 outlines the key results from the thesis and proposes future avenues of research arising from the results of chapters 2 to 5.

Chapter 2

An Evaluation of Hurricane Superintensity in Axisymmetric Numerical Models

Abstract

Potential intensity (PI) is an analytical bound on steady, inviscid, axisymmetric hurricane wind speed. Studies have shown that simulated hurricane azimuthal wind speed can greatly exceed a potential intensity (PI) bound on the maximum gradient wind. This disparity is called superintensity (SI) and has been attributed to the contribution of the unbalanced flow to the azimuthal wind. The goals of this chapter are 1) to introduce a new surface wind PI (PI_s), based on a differential Carnot cycle and bounding the magnitude of the surface winds, 2) to evaluate SI in numerical simulations with respect to diagnostic PI bounds on gradient wind (PI_g), azimuthal wind (PI_a) and surface wind (PI_s) and 3) to evaluate the validity of each PI bound based on the SI computations. Here, we define superintensity as the normalized amount by which each version of PI is exceeded by the quantity it bounds. Axisymmetric tropical cyclone simulations are performed while varying the parameterized turbulent mixing as a way of estimating SI in the inviscid limit. As the mixing length decreases, all three bounded wind speeds increase similarly from a sub-PI state to a marginally superintense state. This shows that all three forms of PI evaluated here are good approximations to their respective metrics in numerical simulations.

2.1 Introduction

2.1.1 Definition and relevance of superintensity

Tropical cyclones (TC), or hurricanes, are the single most destructive natural disaster in the US, with a cumulative damage cost of $265 billion for 2017 alone (Office For Coastal Management, 2018). While our ability to forecast hurricane intensity (wind speed) has generally improved along with track forecasting, over the last 25 years, 24-h lead time forecast skill has improved very slowly (DeMaria et al., 2014). In addition, it has been hypothesized that the forecasting of TC intensity with climate change will become more difficult as the intensification rates are expected to increase (Emanuel, 2017).

TCs are a complex phenomenon and, while our understanding of the underlying physics has made large and regular progress over the last three decades, discrepancies remain between analytical theories, numerical models and observations. In that context, we must strive to reconcile analytical hurricane intensity theories with both hurricane data and numerical simulations. This is a necessary step in understanding the mechanisms of intensification and improving forecast models.

Analytical theories for hurricane intensity include the concept of potential intensity (PI), a theoretical upper bound on inviscid, steady state and axisymmetric hurricane wind speed. PI can be defined to bound various quantities such as the gradient wind (Emanuel, 1986), the azimuthal wind (Bryan and Rotunno, 2009a) and the magnitude of the surface winds (Bister and Emanuel, 1998). Each form of PI can be considered to represent a different simplified picture of the relation between the TC dynamics and thermodynamics.

Gradient wind balance is defined as the state in which the Coriolis and centrifugal accelerations balance the pressure gradient acceleration in the radial momentum equation; that is, the system is in steady state and the diffusive and advective terms

are negligible. Under the assumption that TCs are in gradient wind balance, gradient wind PI (PI_g, arguably the most widespread PI theory) should also bound the maximum azimuthal winds for any given storm. And indeed, gradient wind PI has been shown to be generally well respected in nature (Emanuel, 2000). However, the maximum azimuthal wind speeds within a few strong storms have been observed to exceed the PI_g bound (Montgomery et al., 2006).

One of the main inconsistencies between numerical models and analytical theories that has been discussed in the literature is called superintensity (Persing and Montgomery, 2003). Superintensity (SI) as defined by Persing and Montgomery (2003) occurs when the maximum steady-state azimuthal wind speed of a tropical cyclone exceeds the gradient wind potential intensity, sometimes greatly. An alternative definition of SI will be introduced and used later in this chapter. Superintensity has mostly been studied in axisymmetric numerical models, which are easier to use and compare more directly to PI theory than 3D numerical models.

In a sensitivity study, Hausman (2001) noticed that increasing the resolution in axisymmetric hurricane models was associated with azimuthal wind speed increasing beyond observed values for a similar environment. The subsequent study by Persing and Montgomery (2003) sought to understand this discrepancy and, noting that the simulated winds well exceeded PI_g, they coined the term superintensity. Their explanation, that the import of high entropy air from the eye into the eyewall was responsible for the high intensity, was later shown by Bryan and Rotunno (2009b) not to be the dominant factor in SI. The work on SI by Bryan and Rotunno is very relevant to this chapter and hereafter their papers will be referred to as BR09a,b,c.

Using the CM1 model (Bryan and Fritsch, 2002), Bryan and Rotunno (2009a) showed hurricane intensity (and superintensity) to be very sensitive to the parameterized mixing of enthalpy and momentum. Other studies with CM1, including Bryan and Rotunno (2009c), Rotunno and Bryan (2012), and Bryan (2012) found that the inten-

sity of simulated axisymmetric TCs increased significantly with decreasing horizontal mixing length (l_h). The mixing length l_h influences the magnitude of the horizontal mixing following the parameterization introduced in Rotunno and Emanuel (1987) (hereafter RE87) axisymmetric TC model and based on the Smagorinsky (1963) turbulence parameterization. Keeping the environment and all other parameters fixed, BR09a found that decreasing l_h from values of about 3000 m to 125 m increases the TC azimuthal wind from less than PI_g to 150% of PI_g. Note that, according to the PI assumption of inviscid flow, the intensity of the simulated TCs should converge to PI when l_h decreases, and not exceed it. The sensitivity of azimuthal wind to l_h can be likened to the sensitivity to resolution reported by Hausman (2001). Indeed, lower mixing and, to a certain extent, higher resolution are both associated with stronger radial gradients of entropy, and thus intensity.

BR09a found the gradient wind balance assumption in the Gradient PI (PI_g) theory to be clearly violated in their simulations. This means that superintensity of the azimuthal winds with respect to the gradient wind PI (PI_g) occurs because of gradient wind imbalance, namely supergradient flow. Using methods by Lilly (unpublished manuscript) and Bister and Emanuel (1998), BR09a derived a PI expression based on both thermodynamic and dynamic diagnostics to account for the contribution of unbalanced winds in PI. This expression provides a good upper bound on the azimuthal wind (called $PI+$ in BR09a and PI_a hereafter). While bounds on the gradient wind can be computed a priori, from the environment alone, including agradient winds makes it very difficult to bound the azimuthal wind from the environment only, so that it can only be evaluated diagnostically.

To summarize, BR09a show that, in the early studies of Hausman (2001) and Persing and Montgomery (2003), SI was largely due to supergradient effects. They then explain why PI_g seems to work in constraining the observed azimuthal winds of tropical cyclones.

Willoughby (1990) showed that the azimuthal mean winds of certain observed TCs are very close to gradient wind balance above the frictional layer. This agrees with Emanuel's 1986 assumption of thermal wind balance above the boundary layer, but not with simulations, if we assume that the TCs are inviscid. BR09a reconcile this disparity by pointing out that the TCs are indeed not inviscid and that horizontal mixing tends to weaken the storm and favor gradient wind balance. 3D turbulence has been shown to become important in intense storms, which limits the increase in mean azimuthal wind velocity (e.g., Rotunno et al., 2009; Yang et al., 2007; Brown and Hakim, 2013). However, even with an increase in three-dimensional turbulent mixing, some storms are observed to have winds that are supergradient by up to 10 m s^{-1} (Kepert, 2006), which could explain the observed superintensity.

To summarize, studies evaluating PI have done so for gradient wind PI and azimuthal wind PI in low mixing environments. The PI_g bound was shown not to work very well for azimuthal winds and for small mixing lengths, but to work well for gradient winds, outlining the fact that TC intensities should be compared to the appropriate PI bound. Hereafter, SI will be defined as the discrepancy between a given form of PI and the numerically simulated intensity it bounds, and will be used to evaluate various PI theories in the same simulations.

Generally, SI in numerical models implies that there is a limitation either with the PI bound or with the way hurricanes are represented in current models. In this chapter, we will use SI to evaluate the different representations of the TC physics associated with various forms of PI, assuming that the contribution from numerical errors is negligible. The possible contribution of model numerics or parameterizations to SI is deferred to future research.

2.1.2 New and existing forms of PI

This chapter aims to evaluate both new and existing forms of PI in numerical simulations. Section 2.2 introduces a new derivation (briefly described in Emanuel, 2018)

for a PI bound on the maximum surface winds, similar to the one derived in Bister and Emanuel (1998). This new surface PI (PI_s) is derived with as few assumptions as possible, using the concept of a differential Carnot cycle. It provides a thermodynamic bound on the magnitude of the surface winds including the radial inflow component. The expressions for gradient wind PI and azimuthal wind PI introduced respectively by Emanuel (1986) and BR09a will be evaluated as well. A short derivation of these two forms follows, while the third, new form is derived in Section 2.

2.1.3 Gradient wind PI

The most widely used analytical model of hurricane energetics was first published in Emanuel (1986). This steady state, inviscid, axisymmetric model provides the basis of what is now called potential intensity using: 1) The assumption of moist slantwise neutrality, 2) the assumption of thermal wind balance (hydrostatic and gradient wind balance combined) and 3) a boundary layer closure. The gradient wind (V_g) is defined as the azimuthal wind required so that the sum of the Coriolis and centrifugal accelerations balance the radial pressure gradient acceleration. Assuming moist slantwise neutrality is equivalent to assuming that the angular momentum (M) surfaces coincide with the saturation entropy (s^*) surfaces, neglecting the direct contribution of variable water content to density. The angular momentum is given by $M = Vr + 1/2fr^2$, where V is the azimuthal velocity (here, $V = V_g$), r is the radius and f is a constant Coriolis parameter. In Emanuel (1986), the thermal wind relation is given by

$$\frac{1}{r^3}\Big(\frac{\partial M^2}{\partial p}\Big)_r = -\Big(\frac{\partial T}{\partial p}\Big)_{s^*}\Big(\frac{\partial s^*}{\partial r}\Big)_p \tag{2.1}$$

where the subscripts denote quantities being held constant. Moist slantwise neutrality allows us to integrate Eq. (2.1) upwards along surfaces of constant angular momentum, between the top of the boundary layer and the outflow, defined as the point where the azimuthal velocity vanishes. This yields

$$\frac{V_{g,b}}{r_b} = -\frac{ds^*}{dM}(T_b - T_{out}) \tag{2.2}$$

where subscript b denotes the top of the boundary layer and subscript *out* denotes the outflow layer. Equation (2.1) indicates that the vertical shear is monotonic with T so that the maximum velocity occurs at the top of the boundary layer. This means that $V_{g,b}$ is an upper bound on the gradient wind. From there, ds^*/dM has to be defined to get a diagnostic equation for maximum velocity. The boundary layer (BL) closure states that ds/dM in the BL is the ratio of the surface fluxes of entropy (F_s) and angular momentum ($\bar{r}\tau_\theta$). Further, $ds^*/dM = ds/dM$ at the top of the BL, so that

$$\frac{ds^*}{dM} = \frac{F_s}{\bar{r}\tau_\theta} \tag{2.3}$$

where $\bar{r}$ is the vertically averaged radius of angular momentum surfaces. We need to account for dissipative heating in the boundary layer because the inviscid assumption is only applied to the interior flow, and because the numerical models used in this chapter include dissipative heating parameterizations. We obtain

$$F_s = \frac{\rho}{T_s}(C_{k10}|\mathbf{V_{10}}|(k_s^* - k_{10}) + C_{D10}|\mathbf{V_{10}}|^3) \tag{2.4}$$

$$\tau_\theta = -\rho C_{D10}|\mathbf{V_{10}}|V_{10}. \tag{2.5}$$

In these equations, the subscript 10 designates the near surface layer at 10 m above the air-sea interface. $|\mathbf{V_{10}}|$ is the magnitude of the surface winds. C_{k10} and C_{D10} are the bulk aerodynamic flux coefficients for enthalpy and momentum. $k = (c_p + q_t c_l)T + L_v q$ is the enthalpy, where q is the water vapor mixing ratio and q_t is the total water mixing ratio. k_s^* is the saturation enthalpy at sea surface temperature (T_s). We note that, for adiabatic and hydrostatic transformations, the enthalpy difference $(k_s^* - k_{10})$ is equivalent to the moist static energy (MSE) difference $(h_s^* - h_b)$ between the top of the boundary layer (h_b) and the surface temperature saturated state (h_s^*).

The MSE is given by $h = k + (1 + q_t)gz$. Next, Eqs. (2.3), (2.4) and (2.5) are substituted into Eq. (2.2). Assuming that the radius of the angular momentum surfaces is similar at the top and at the bottom of the boundary layer, we get

$$V_{g,b} = \frac{1}{V_{10}} \frac{r_b}{\bar{r}} \frac{(T_b - T_{out})}{T_s} \Big(\frac{C_{k10}}{C_{D10}} (k_s^* - k_{10}) + |\mathbf{V_{10}}|^2 \Big). \tag{2.6}$$

Then, following Bister and Emanuel (1998), we assume that the momentum near the surface equals that at the top of the boundary layer ($V_{10} \approx V_{g,b}$, and $\bar{r} \approx r_b$), that $T_s \approx T_b$ and finally, that the dissipative heating effects can be properly captured by setting $|\mathbf{V_{10}}|^2 \approx V_{g,b}^2$. These assumptions allow us to simplify the equation further and obtain

$$PI_g^2 = V_{g,b}^2 = \frac{C_{k10}}{C_{D10}} \frac{(T_b - T_{out})}{T_{out}} (k_s^* - k_{10}) \tag{2.7}$$

where we have redefined $V_{g,b}$ as PI_g, which denotes a potential intensity derived from dynamical principles, that represents an upper bound on gradient wind (V_g). The validity of the simplifying approximations will be evaluated in the results section.

2.1.4 Azimuthal wind PI

Using the same boundary layer closure assumptions as in the PI_g derivation, along with the assumption that $M_b \approx V_b r_b$ in the inner core, the BR09a equation that accounts for the supergradient contribution is written

$$PI_a^2 = V_{max}^2 = PI_g^2 + r_b \eta_b w_b \frac{T_s}{T_o} \tag{2.8}$$

where r_b, η_b and w_b are the radius, the azimuthal vorticity and the vertical velocity at the location of maximum winds. PI_a represents a bound on the maximum azimuthal wind.

2.1.5 Objectives

In summary, the main purpose of this chapter is to introduce a new derivation for surface PI (hereafter PI_s), based on the idea of a differential Carnot cycle and bounding the magnitude of the surface winds, and to evaluate this theory along with previous PI theories bounding the azimuthal winds and the gradient winds, by comparing them to numerically simulated values.

First, section 2.2 introduces the derivation of the surface PI based on a differential Carnot engine view of the TC. Then, section 2.3 presents the model and simulation setup to investigate SI, and section 2.4 shows the results of these computations. Finally, section 2.5 compares the degree of superintensity for all forms of PI and all simulations.

2.2 Surface PI

The energy cycle of a hurricane can be described in terms of a Carnot heat engine (Emanuel, 1986; Pauluis and Zhang, 2017; Emanuel, 2018), which provides an integral constraint on the maximum surface winds. Here we derive a local constraint by differentiating two adjacent cycles as shown in Figure 2-1. The advantage of using a differential Carnot cycle instead of approximating the secondary circulation of the hurricane as a full Carnot cycle is twofold. First, it provides an expression for the maximum surface winds rather than an integral constraint on the surface winds for the whole storm. Second, it does not require the entire secondary circulation of the hurricane to satisfy the Carnot cycle's assumptions, but only the portion of the cycle located in the eyewall. Hakim (2011) showed that the secondary circulation of a simulated axisymmetric TC corresponds approximately to a Carnot cycle in the inflow and in the eyewall, but not in the outflow and subsidence regions.

In Figure 2-1, Cycle 1 begins at point A very near the surface in the boundary layer far outside the core and follows the spiraling inflow to point B incrementally

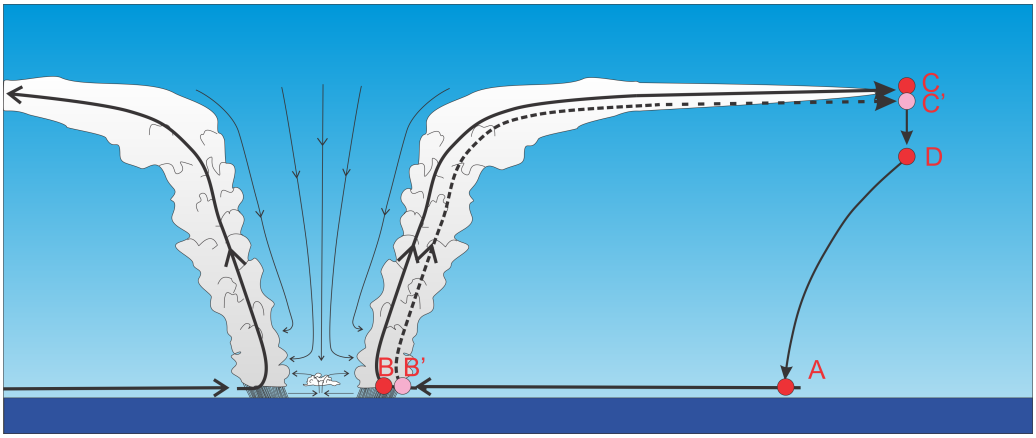

Figure 2-1: Showing two adjacent heat cycles of an axisymmetric, steady hurricane. Cycle 1 is defined as A-B-C-D-A, and cycle 2 is defined as A-B'-C'-D-A.

inside the radius of maximum winds. This leg is approximated as isothermal, with strong input of enthalpy from the ocean and strong dissipation of kinetic energy. From B the cycle follows air upward in the eyewall, and outward to point C, far outside the storm center; this leg is approximated as moist adiabatic and at constant energy and angular momentum. From point C, air sinks to point D while losing entropy and energy owing to radiative cooling; point D is chosen as a point in the environment that has the same moist entropy as point A. Leg C-D is approximated as isothermal, and angular momentum is regained along this leg, presumably owing to irreversible mixing. From D, the parcel sinks at constant angular momentum back to point A. In the upper part of this leg, air loses entropy though radiative cooling, but regains it through irreversible mixing as it approaches A. Cycle 2 is identical to Cycle 1 except that the air turns upward in the eyewall at point B' just outside the radius of maximum winds, and follows a streamline and angular momentum surface to point C' just under point C, but then sinking to point D and back to its starting point A. We can take points A and D to be the same in each cycle because they are in regions of very weak spatial gradients of entropy and angular momentum. Both legs B-C and B'-C' are considered to occur at water saturation. A Carnot-like relationship between entropy gained in A-B (and lost in C-D) and mechanical dissipation can be derived from equations for conservation of moist entropy, s and energy. We begin with by differentiating (following a parcel) the reversible moist entropy using its definition in

Emanuel (1994):

$$T\frac{ds}{dt} = \left(c_{pd} + c_l q_t\right)\frac{dT}{dt} + \frac{d\left(L_v q\right)}{dt} - \left(1 + q_t\right)\alpha\frac{dp}{dt} - R_v T \ln\left(\mathcal{H}\right)\frac{dq_t}{dt}, \tag{2.9}$$

where T is temperature, p is pressure, q is the vapor mixing ratio, q_t is the total water mixing ratio, α is the specific volume, c_{pd} is the specific heat capacity of dry air, c_l is the heat capacity of liquid water, L_v is the latent heat of vaporization, R_v is the gas constant for water vapor, and $\mathcal{H}$ is the relative humidity. The last term in (2.9) is an irreversible source of entropy. Note that we neglect the ice phase here; including it would add terms related to thermodynamically irreversible ice-phase effects such as supercooling. By taking the dot product of the vector momentum equation with the three-dimensional velocity vector, we obtain a relationship for the kinetic energy:

$$\frac{d}{dt}\left(\frac{1}{2}|\mathbf{V}|^2\right) = -\alpha\frac{dp}{dt} + \mathbf{V}\cdot\mathbf{F} - wg, \tag{2.10}$$

where $\mathbf{V}$ is the three-dimensional velocity, w is its vertical component, g is the acceleration of gravity, and $\mathbf{F}$ is the frictional source of momentum. Eliminating pressure p between (2.9) and (2.10) yields

$$T\frac{ds}{dt} = \frac{d}{dt}\left[\left(c_{pd} + c_l q_t\right)T + L_v q + \left(1 + q_t\right)\left(\frac{1}{2}|\mathbf{V}|^2 + gz\right)\right] - \mathbf{V}\cdot\mathbf{F} - \frac{dq_t}{dt}\left[R_v T\ln(\mathcal{H}) + \frac{1}{2}|\mathbf{V}|^2 + gz\right]. \tag{2.11}$$

We next integrate (2.11) around either A-B-C-D-A or A-B'-C'-D-A to obtain

$$\oint T\frac{ds}{dt} = -\oint \mathbf{V}\cdot\mathbf{F} - \oint \frac{dq_t}{dt}\left[R_v T\ln(\mathcal{H}) + \frac{1}{2}|\mathbf{V}|^2 + gz\right]. \tag{2.12}$$

The first term on the right side of (2.11) is a perfect derivative and thus integrates to zero around a closed loop. If we apply (2.12) first to the loop A-B-C-D-A and subtract that from its application to A-B'-C'-D-A. we get a closed integral around the loop B'-B-C-C'-B':

$$\oint\limits_{inner} T\frac{ds}{dt} = -\oint\limits_{inner} \mathbf{V}\,.\,\mathbf{F} - \oint\limits_{inner} \frac{dq_t}{dt}\left[\frac{1}{2}|\mathbf{V}|^2 + gz\right]. \tag{2.13}$$

The $\ln(\mathcal{H})$ is not present as the inner loop is taken to be saturated. The last term in (2.13) represents the irreversible entropy loss associated with lifting water mass against gravity and changing its kinetic energy. It is quantitatively small compared to the other terms in (2.13) and we henceforth neglect it, thus we will evaluate

$$\oint\limits_{inner} T\frac{ds}{dt} = -\oint\limits_{inner} \mathbf{V}\,.\,\mathbf{F} \tag{2.14}$$

where the *inner* notation denotes the circuit B'-B-C-C'-B'. We note that B-C and C'-B' are adiabatic, and we assume that friction is only important in B'-B. (Emanuel, 1986, showed that there must also be frictional dissipation in the leg C-C' associated with a gain of angular momentum, but this will be small if the radius at which this occurs is not too large.) Using classical aerodynamic flux formulae for the sea surface source of enthalpy and sink of momentum, and taking the circuit B'-B-C-C'-B' to be of infinitesimal width yields

$$\frac{T_s - T_{out}}{T_s}\left[C_{k10}|\mathbf{V}_{10}|\,(k_0^* - k_{10}) + C_{D10}|\mathbf{V}_{10}|^3\right] = C_{D10}|\mathbf{V}_{10}|^3, \tag{2.15}$$

where $|\mathbf{V}_{10}|$ is now the 10 m wind speed at the radius of maximum winds, the exchange coefficients pertain to 10 m altitude, T_s is the surface temperature, T_{out} is the temperature at C-C', k_s^* is the saturation enthalpy of the sea surface, and k_{10} is the enthalpy at 10 m. Rearranging (2.15) yields an expression for what we refer to as the surface PI, or :

PI Form	Variable	Diagnostic	SI Definition
PI_g	V_g	$PI_g^2 = \frac{C_{k10}}{C_{D10}} \frac{(T_b - T_{out})}{T_{out}} (k_s^* - k_{10})$	$SI_g = \frac{(\max(V_g) - PI_g)}{PI_g}$
PI_a	V	$PI_a^2 = PI_g^2 + r_b \eta_b w_b \frac{T_s}{T_o}$	$SI_a = \frac{(\max(V) - PI_a)}{PI_a}$
PI_s	$\lvert\mathbf{V_{10}}\rvert$	$PI_s^2 = \frac{C_{k10}}{C_{D10}} \frac{(T_s - T_{out})}{T_{out}} (k_s^* - k_{10})$	$SI_s = \frac{(\max(\lvert\mathbf{V_{10}}\rvert) - PI_s)}{PI_s}$

Table 2.1: Summary of the variables bounded, the diagnostic formulas and the SI definitions for each form of PI.

$$PI_s^2 = |\mathbf{V_{10}}|^2 = \frac{C_{k10}}{C_{D10}} \frac{(T_s - T_{out})}{T_{out}} (k_s^* - k_{10}). \tag{2.16}$$

No assumptions of gradient wind or hydrostatic balance have been made here. Note that the expression for PI_s is almost identical to that for PI_g, the only difference being that T_s appears instead of T_b, in the numerator of the thermodynamic efficiency ratio.

Summarizing the different versions of PI we will be using in this chapter: PI_s puts an upper bound on the magnitude of the surface winds, PI_a bounds the maximum azimuthal winds and PI_g bounds the maximum gradient winds. Similarly, we will denote superintensity by SI_s, SI_a and SI_g representing the amount by which the maximum winds exceed each version of PI. In this chapter, superintensity will be computed as a relative, normalized quantity so that, for example, $SI_s = (\max(|\mathbf{V_{10}}|) - PI_s)/PI_s$. Hereafter $|\mathbf{V_{10}}|$ refers to simulation data. Table 2.1 summarizes the forms of PI that will be evaluated in this chapter.

2.3 Numerical simulations

The simulations in this chapter are conducted using two axisymmetric models, namely ASPECH (Tang and Emanuel, 2012) and CM1 version 19, in an axisymmetric configuration (BR09c). Both models' equation sets conserve mass and internal energy in saturated air and include dissipative heating. Most previous SI studies used CM1 but we add in another model to assess the degree to which superintense behavior may be

model dependent. Similarly to RE87, in both models the radiation is parameterized by a simple Newtonian relaxation of potential temperature to the background, which is capped at 2 K per day cooling. For simplicity, surface exchange coefficients are fixed to $C_{k10}/C_{D10} = 1$ with $C_{D10} = 0.002$ and $C_{k10} = 0.002$. C_{D10} is similar to the values used in most models for high wind speeds, but the value of $C_{k10} = 0.002$ resulting from these choices is much higher than that generally considered to be most representative of intense hurricanes ($C_{k10} = 0.0012$). This choice was partly motivated by the desire to simulate high intensity storms, more likely to exhibit superintensity. The domains are 1500 km $\times$ 27 km, with a horizontal grid spacing of 2 km for the inner 300 km stretching to 8 km at the edge of the domain. The vertical grid spacing is 300 m for the lower 15 km, stretching to 500 m at the top of the domain in ASPECH, and is uniformly 300 m in CM1. This resolution, lower than has been used for the CM1 simulations in BR09a, was chosen for ease of comparison with ASPECH, a somewhat computationally slower model.

The initial vortex, in both simulations, is defined to have a maximum wind speed of 15 m s^{-1} at a height of 1 km and a radius of 100 km. The vertical extent of the vortex is 15 km and the radius of zero winds is 500 km. The microphysical parameterization used in both models is the simple liquid water scheme used in RE87 with a terminal velocity of $v_t = 7$ m s^{-1}. BR09c showed that hurricane maximum intensity is very sensitive to terminal velocity and that $v_t = 7$ m s^{-1} yields intensities similar to (but somewhat lower than) the pseudoadiabatic limit. Unless specified otherwise, the asymptotic vertical mixing length is $l_v = 100$ m. To ensure that conditional instability is small, the simulations are initialized with the RE87 sounding made available by George Bryan[1], which is essentially neutral. The sea surface temperature T_s is 27 ^{o}C in all simulations, with an initial air-sea temperature difference at 10-m of about 3.5 ^{o}C.

[1] `http://www2.mmm.ucar.edu/people/bryan/cm1/soundings/input_sounding_rotunno_emanuel`

2.3.1 Sensitivity studies

The goal of the sensitivity analysis is to push the models from a state where the simulated intensities (gradient, azimuthal and surface winds) do not reach their respective PI bounds, to a superintense state. To do so, we decrease the horizontal mixing length l_h by factors of two over six simulations from $l_h = 2000$ m to $l_h = 62.5$ m. Decreasing l_h decreases the mixing rate of enthalpy and momentum and allows for stronger gradients to form, which in turn leads to more intense hurricanes.

2.3.2 In situ estimation of PI

Diagnostics of a given form of PI are realized in situ at the location where the value bounded by that form of PI is maximum. For example, PI_s is computed using using equation (2.16) at the radius of maximum surface winds. The thermodynamic disequilibrium is computed as the difference between the surface saturation MSE and the boundary layer MSE, here taken at the first model level (at a height of 150 m). The outflow temperature is taken at the point where the azimuthal velocity changes sign when ascending along a streamline from the PI evaluation point.

2.4 Results

First, Fig. 2-2 shows time series of the instantaneous maximum azimuthal velocity for all simulations of the l_h sensitivity experiment and for both models. The time series of both models are qualitatively similar with the exception of an initially faster spinup rate in CM1. Since we are concerned with the steady state only, this does not make much difference in the analysis. Consistent with previous studies (e.g. Bryan and Rotunno, 2009a,c; Rotunno and Bryan, 2012; Bryan, 2012), it is clear that as the mixing length decreases, the maximum intensity increases.

Next, in Fig. 2-3, we show again the ASPECH maximum azimuthal velocity time series for $l_h = 2000$ m and $l_h = 63$ m alongside time series of diagnosed PI_g and

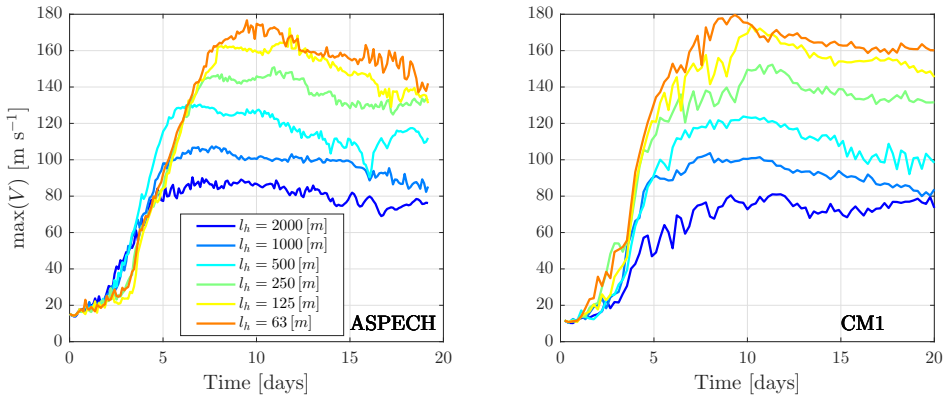

Figure 2-2: Time series of the maximum azimuthal wind, V, in ASPECH (left) and CM1 (right) simulations for all values of l_h (color scale; the warmer colors correspond to smaller l_h).

PI_a for the same simulations. Consistent with BR09a and because of supergradient flow, $max(V) > PI_g$, with the difference increasing at small mixing lengths. Again consistent with BR09a, PI_a clearly represents a much better bound on max(V), as it is barely exceeded, even at small l_h. The difference between max(V) and PI_g in Fig. 2-3 represents the definition of SI used in previous studies. Again, here we aim at comparing PI bounds against the appropriate quantity, so that we define $SI_g = (\max(V_g) - PI_g)/PI_g$, the superintensity with respect to the gradient wind PI.

BR09a showed that gradient winds computed from the radial momentum equation in low-mixing TCs will tend to be overestimated since the pressure gradient includes a perturbation due to the unbalanced wind contribution. This computation will thus also overestimate SI_g. Throughout this chapter, V_g will instead be computed using BR09a's Eq.16 (Emanuel's 1986 Eq.11)

$$r^2|_{M_g} = -M\left[\frac{ds}{dM}(T - T_{out})\right]^{-1}, \tag{2.17}$$

where the variables on the right hand side are taken along the angular momentum surface passing through the position of maximum winds. The radius computed on the left hand side can then be considered as the radius this angular momentum surface would have if it were actually balanced. The velocity of air with the same angular

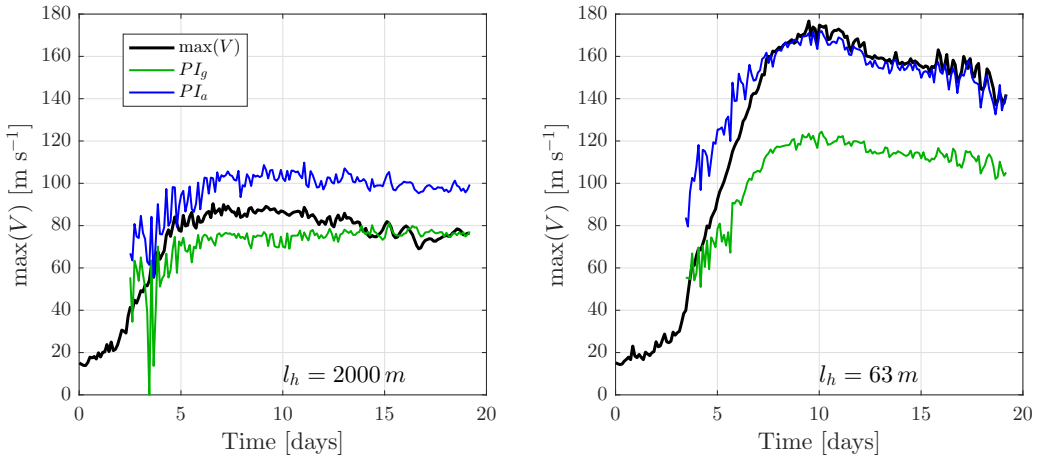

Figure 2-3: Time series of the maximum azimuthal velocity, V (black), the gradient potential intensity, PI_g, (green) and the azimuthal potential intensity, PI_a, (blue) for $l_h = 2000$ m (left) and $l_h = 63$ m (right). Simulated using ASPECH.

momentum as that of the maximum winds, and located at a radius $r|_{M_g}$, is then the gradient wind.

This method avoids accounting for the unbalanced wind contribution but requires assuming hydrostatic balance and moist slantwise neutrality above the boundary layer, which may impact the resulting V_g as well as SI_g. Indeed, moist slantwise neutrality is not respected as well at large values of l_h as it is at small values. More precisely, ds^*/dM decreases with height due to horizontal mixing (not shown), so that V_g is overestimated when l_h is large.

2.4.1 Simplifying approximations in PI_g and PI_a

The validity of the main physical assumptions of the gradient PI theory, namely thermal wind balance, moist slantwise neutrality and the boundary layer closure, has been evaluated in BR09a. In a replication of BR09's results, we verified that the moist slantwise neutrality and boundary layer closure are fairly well satisfied in the simulations presented here and as such will not discuss them further. However, the simplifying approximations for PI_g and PI_a, that allow one to go from Eq. 2.6 to Eq. 2.7 have not been evaluated for various intensities. The PI_g derivation approx-

imates $T_s \approx T_b$ for the purpose of computing thermodynamic efficiency, $V_{10} \approx V_{g,b}$ and $\bar{r} \approx r_b$ to relate momentum at the top and bottom of the boundary layer, and $|\mathbf{V_{10}}|^2 \approx V_{g,b}^2$ for the dissipative heating. These approximations are generally thought to be small and largely cancel out. To verify this, we compare the average value of the approximate PI_g to that of the unapproximated form of Eq. 2.6. The averaging is done over the most intense part of the simulations, from day 8 to 12, corresponding to the times at which we intend to evaluate superintensity. The contribution of each individual assumption to the final result is also evaluated.

Figure 2-4 shows the mean of the normalized difference between PI_g and unapproximated gradient PI as a function of the mixing length. All results represent the relative departure from the unapproximated form due to a given assumption. For example, the temperature assumption plot (green profile) is really just $(T_s - T_b)/T_b$. The assumptions are multiplicative so that the combined effect of all the approximations (black profile) is not equal to the sum of the individual approximations. Note that while the errors owing to the assumptions about velocities, radius, and dissipative heating can be as large as 20%, they end up cancelling for the most part, so that PI_g is within 10% of the unapproximated PI. This difference is even smaller (about 5%) at small mixing lengths, so that for the purpose of evaluating superintensity, we will use the approximate PI_g and PI_a forms. In this chapter, the approximations described above mostly serve to simplify the interpretation of the PI_g and PI_a forms. However, computing an a priori gradient wind PI from only environmental variables would require taking a similar set of approximations.

2.4.2 Surface PI

Next, we look at whether the surface PI (PI_s) is well respected in the ASPECH simulations. Contrarily to PI_g, which needs to be compared to gradient wind computed from the simulation data, PI_s is directly compared to output surface winds. As such,

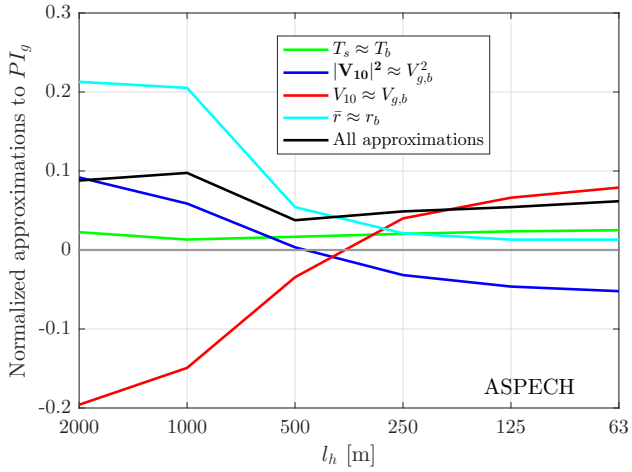

Figure 2-4: Contribution of simplifying assumptions to PI_g as a function of l_h, in ASPECH, for the SST approximation (green), the dissipative heating approximation (blue), the exchange coefficient approximation (red), the radius of M surfaces approximation (cyan), and the combined effect of all assumptions (black).

assumptions enter only in the derivation of the surface PI, not in the quantity it is compared to.

Figure 2-5 shows time series of the maximum surface winds and surface PI for all simulations. The time series of PI_s do not extend to the start of the simulation, because the outflow temperature is not initially well defined. The minimum values of PI_s during intensification are similar for all simulations, which is consistent with the identical environment in all simulations. Note again that PI_s depends on a differential Carnot cycle, and the fact that Hakim (2011) showed that simulated steady state hurricanes do not have a full Carnot thermodynamic cycle does not mean that there is any problem with the PI_s derivation, as it only requires the inner core portion of the Carnot cycle to be valid.

As $|\mathbf{V_{10}}|$ tends to PI_s, both time series covary surprisingly closely, with the increase in PI_s following closely the intensification of $|\mathbf{V_{10}}|$. Variations of $|\mathbf{V_{10}}|$ on time scales of less than a day are also captured by PI_s. This interesting result is an indication that the Carnot energetic constraint is consistent with the relation be-

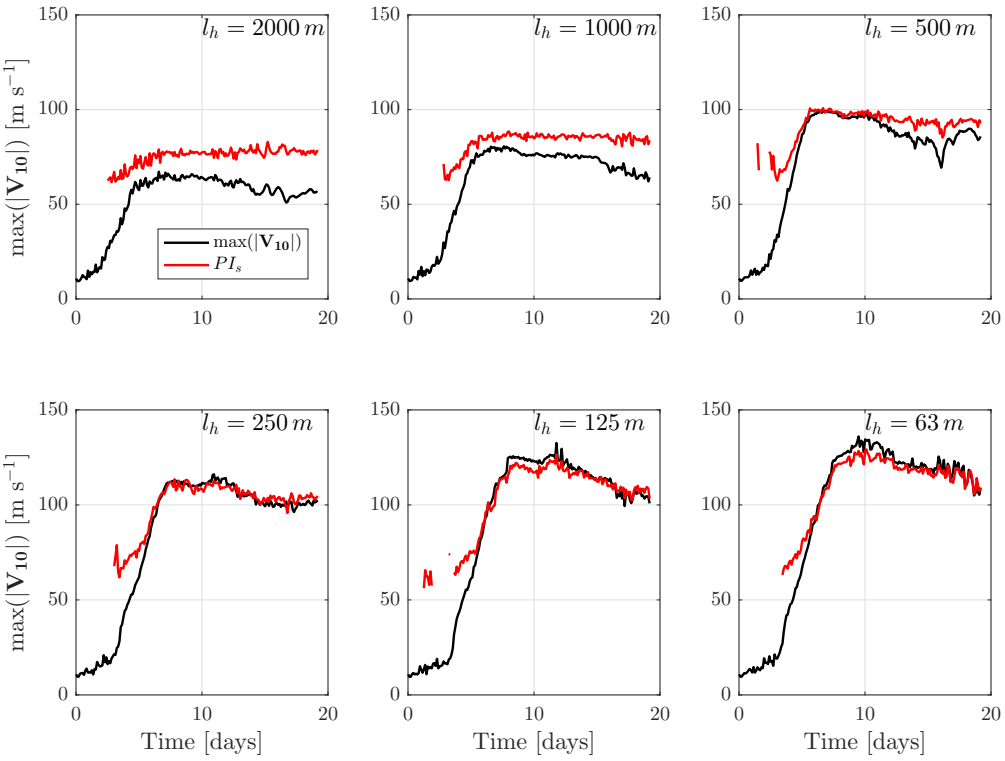

Figure 2-5: Time series of the maximum magnitude of surface winds in ASPECH, $|\mathbf{V_{10}}|$ (black), in m s^{-1}, and the surface potential intensity, PI_s, (red) for all simulations.

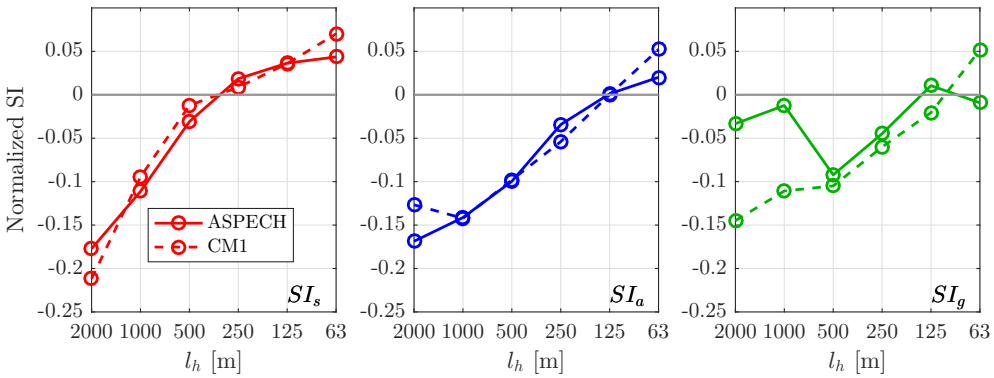

Figure 2-6: Averaged normalized SI as a function of l_h with respect to the surface PI, SI_s (left, red), the azimuthal PI, SI_a (center, blue) and the gradient PI, SI_g (right, green) for ASPECH (solid line) and CM1 (dashed line) .

tween the dynamics and the thermodynamics of the simulated TCs, even on short time scales. It is not entirely clear why PI_s covaries with $|\mathbf{V_{10}}|$ on short time scales rather than on average, over steady periods as per the assumptions of PI. CM1 yields similar results (not shown), but the surface winds exceed PI_s by up to 7% in the $l_h = 63$ m simulation.

2.5 Superintensity

First, we present the superintensities for each variable, normalized with respect to the corresponding PI bound and averaged from day 8 to day 12. For example, for the surface SI, $SI_s = (\max(|\mathbf{V_{10}}|) - PI_s)/PI_s$. The interpretation of SI is the following: $SI_s = -0.2$ for a given simulation means that the average magnitude of the surface winds, during the most intense period, is smaller than PI_s by 20%. Conversely $SI_s > 0$ means that PI_s is exceeded on average during the same period by the quantity it should bound. The same reasoning is applied in computing SI for the azimuthal wind (SI_a) and for the gradient wind (SI_g). Figure 2-6 shows the various SIs as a function of l_h and for both models.

For most computed superintensities, there is a clear positive tendency with decreasing l_h. In CM1, SI_s increases from about -0.21 to 0.07, SI_a from about -0.17 to

0.05, and SI_g from about -0.15 to 0.05. In ASPECH, SI_s increases from about -0.17 to 0.05, SI_a from about -0.13 to 0.02, and there is no clear trend for SI_g. In both models, SI_s seems to have smaller sensitivities at small mixing lengths. Analysing SI_g is a bit complicated since the discrepancy (SI_g) between V_g, diagnosed using BR09a's method and PI_g, does not capture the effect of the departure from moist slantwise neutrality and from hydrostatic balance. SI_g, in this case, is due only to the boundary layer assumptions and the simplifying approximations applied between Eq.2.6 and Eq.2.7 .

At this point, it is important to note that the actual intensities and potential intensities vary much more with l_h than does SI. For example, Fig. 2-3 shows that the peak intensities increase by more than 100% over the range of l_h, while SI_a varies by less than 20 % and is generally closer to 0 at small mixing lengths than at large mixing lengths. This tells us that each PI and its bounded quantity both increase and converge with decreasing l_h. This behavior is expected as PI theories are defined for inviscid flow above the boundary layer. Larger mixing lengths imply a decrease in the eyewall entropy gradient so that V_g and V do not reach PI_g and PI_a, respectively. Alternatively, it implies that the assumption of isentropic ascent is not quite satisfied so that $|\mathbf{V_{10}}|$ does not reach PI_s. As l_h decreases, the PI assumptions are better satisfied.

Both models produce similar SI for surface winds. The surface PI diagnostic, PI_s, relies purely on model thermodynamics, and hence both models simulate a similar relation among the thermodynamic disequilibrium, the thermodynamic efficiency and the near surface winds. The simulations only become superintense with respect to the surface PI at small l_h, with values of $SI_s < 0.05$ in ASPECH and $SI_s < 0.07$ in CM1. Hence, since SI_s remains small at low mixing lengths, we conclude that PI_s is a good bound for surface winds.

The azimuthal wind PI, PI_a, however, depends both on thermodynamic and dynamical diagnosed components. Thus, even if the profiles of SI_a are similar in both

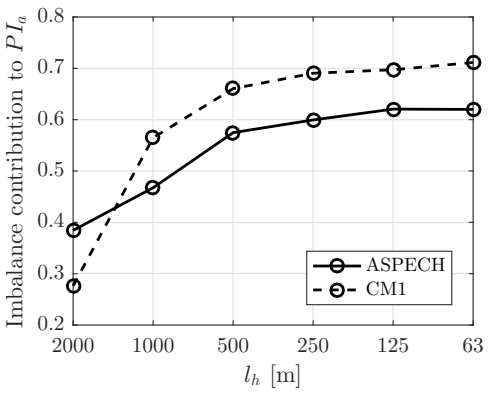

Figure 2-7: Averaged normalized contribution of the imbalance to PI_a as a function of l_h for ASPECH (solid line) and CM1 (dashed line).

models, the ratio of the dynamical and thermodynamic components may not be. Indeed, Fig. 2-7 shows that the increase in PI_a due to the imbalance (the last term of Eq.2.8, divided by PI_a), varies more and reaches larger values in CM1 than in ASPECH. In this study, the sensitivity of SI_a to l_h, which is clearly shown in Fig. 2-6, is larger than in BR09a, where $SI_a \approx 0$ for all simulations.

The above discrepancy between CM1 and ASPECH may be due to differences between the PBL schemes in both models and to an uncertainty in the computation of the unbalanced contribution. Indeed, here PI_a is computed by taking in situ values at a single point (point of maximum winds), as should be the case following BR09a. However, at high intensities, the high vorticity (η_b) and updraft (w_b) regions each collapse to one or two grid points that are not necessarily collocated so that diagnosing the contribution of the imbalance yields a somewhat variable effect. We do not, at this point, have an analysis explaining why this is the case but the inaccuracy of the imbalance term may be due to the very large intensities simulated and the relatively low horizontal resolution of the simulations (2000 m in contrast to 1000 m in BR09a). However, PI_a still bounds azimuthal winds within 5% at low mixing lengths.

The vertical mixing length is also known to be important in controlling the structure and intensity of TCs (e.g. Bryan, 2012; Rotunno and Bryan, 2012). Thus to

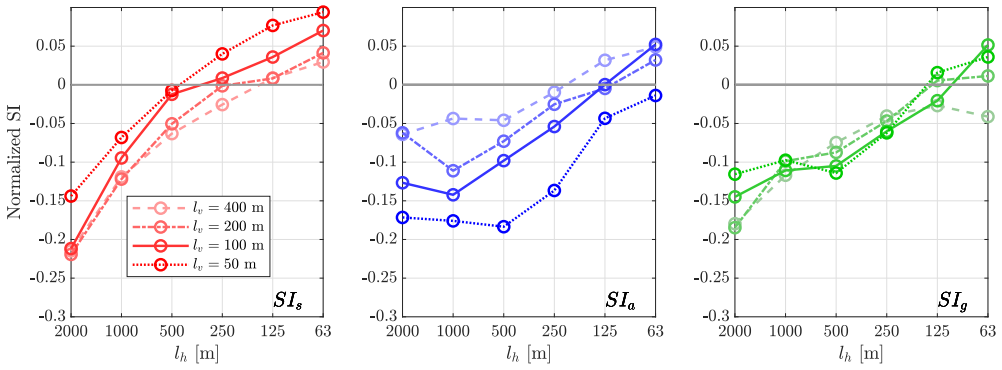

Figure 2-8: Averaged normalized SI in CM1 as a function of l_h with respect to the surface potential intensity, SI_s (left, red), the azimuthal potential intensity, SI_a (center, blue) and the gradient potential intensity, SI_g (right, green) for all values of l_v (brighter colors indicate lower values of l_v).

further evaluate the various PI bounds, we performed additional simulations using CM1 for the same values of l_h and for $l_v = 50$ m, 100 m (control), 200 m and 400 m. The results are shown in Fig. 2-8. SI_a profiles seem to flatten out and shift to higher values (closer to 0 on average) as vertical mixing increases. Interestingly, SI_s profiles seem to have an opposite trends, with the largest superintensities occurring at the smallest vertical mixing lengths. Since we do not yet have a physical understanding of these trends, Fig. 2-8 is mostly meant to show that the qualitative results of the chapter are not fundamentally altered by modifying other turbulence parameters.

2.6 Conclusion

This chapter introduced a new form of potential intensity bounding the maximum magnitude of the surface winds and based on the idea of a differential Carnot Cycle. This derivation has the advantage of only requiring the Carnot cycle's assumptions to be valid for the part of the secondary circulation located in the eyewall of the TCs, which is easier to satisfy.

Previous studies showed that supergradient flow is an important contributor to the azimuthal wind speed in superintense cyclones and that a gradient wind bound was not appropriate in that context. From there, we redefined SI as being the state where a quantity bounded by a given form of PI exceeds that bound. We evaluated three forms of PI (and the associated forms of SI): the newly introduced PI_s, and the existing PI_a and PI_g, bounding the magnitude of the surface wind, azimuthal wind and gradient wind respectively. The corresponding SI, (SI_g, SI_a and SI_s) were defined as normalized quantities, so that, for example: $SI_a = (V - PI_a)/PI_a$.

The derivation of PI_g requires making a series of approximations so that its computation only depends on thermodynamic variables. These approximations, namely $T_s \approx T_b$, $V_{10} \approx V_{g,b}$, $\bar{r} \approx r_b$, and $|\mathbf{V_{10}}|^2 \approx V_{g,b}^2$ were shown to cancel out to within 10% for l_h varying from 2000 m to 63 m.

SI_g and SI_a are always less than 5%, so that PI_g and PI_a seem to be good bounds on the maximum azimuthal winds, as was shown by BR09a. Finally, SI_s is generally less than 5%, suggesting that the Carnot-analog to the derivation from dynamical principles represents a good bound on the surface winds. Even if PI_g is a proper limit for gradient wind, it applies only to gradient wind, an ideal construct that is not necessarily realized. While PI_a applies to an actual wind speed and is very useful in assessing the contribution of supergradient flow to azimuthal winds, its computation relies on dynamical diagnostics. PI_s on the other hand, is a straightforward thermodynamic bound on surface winds, a quantity that is more relevant to hurricane risk assessment.

Future research directions may include investigating the sensitivity of superintensity to the numerical methods by modifying the scheme used in a given model. It would also be interesting to include a simple boundary layer model in a dynamical PI a priori method to estimate the unbalance in the boundary layer, and to estimate the maximum azimuthal wind for a given environment.

Chapter 3

A Thermodynamic Perspective on Steady-State Tropical Cyclones

Abstract

Theories for the maximum intensity of tropical cyclones (TCs) assume steady state. However, many TCs in simulations that run for tens of days tend to decay considerably from an early steady state in the core (CS), before stabilizing at a final equilibrium steady state (ES). This decay raises the question of whether CS or ES should be used as a comparison to the maximum intensity theories. To understand the differences between CS and ES, we investigate why TCs decay and attempt to simulate a TC with steady intensity over a 100-day period. Using the axisymmetric Cloud Model 1, we find that the CS TC decay is due to a large-scale drying of the subsidence region. Such a drying is very pronounced in axisymmetric models because shallow-to-mid level convection is not represented accurately enough to moisten air in the subsidence region. Simulations with an added moisture relaxation term in the subsidence region and dry cyclones without any moisture both remain in a steady state for over 100 days, without decaying appreciably after the spin-up period. These simulations indicate that the decay in TC simulations is due to the irreversible removal of precipitation combined with the lack of a moistening mechanism in the subsidence region. Once either of these conditions is removed, the decay disappears and the CS and ES intensities become essentially equivalent.

3.1 Introduction

Our understanding of complex atmospheric phenomena, like tropical cyclones (TCs), evolves as the result of a synergy between analytical theories, numerical modeling, and observations. Each branch of the research process informs the other two. Interestingly enough, simple analytical assumptions like that of an inviscid free troposphere, or of a system in steady state, can be challenging to understand when taken in the context of numerical modelling. For comparison with analytical theories derived using steady state assumptions, idealized numerical studies of TCs that focus, for example, on maximum winds or TC structure, conduct their analyses on a part of the simulation considered to be in steady state (e.g., Tang and Emanuel, 2012; Chavas and Emanuel, 2014; Persing and Montgomery, 2003). Theories of potential intensity (PI), a thermodynamic bound on maximum TC velocity that depends on properties of the environment, rely on such assumptions of steady state, and so do the numerical studies of PI (Rotunno and Emanuel, 1987; Bryan and Rotunno, 2009a; Hakim, 2011; Rousseau-Rizzi and Emanuel, 2019).

For all the instances where steady state is invoked in modelling studies, there does not seem to be a generally accepted rule for what constitutes a steady state in TCs, and as a result, different studies have quite different definitions. For example, Rotunno and Emanuel (1987) simulate the TCs' evolution for 6 days before they consider having reached a steady state, Bryan and Rotunno (2009a) runs simulations out to 12 days, and Hakim (2011) runs them for hundreds of days. Hakim (2011) performs axisymmetric numerical simulations of TCs using the model CM1 (Bryan and Fritsch, 2002; Bryan and Rotunno, 2009c) and notices that, after being quasi-steady for a few days, the intensity of the storm, defined here as the maximum wind speed, decays over a period of order ten days before becoming quasi-steady again at a much lower value. This newly achieved intensity then remains essentially constant for over a hundred days. Hakim (2011) argues that this latter intensity represents the physical steady state of TCs to which PI should be compared, and that the higher intensities reached

earlier on in the simulation are transient fluctuations due to either internal dynamics of the TC, or to unbalanced initial conditions. A similar behavior is noted by Chavas and Emanuel (2014). Smith et al. (2014) note that simulated TCs also decay in 3D model simulations. Their explanation is that angular momentum sinks far outweigh the sources and that the TC runs out of angular momentum. In this chapter, we wish to elucidate why decays such as those noted by Hakim (2011) and Smith et al. (2014) occur, and what differentiates various definitions of steady state. These questions are important because they inform both our general understanding of TC energetics, and the applicability of PI theories to real TCs, which are relatively short lived.

In general, the various definitions of steady-state intensity introduced in the literature can be grouped into two phenomenologically inspired categories, which we will label core-steady-state (CS), and equilibrium-steady-state (ES). As shown by the schematic of Fig. 3-1, CS is a definition that describes the state of the storm where the intensity varies slowly around peak intensity, which can occur after just a few days, depending on the numerical setup. ES describes the final state of a storm where the intensity becomes statistically steady for as long as anyone cares to run a simulation. It occurs later in time and is usually separated from CS by a decay period of a few tens of days. The steady state definitions of Hakim (2011) and Chavas and Emanuel (2014) fall in the ES category, while those of Rotunno and Emanuel (1987) or Bryan and Rotunno (2009a) belong to the CS category.

To understand the difference between the meaning of CS and that of ES, it is useful to understand the decay that separates them. To do so, we consider the evolution of conserved variables along the secondary circulation. The secondary circulation is the component of the TC circulation in radius-height ($r - z$) cylindrical coordinates. It captures most of the changes in the parcel properties that are relevant to TC energetics (Eliassen and Kleinschmidt, 1957). It is most easily understood in terms of the evolution of conserved or nearly conserved quantities that do not arise as the residual of large cancelling terms. Angular momentum (M) and pseudoadiabatic

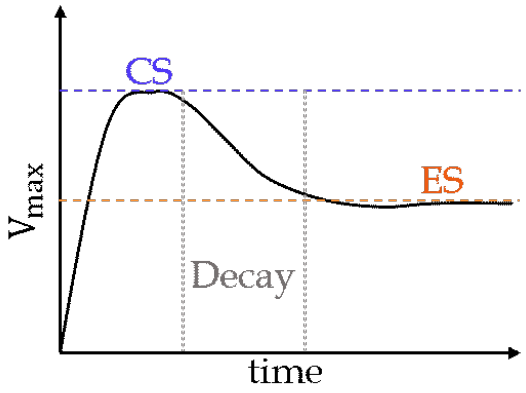

Figure 3-1: Conceptual schematic of maximum hurricane intensity over time in a typical long (>10 days) axisymmetric simulation. Core-steady state (CS) is identified by the dashed blue line and equilibrium-steady state (ES) is identified by the dashed orange line. The decay period is identified by dashed gray lines.

entropy (s) are such variables. For an air parcel, time tendencies of M can only arise due to turbulence, while time tendencies of s can only arise due to turbulence or departure from the pseudoadiabatic assumptions (e.g. Bryan, 2008). This makes it easier to identify the physical causes of changes in s and M along the secondary circulation.

3.1.1 Eliassen and Kleinschmidt Theory

We consider the early theory of TC energetics introduced by Eliassen and Kleinschmidt (1957), hereafter EK57. The theory of EK57 was the first one to our knowledge to represent the steady state TC as a closed thermodynamic cycle. This cycle is illustrated in Fig. 3-2, from EK57. In leg [1]-[2], air with environmental properties gains moist entropy in the form of a large moisture gain, and a small temperature increase, until the temperature is similar to the sea surface temperature (SST). Afterwards, the air ascends in the eyewall and into the outflow along leg [2]-[3], which is a moist adiabat, where by definition moist entropy is constant. Finally, the air cools radiatively, which causes it to subside along leg [3]-[1], back to its starting point. They suggest that an estimate of the storm velocity can be obtained by integrating the work done along that cycle. This is a method that has been used for some potential

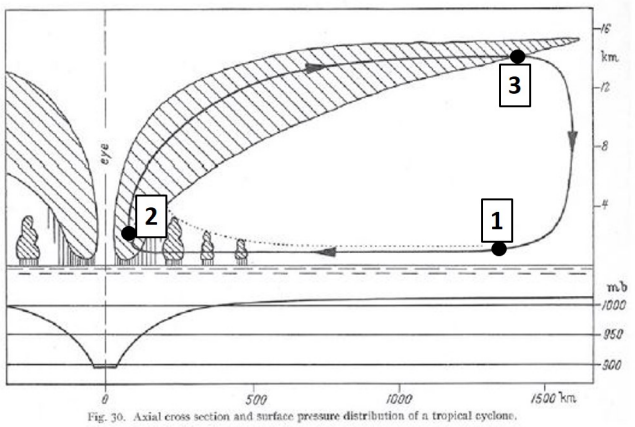

Fig. 30. Axial cross section and surface pressure distribution of a tropical cyclone.

Figure 3-2: Figure 30 from Eliassen and Kleinschmidt 1957, presenting a conceptual vertical cross section through a hurricane. The solid line with arrows denotes the shape and direction of the secondary circulation. Numbers indicate the transition between important segments, as discussed in the text

intensity (PI) theories (e.g., Emanuel, 1988).

One key fact is not made explicit in the model of EK57. The subsiding air will be much drier than the initial environmental air at the surface, unless the system obeys moist reversible thermodynamics (i.e., water condensed along leg 2-3 then evaporates along leg 3-1), or unless moisture is somehow regained through convective or environmental fluxes. Without regaining moisture, there would be a much lower moist entropy at the end of circuit [1]-[2]-[3]-[1] than at the beginning. So while the series of processes [1]-[2]-[3]-[1] is represented as a closed thermodynamic cycle, it must assume, perhaps implicitly in EK57, that the system is reversible or that entropy is regained by mixing at some point along the subsiding leg of the TC. The inflowing leg [1]-[2] and the ascent leg [2]-[3] each take $\sim$1 day to complete, while the radiatively driven subsidence leg takes tens of days to complete. Similar to the evolution of s, EK57 mention that M is lost to the sea surface in leg [1]-[2] and conserved in leg [2]-[3]. In order to have a closed cycle, M must be regained in leg [3]-[1].

3.1.2 Distinction between CS and ES

Given a conserved variable c, the conservation equation is written

$$\frac{dc}{dt} = \frac{\partial c}{\partial t} + \boldsymbol{u} \cdot \boldsymbol{\nabla} c = D_c, \tag{3.1}$$

where $\boldsymbol{u}$ is the velocity vector in the $r - z$ plane and D_c is the turbulent mixing tendency of c. More comprehensively, CS is defined such that in the inflow and ascent [1]-[2]-[3],

$$\left|\frac{\partial c}{\partial t}\right| << |\boldsymbol{u} \cdot \boldsymbol{\nabla} c|, \tag{3.2}$$

and the subsidence leg is assumed to evolve slowly from the initial value. That is, the local rate of change is small with respect to the balance between advection and turbulence, and the environment through which the air subsides is taken to be nearly fixed. ES, on the other hand, is defined as

$$\oint_{sc} \frac{1}{u_l} \frac{dc}{dt} dl \approx 0 \tag{3.3}$$

where sc denotes the fact that the integral is performed along the secondary circulation, l is position along sc, and u_l is the velocity along the secondary circulation, at position l . ES essentially requires the value of c of a parcel to be the same at the beginning and at the end of a loop along the secondary circulation. Hence, ES requires the integral of the local tendencies along sc, weighted by the inverse $r - z$ velocity, to vanish. This means that low-velocity regions, such as the subsidence region, must have correspondingly smaller time tendencies to satisfy ES. For now, we surmise that the difference (i.e., the decay) between CS and ES is due to a change in the environment of the storm. The conserved variables we chose to compare between the definitions of steady state are angular momentum M and pseudoadiabatic entropy s because their evolution and distribution capture, we believe, the most important dynamics (via M) and thermodynamics (via s).

3.1.3 Hypothesis

We further hypothesize that the decay noted by previous studies is due to a decrease of the subsidence region pseudoadiabatic entropy, on the subsidence timescale. Indeed, as we discussed, s of the air parcel after subsiding down to the surface will be much lower than the original environmental value, unless the parcel can somehow regain water vapor when subsiding. There are essentially only two ways in which this can happen. By vertical mixing, that is to say moistening by convection, or by horizontal mixing with environmental air. However, it happens that, in axisymmetric models like that of Hakim (2011), or in coarsely resolved subsidence regions like that of Smith et al. (2014), shallow-to-mid level convection is strongly suppressed. In addition, these models have closed boundary conditions so that no air “renews" the environment as would in effect happen with a real TC moving into a new environment. The implication of these model limitations is that moisture is unlikely to be regained along the subsidence leg.

3.1.4 Goal

The aim of this chapter is twofold: 1) to compare the two different definitions of TC intensity steady state defined above and 2) to quantify the physical processes required to obtain a closed EK57 type thermodynamic cycle. First, section 3.2 presents the model, simulation setup and methods to investigate the difference between CS and ES and the closure of the thermodynamic cycle. Then, section 3.3 shows the results of these computations and section 3.4 discusses the implications of the results and evaluates an alternative interpretation based on angular momentum. Finally, section 3.5 sums up the chapter and concludes.

3.2 Methodology

In this chapter, we are using Cloud Model 1 (CM1), a compressible atmospheric model in axisymmetric configuration (Bryan and Fritsch, 2002; Bryan and Rotunno,

2009c). The model's equation sets conserve mass and internal energy in saturated air and includes dissipative heating. The domain outer radius is 1500 km and the height is 25 km. The grid is radially uniform with a 2 km grid spacing in the inner 64 km and then stretches to 4 km at the outer edge of the domain. The grid spacing is 100 m in the vertical in the lower 500 m of the domain, stretching to 500 m grid spacing at the height of 6000 m. The vertical grid spacing is uniform above 6000 m.

The conversion of water vapor to hydrometeors is represented by the simple liquid water scheme of Rotunno and Emanuel (1987). The terminal velocity of liquid water is 7 m s^{-1}, which was shown by Bryan and Rotunno (2009c) to yield intensities close to the pseudoadiabatic limit. The advection scheme for both scalars and momenta is a 5th order WENO scheme. The turbulence parameterization is similar to that of Rotunno and Emanuel (1987) and is based on Smagorinsky (1963). The horizontal mixing length is fixed at a value of $l_h = 1000$ m and the asymptotic vertical mixing length is $l_v = 100$ m. Both of these are typical values in simulated axisymmetric TCs. The simulations use a surface exchange coefficients parameterization based on Fairall et al. (2003), Donelan et al. (2004) and Drennan et al. (2007). The simulations use a constant Coriolis parameter $f = 5 \times 10^{-5}$ s^{-1}. Radiation is parameterized by a Newtonian relaxation of potential temperature to the initial environmental state. The setup comprises two Rayleigh damping layers, within 5 km of the top boundary and within 100 km of the outer boundary. The top damping layer acts on all three components of velocity and on potential temperature, while the lateral damping layer only acts on vertical velocity. The outer boundary is closed.

The initial vortex, in all simulations, is defined to have a maximum wind speed of 15 m s^{-1} at the surface and at a radius of 100 km. The vertical extent of the vortex is 15 km, and the radius where the winds go to zero is 500 km. The initial thermodynamic profile in all simulations is exactly moist neutral to vertical displacement, using the model's equations, and is nearly saturated throughout the troposphere (Fig 1 of Bryan and Rotunno (2009a)). It is useful for the purpose of this chapter to have

a model sounding that is initially neutral to the model equations, as initial CAPE adds to the unsteadiness of the solution (not shown). The sea surface temperature is constant at 301 K, with an air-sea temperature difference of 3 K.

3.2.1 Simulations

In order to test our hypothesis that drying in the subsidence region is responsible for the decaying intensity of simulated TCs, we run three main simulations. The first one is a control case (CTRL), which uses the settings described above. The second one is almost identical, except that moisture in the subsidence region is relaxed to the initial value (RELAX) with a timescale of 2 days, as described below. The third one is a dry simulation (DRY) which has three differences with the CTRL: 1) a dry adiabatic troposphere in the environment, with a potential temperature lapse rate of 10K per kilometer in the stratosphere, 2) no moisture included in the simulation and 3), a large air-sea temperature difference (12 K). Everything else is kept identical to the CTRL. Then, in order to further test the sensitivity of the intensity to the drying, we also run two additional simulation named REL1 and REL4 that are similar to RELAX but use relaxation timescales of 1 day and 4 days respectively.

3.2.2 Role of the moistening

In RELAX, REL1 and REL4, water vapor mixing ratio is relaxed to the initial environmental state q_{v0} using

$$\frac{\partial q_v}{\partial t} = [...] + \mu\Big(\frac{q_{v0} - q_v}{\tau}\Big), \tag{3.4}$$

where the constant τ is 2 days in RELAX, 1 day in REL1 and 4 days in REL4. $\mu = \mu(r, z)$ is a mask that determines the region over which this relaxation term is applied. The mask excludes the core of the storm, the boundary layer and the upper-tropopheric outflow of the storm. It is applied only to the midlevels in the subsidence region. We note that this relaxation of water vapor is analogous to the Newtonian relaxation parameterization for radiation introduced in Rotunno and Emanuel

(1987) and used in our study. Rotunno and Emanuel (1987) introduced the radiation parameterization to balance the impact that a simulated TC would have on the environmental stratification inside a closed domain. The q_v relaxation term introduced here serves to balance excessive drying in the subsidence region. A similar moisture relaxation term (albeit applied to the entire domain) was used by Frisius (2015) who tested the sensitivity of TC size to varying simultaneously the timescale of both the Newtonian relaxation of temperature and that of moisture. The intensity in the simulations of Frisius (2015) decayed by about 10 to 20 m s^{-1} from day 10 to 50 but remained remarkably steady afterwards.

3.2.3 Trajectory integral

In order to understand the evolution of the entropy of a parcel along the secondary circulation, we define a method to integrate budget equations for pseudoadiabatic entropy s along the parcel trajectory. First, following Bryan (2008), we define the differential form of the pseudoatiabatic entropy equation

$$Tds = c_p dT + L_0 dq_v - \frac{1}{\rho_d} dp, \tag{3.5}$$

and the integrated form

$$s = c_p \ln(T) - R_d \ln(p_d) + \frac{L_0 q_v}{T} - R_v q_v \ln \mathcal{H}. \tag{3.6}$$

where c_p is the heat capacity of dry air at constant pressure, T is the temperature, R_d is the dry air gas constant, p is the pressure, p_d is the dry air pressure, ρ_d is the dry air density, L_0 is a constant latent heat of vaporization, q_v is the water vapor mixing ratio, R_v is the gas constant of water vapor and $\mathcal{H}$ is the relative humidity. Then, since CM1 outputs accurate budgets of potential temperature (θ) and q_v, we write the budget equation for entropy in terms of θ and q_v. Following a trajectory, we have

$$\frac{ds}{dt} = \frac{c_p}{\theta} \frac{d\theta}{dt} + \frac{L_0}{T} \frac{dq_v}{dt}, \tag{3.7}$$

which we can break down into budget terms

$$\frac{ds}{dt} = \frac{c_p}{\theta}(D_\theta + N_\theta + R_\theta + \epsilon_\theta) + \frac{L_0}{T}(D_{q_v} + N_{q_v} + M_{q_v}), \tag{3.8}$$

or equivalently

$$\frac{ds}{dt} = D_s + N_s + R_s + \epsilon_s + M_s, \tag{3.9}$$

where D is parameterized turbulence, N is implicit diffusion, R is radiation or θ relaxation, M is moisture relaxation and ϵ is dissipative heating. The subscripts indicate the variable to which the tendency term applies. By implicit diffusion N, we mean an estimate of the diffusive component in the advection scheme, computed using higher order expansion of the advection scheme, similar to the method of Wicker and Skamarock (2002). This N needs to be taken into account in the budget because along-trajectory budgets require an accurate computation of the Lagrangian derivative, which by definition does not include source terms or diffusive effects, either parameterized or implicit. The next step is to average the equation in time to filter out high frequency variability like gravity waves. The Lagrangian derivative of time-averaged entropy $\bar{s}$ in a time averaged flow $\bar{\mathbf{u}}$ is

$$\frac{d\bar{s}}{dt} = \frac{\partial \bar{s}}{\partial t} + \bar{\mathbf{u}} \cdot \boldsymbol{\nabla} \bar{s}. \tag{3.10}$$

We note that the time mean of the advection is not the same as the advection by the time mean flow. As we take the time average of the advection budget term, we need to account for the eddy mixing term,

$$\overline{\mathbf{u} \cdot \boldsymbol{\nabla} s} = \bar{\mathbf{u}} \cdot \boldsymbol{\nabla} \bar{s} + \overline{\mathbf{u}' \cdot \boldsymbol{\nabla} s'}, \tag{3.11}$$

where the overbar denotes a time average, and the prime a perturbation with respect to that average. For example, $s(r, z, t) = \bar{s}(r, z) + s'(r, z, t)$. On average, we are therefore left with an additional eddy term which needs to be treated like a source term,

$$\frac{d\overline{s}}{dt} = \overline{D_s} + \overline{N_s} + \overline{R_s} + \overline{\epsilon_s} + \overline{M_s} + \overline{E_s} \tag{3.12}$$

where $\overline{E_s} = -\overline{\mathbf{u}' \cdot \boldsymbol{\nabla} s'}$. The eddy term needs to be computed with the model's advection scheme (because of the large higher order spatial derivatives near the eyewall of the hurricane, a lower order advection scheme yields large errors). Since this budget is applied to time-averaged flow, hereafter, "trajectories" will refer to nominal trajectories in $r - z$ space that are computed from the mean flow by integrating

$$\frac{d\overline{r}}{dt} = \overline{u}, \qquad \frac{d\overline{z}}{dt} = \overline{w}. \tag{3.13}$$

The different terms contributing to the budgets of θ and q_v are interpolated onto the trajectory and used to compute the entropy budget.

3.3 Results

Since we are concerned with the evolution of intensity and its steady state, in Fig. 3-3, we compare timeseries of the maximum instantaneous tangential velocity for 1) the CTRL case (gray), 2) the RELAX case (blue) and 3) the DRY TC simulation (yellow). The CTRL case reaches its peak intensity around day 9, remains quasi-steady at about 73 m s^{-1} for 3 to 4 days and then decays to 37 m s^{-1} over the course of about 50 days. The CTRL TC eventually dies out completely without reaching ES, like a similar simulation in Hakim (2011). In the RELAX case, the simulation reaches peak intensity around day 15, remains quasi-steady at about 85 m s^{-1} for a few days, and then decays slowly by about 10 m s^{-1} before reaching ES around day 80, which holds for as far as we have run that simulation (200 days). Finally, the DRY case reaches a maximum around 20 days and then remains statistically steady for the rest of the simulation.

Figure 3-3 provides evidence that either relaxing moisture in the subsidence region or removing moisture altogether removes most of the decaying behavior of the TC and essentially makes ES equivalent to CS. The tentative conclusion from that

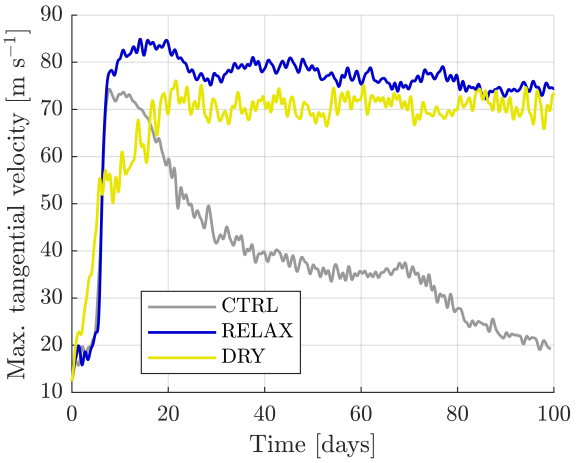

Figure 3-3: Time series of the maximum instantaneous azimuthal velocity for CTRL (gray), RELAX (blue) and DRY (yellow). The time series are filtered with a Lanczos filter and a cutoff frequency of 1 day.

result, combined with the discussion in the Introduction, is that moisture changes in the environment cause CS to depart from ES. In order to further test that hypothesis, an additional simulation was run with reversible thermodynamics (no fallout of precipitation), which also removes the decay (not shown).

Figure 3-4 compares three Hovmöller (radius-time) diagrams of the evolution of the entropy perturbation near the sea surface. The plots extend from a radius of 0 to 900 km, to encompass all of the inflow branch of the secondary circulation, and from a time of 0 to 40 days, to encompass both intensification and decay in the CTRL case. Extending the plots further in radius or time does not change the conclusions. The colormaps extend from -50 to 50 [J kg^{-1} K^{-1}]. For reference, 50 [J kg^{-1} K^{-1}] is roughly the difference of entropy between the near surface layer at the initial time and the outflow layer of CTRL at maximum intensity. A negative value means that the entropy has decreased with respect to the initial value. In the CTRL simulation, the moist entropy increases for about the first 10 days, with the largest increase occurring in the eyewall region. Then, s decreases substantially under the subsidence region, to values well below the initial conditions. The radial wind-induced increase in s as the air spirals inwards from a radius of 400 km is not sufficient to counteract that massive local decrease. This decrease in s is due to

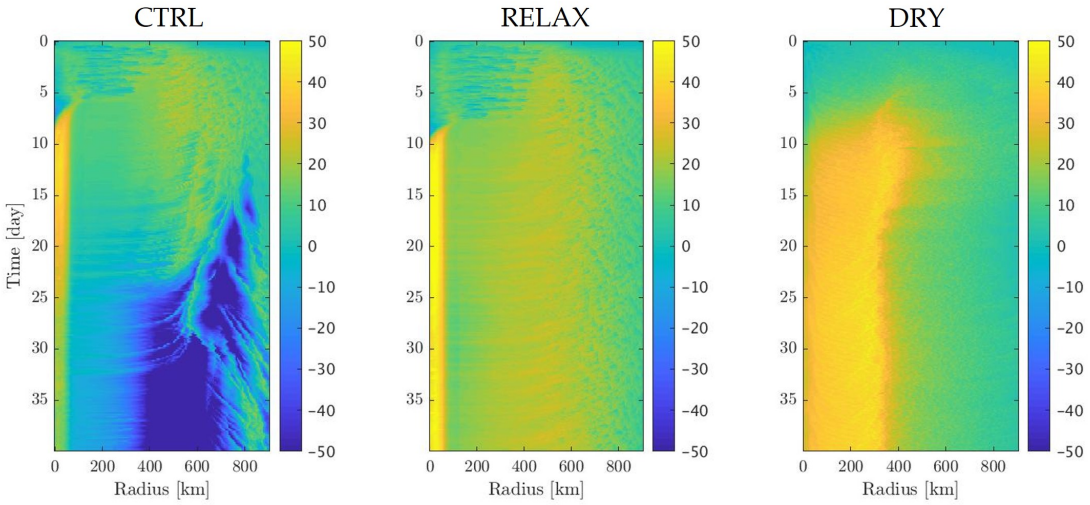

Figure 3-4: Day 0 to 40 Hovmöller diagrams of the near surface (z = 100 m) pseudoadiabatic entropy perturbation [J kg^{-1} K^{-1}] for CTRL (left), RELAX (center) and DRY (right).

moisture decreases, as temperature and pressure cannot depart much from the initial values. Surface and low-to-mid tropospheric mixing ratio exhibit similar signals (not shown). In the RELAX simulation, the entropy increases everywhere near the surface, as the storm intensifies, and remains higher than in the initial conditions. The DRY case is similar to the RELAX case in the sense that the near surface entropy remains everywhere higher than in the initial conditions, after intensification. Consistent with the time series, the DRY case takes longer (≈20 days) to become steady on average than the RELAX case (≈10 days), and has higher variability afterwards. Figure 3-4 along with Fig. 3-3 makes a strong case that the drying of the subsidence region is responsible for the TC decay in the CTRL case.

3.3.1 Trajectory integral results

Using the trajectory integral method introduced earlier, we now look at the time it takes an air parcel to travel along the different sections of the secondary circulation. In Table 3.1 we see that for both the CTRL and RELAX cases, the parcel takes about 10 times longer to subside as it takes to travel from the inflow to the outflow of the storm. In CTRL, the subsidence timescale of 39 days is essentially the time it takes

Simulation	Inflow time	Outflow time	Subsidence time
CTRL	1.5	1.5	39
RELAX	2	2	37
DRY	2	0.8	1.7

Table 3.1: Summary of the time [days] it takes a parcel to travel along different segments of the secondary circulation. The total time is the sum of the inflow time, the outflow time and the subsidence time.

for all moisture to be removed from the subsidence region in the absence of some process to replenish it. The drying starts as soon as air begins to subside, and the environment becomes completely dry ($RH \approx 0$) around 39 days later. In addition, the profile of moisture is exponential in temperature, which means that, for fixed subsidence, the relative humidity at a given point in the subsidence region decreases faster earlier in the simulation than later, shifting the impacts of the drying earlier in the simulation. This is likely responsible for the maximum surface entropy (and intensity) peaking earlier and at a lower value in CTRL than in RELAX (Figs. 3-3 and 3-4). In DRY, it takes about the same time to subside as it takes to ascend. These results indicate that the assumption in the CS definition, that the subsidence region varies slowly with respect to the core, is appropriate for CTRL and RELAX. In DRY however, the subsidence region does not vary slowly with respect to the core. Hence, the slowly varying inflow and outflow conditions required by CS only arise when equilibrium is reached, and ES and CS must become equivalent in this case.

Next, we look at the integrals of s along the cycle to better understand the definition of ES.

To gain insight into the decay of the control case, Fig. 3-5 shows plots of the $T - s$ cycles of the three main simulations, along the trajectory that passes through the position of maximum winds. The black lines illustrate conditions along the parcel trajectories that cross the position of maximum winds in each simulation, in $T - s$ space. The colored (gray, blue and yellow) lines are the values of the integrals in time of the Lagrangian entropy budget, from the position of maximum winds onwards. That is

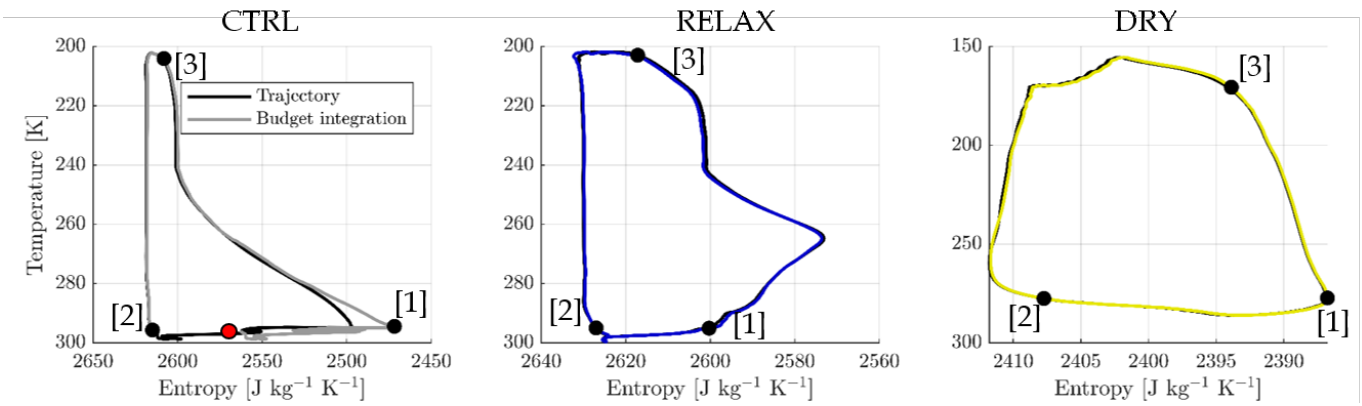

Figure 3-5: Illustration of thermodynamic conditions along the secondary circulation in $T-s$ space using two approaches: using actual entropy along a trajectory (black); and using the integral of the entropy budget along the same trajectory (colors). The trajectory begins and ends at point [2] (the radius of maximum winds). The red dot indicates the final point of the integrated budget in CTRL, since it differs from the initial point; gray (left) is CTRL, blue (center) is RELAX, and yellow (right) is DRY. Temperature decreases upwards and entropy decreases to the right so that the $T-s$ space is oriented in the same way as $r-z$ space.

$$\oint_{sc} \frac{1}{u_l}(\overline{D_s} + \overline{N_s} + \overline{R_s} + \overline{\epsilon_s} + \overline{M_s} + \overline{E_s})dl. \tag{3.14}$$

The averages here are performed from day 20 to 100 for both the DRY and the RELAX case, which are quite steady, and performed from day 15 to 25 for the CTRL simulation, which is decaying. In both RELAX and DRY, the s integral computation over the whole cycle matches the model simulated values of s very well, indicating that both RELAX and DRY are essentially in ES over the averaging period. In addition, this indicates that the budget is accurate and quantitatively captures the contribution of various source terms to the entropy variation along the trajectory. In CTRL, one can observe two main differences with respect to the steady cases. First, the budget does not close, which is unsurprising given that the simulation is obviously decaying and not in an equilibrium steady state. If the tendency terms, averaged over day 15-25 are integrated over the full trajectory, the result is a much lower entropy than the starting value. Second, there is a massive decrease in entropy along the trajectory as the temperature of subsiding air increases. The entropy of the subsiding

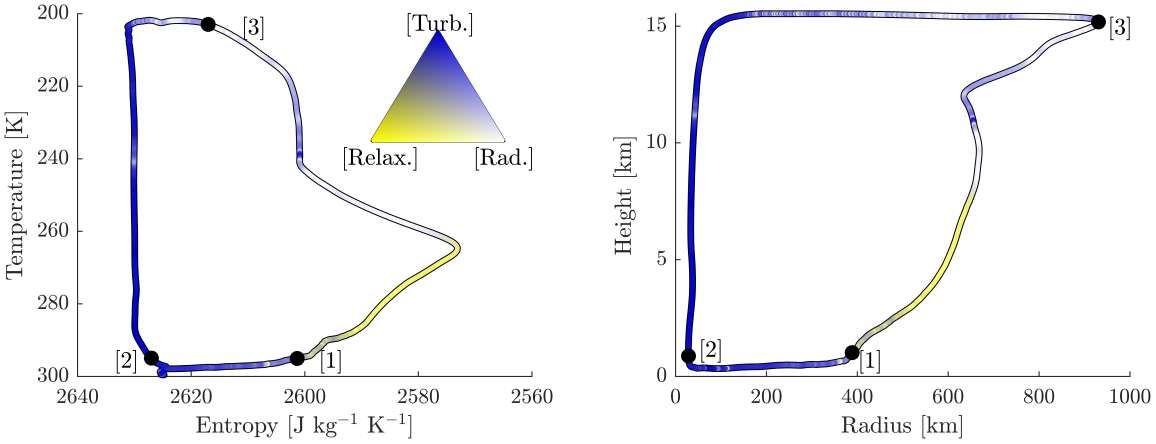

Figure 3-6: RELAX case parcel trajectory along the secondary circulation in $T - s$ (left) and physical (right) space. The trajectory is color-coded to outline the most important contributors to the entropy budget. Blue represent turbulence terms, white represent radiation and microphysics, and yellow represents parameterized moisture relaxation.

air decreases to much lower values than the initial values of entropy near sea surface, which once again, points to the lack of a mechanism to regain entropy while the air subsides.

To gain additional insight into the processes involved in reaching ES, we break down the entropy budget into its main components. Figure 3-6 shows again an integrated $T - s$ cycle for the RELAX simulation, along with the trajectory of the parcel in physical space. The plot is colored as a function of the three-way relative magnitude of terms in the entropy budget. Blue for turbulence terms, white for radiation/relaxation and hydrometeor fallout (which is small), and yellow for parameterized moisture relaxation. The interpolation of these terms is presented in the triangular colormap. This shows that segment [1]-[2] is dominated by turbulence, driven by air-sea interaction. Next, segment [2]-[3] is dominated initially by turbulence and then by radiation. Even though turbulence is the dominant term in the vertical portion of [2]-[3], it has a small absolute magnitude there. Finally, segment [3]-[1] is dominated initially by radiation, and then by q_v relaxation, with a large counteracting effect from radiation. This quantification of the mechanisms entering in a hurricane thermodynamic cycle over the timescales of the secondary

circulation verifies the requirements for a EK57-type TC. The CTRL case, without q_v relaxation, shows a cycle that does not close because the radiation keeps driving the entropy to lower values without counteracting effects (not shown). We note that the secondary circulation in RELAX does not extend far radially compared to other studies performing long term integrations (e.g., Chavas and Emanuel, 2014; Persing et al., 2019). One possible explanation is the choice of Newtonian relaxation to a background sounding rather than more realistic parameterized radiation such as the Rapid Radiative Transfer Model. Newtonian relaxation does not account for cloud radiative feedbacks (CRFs), and as was shown by Bu et al. (2014), CRFs act to greatly enhance the radial extent of tropical cyclones. The lack of CRFs in our study, as opposed to the relatively small domain (compared to these previous studies), might result in this compact storm. Indeed, there is no evidence that the secondary circulation reaches the outer wall in CTRL and RELAX. We further confirmed that the domain size does not constrain the radial extend of the CTRL and RELAX storms by rerunning those simulations for 80 days in 6000 km domains. We could not find any appreciable difference in the structure and evolution of the CTRL and RELAX storms in the two different domain sizes (not shown). In addition, other studies using Newtonian relaxation also obtained similarly compact storms (e.g., Emanuel and Rotunno, 2011; Frisius, 2015) for which the secondary circulation does not impinge on the outer boundary. We acknowledge that the mid-tropospheric drying reported in this chapter is likely to be sensitive to radiative and microphysical parameterizations via their influence on the secondary circulation.

3.3.2 Moisture relaxation timescale sensitivity

CTRL does not have a clear ES, and while RELAX does, it is not very different from its CS. In order to better understand the difference between CS and ES, and the evolution from CS to ES, we now turn our attention towards REL1 and REL4, which have different moisture relaxation timescales than RELAX, and should lead to different ES. Figure 3-7 shows timeseries of the maximum velocity for REL1, RELAX and REL4. From CS onwards, the smaller the τ, the closer EC becomes to CS. During CS,

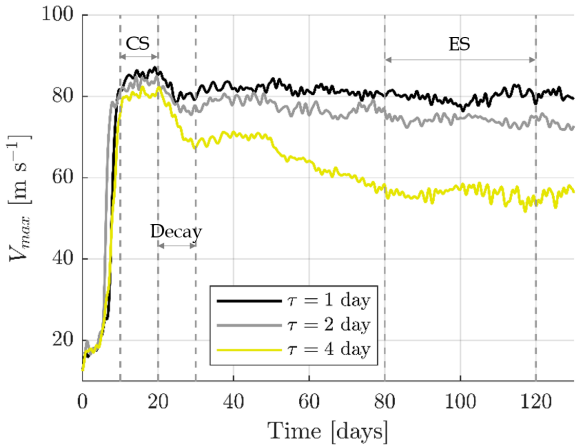

Figure 3-7: Time series of the maximum instantaneous azimuthal velocity for REL1 (black, $\tau = 1$ day), RELAX (gray, $\tau = 2$ days) and REL4 (yellow, $\tau = 4$ days). The time series are filtered with a Lanczos filter and a cutoff frequency of 1 day. CS, Decay and ES time intervals are identified for the purpose of comparing thermodynamic cycles in Fig.3-8.

REL1 is 3 m s^{-1} more intense than RELAX, and 6 m s^{-1} more intense than REL4. The decay is more rapid and lasts longer at large τ so that the intensity differences grow until a clear ES is reached for all three simulations. During ES, REL1 is 6 m s^{-1} more intense than RELAX, and 25 m s^{-1} more intense than REL4.

Next, Fig.3-8 shows the thermodynamic cycles of REL1, RELAX and REL4 over the CS, Decay and ES periods identified in Fig.3-7. Figure 3-8 also shows the thermodynamic cycles of CTRL over comparable CS (day 8 to 12) and decay (day 15 to 25) periods, and right before the storm simulation ends (day 70 to 90). Note that the abscissa in CTRL has the same maximum value as those in the other plots, but extends to much smaller values. The most obvious difference between the plots is that, for a given period (CS, Decay or ES), the entropy in the core of the storm is lower when τ is larger, and that difference grows as time goes on, until it stabilizes at ES. The second thing to notice is that the area encompassed by the thermodynamic diagram itself changes much less for smaller τ. This shows that CS and ES are not only very similar in intensity at small τ, they are also similar in the area within the $T - s$ diagram. At larger τ, or in the CTRL case, the entropy in the core decreases as

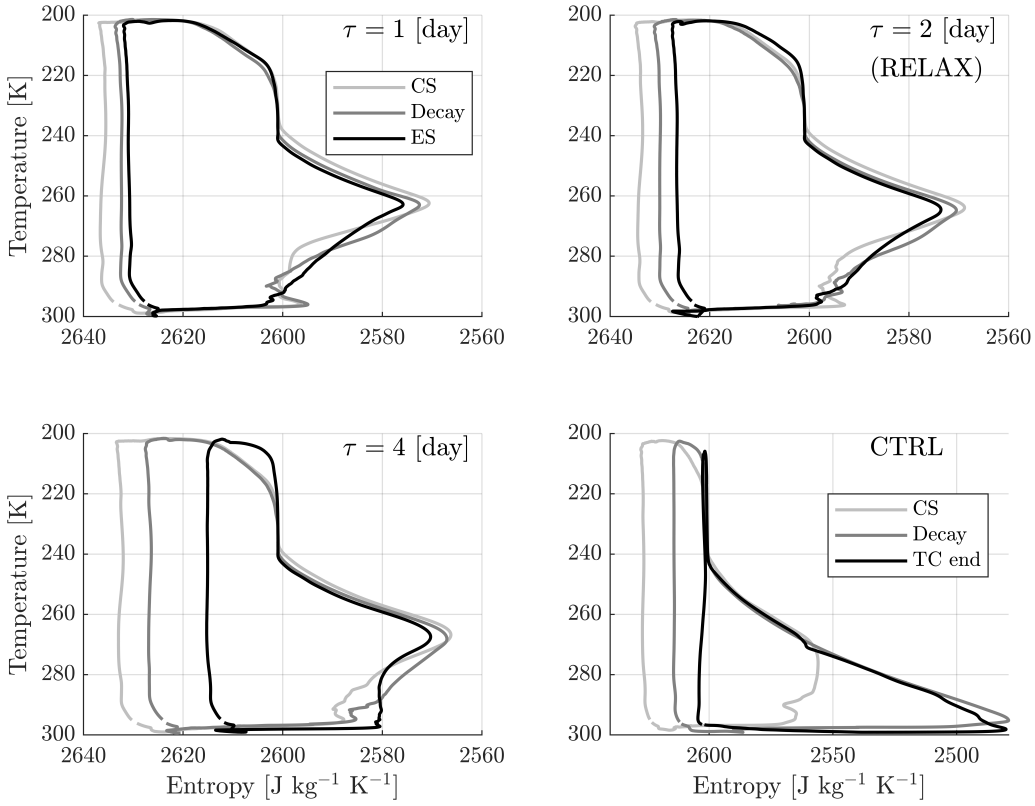

Figure 3-8: $T - s$ cycles for CS (pale gray), Decay (gray) and ES (black) for REL1 (top left), RELAX (top right), REL4 (bottom left) and CTRL (bottom right). There is no ES in CTRL, so a $T - s$ cycle taken right as the TC simulation ends (days 70 to 90) is plotted instead.

the near surface entropy at large radius decreases. REL4 confirms that quasi-steady intensity can exist both when the thermodynamic cycle is still far from equilibrium (CS) and once it has reached equilibrium (ES). Examination of the thermodynamic cycles of CTRL shows why the storm ultimately dies out. As too little entropy is regained along the inflow to compensate that lost in the subsidence, s decreases in the core until it drops below the value in the upper troposphere subsidence region. While the TC streamlines in physical space do not change much in REL1 and RELAX between CS and ES, they do in REL4 and CTRL, where, over the decay period, the outflow leg contracts radially from an extent of about 950 km in both cases to about 650 km in REL4 and 400km in CTRL (not shown).

3.4 Discussion

3.4.1 CS vs ES

These results indicate that the decay in CTRL is due to the combination of the irreversible precipitation removal in the ascent leg, and the lack of a moistening mechanism in the subsidence leg. If we either add a rapid moistening mechanism in the subsidence region (as in RELAX or REL1), remove moisture altogether from the model (as in the DRY simulation) or prevent precipitation removal (not shown), the decay mostly disappears. This is further confirmed by the sensitivity of ES to τ, which we would expect from the argument that drying is driving the decay and explains the difference between CS and ES. Interestingly, CS is also sensitive to τ, albeit not as much. For example, the RELAX peak (CS) intensity is higher than that of CTRL by 10 m s^{-1} while lower than that of REL1 by 3 m s^{-1}. This indicates that the CS assumption, that the environment does not have time to change before peak intensity, is not very robust. In CTRL, subsidence drying results in a peak intensity that is lower, even just 10 days after the beginning of the simulation. There remains a small decay in RELAX after CS, which can be due to the moisture and temperature fields slowly reaching equilibrium or to the evolution of the M field (discussed below). In any case, the dominant effect on the decay in CTRL is the drying. The DRY case is also interesting in that its inflow-ascent-outflow timescale is so similar to its subsidence timescale that the theoretical difference between CS and ES disappears. And indeed, DRY does not show any sign of decay after reaching peak intensity.

From our results it seems that the definition of ES would be quite difficult to generalize or to compare with environmental PI theories, that is, PI for a specified and possibly arbitrary environmental profile. Indeed, while CS is very sensitive to a host of model parameters like resolution (Hausman, 2001), terminal velocity (Bryan and Rotunno, 2009c) or mixing length (Rotunno and Bryan, 2012), ES will additionally be sensitive to any parameter that influences the equilibrium state of the model, like τ, or any parameterization for the radiation, surface fluxes, turbulence, or convec-

tion. The foregoing sensitivities would defeat the purpose of using PI to predict the intensity of a TC based on environmental parameters, and it seems that PI should be compared to CS. In addition, the intensity is closer to reaching PI (computed following Bryan and Rotunno, 2009a) during CS than during ES, because PI doesn't decrease as much as intensity during the decay (not shown). A possible explanation for the fact that our CTRL simulation decays until it ends while other simulations without moisture relaxation do not (e.g., Hakim, 2011; Chavas and Emanuel, 2014) is the fact that these simulations used radiation parameterizations representing CRFs, which enhance the radial extent of the cyclone, and entails more time for the air spiraling inwards to regain entropy. As was shown by the τ sensitivity experiment, if the entropy in the core does not decrease as much, a smaller decay should occur.

3.4.2 Angular momentum

Thus far, we have been silent about the evolution of other conserved variables, and more specifically dynamical variables like M. The goal was to demonstrate the role of moisture before discussing additional possibilities. Previous literature (e.g., Smith et al., 2014) has argued that the decay of simulated storms is primarily due to the loss of angular momentum to the sea surface, which causes the angular momentum, and thus the intensity to decrease at the radius of maximum winds. From the results obtained in this chapter, it appears that the decrease in angular momentum at the radius of maximum winds in CTRL, concurrent with the decay, is simply a consequence of the TC failing to produce enough work to draw high angular momentum air inwards at small radii.

As proposed by Smith et al. (2014), the mass-integrated angular momentum in the domain initially decreases as a result of the stresses applied by the TC winds on the lower boundary. However that decrease is small with respect to the domain-integrated M. Figure 3-9 shows the domain-integrated M as a function of time (full line), and the initial value of the domain-integrated M plus the time-integrated surface sink of M along the inflow (dashed line). The two would be equivalent if the only sink or

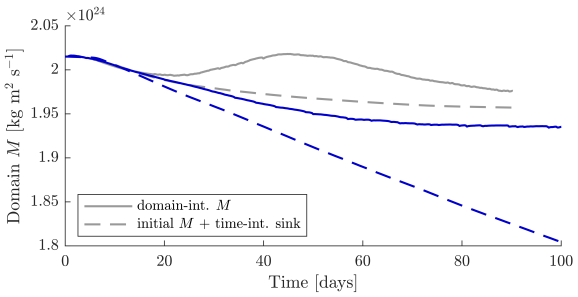

Figure 3-9: Domain-integrated M as a function of time (solid line) and domain-integrated M at $t = 0$ plus the time-integrated surface momentum sink (dashed line) for CTRL (gray) and RELAX (blue). The momentum sink is integrated in time and space in the inner 500 km from the start of the simulation.

source of momentum was along the surface inflow.

Eventually the domain-integrated M stops decreasing after about 80 days in the RELAX case, even as the slope of the momentum sink time-integral remains negative and linear (implying that the surface sink of M remains constant). This leveling-off of domain-integrated M is due to the fact that the anticyclone deepens until it starts impinging on the stratospheric damping layer, at which point the imposed damping starts to restore domain-integrated angular momentum by weakening the anticyclone. In the secondary circulation (which is well below the damping layer), examination of budget terms for M shows that M is regained by parameterized mixing with the environment while air subsides at the largest radius in the storm outflow. There, while velocities are quite small, the radial derivative of angular velocity is large, which causes turbulent mixing. This mixing, which occurs mostly over a thin 1 km layer, around an altitude of 15 km, restores to the secondary circulation essentially all the angular momentum lost to the sea surface by the circulating air, while slightly decreasing angular momentum in the environment.

Figure 3-9 shows that while the variables relevant to TC intensity can be steady after just 10-20 days, the TC structure can take much longer to equilibrate. The higher intensity in RELAX explains the larger magnitude of the M sink and the smaller domain-integrated M in that case, which further supports the conclusion that in this study, decay is not caused by a lack of angular momentum. We do not attempt to

dispute that domain-wide angular momentum changes are important for the model structure (as evidenced by Chavas and Emanuel, 2014; Smith et al., 2014; Persing et al., 2019), but rather to point out that they do not seem to be the main drivers of intensity variations after the spin-up period in these simulations.

3.5 Conclusion

In conclusion, the large decay in TC intensity seen in some very long simulations (e.g., Hakim, 2011; Smith et al., 2014) results primarily from a change of the environment by the TC's secondary circulation. This decay is ultimately due to the lack of shallow-to-mid-level convection in axisymmetric models, and the lack of horizontal moisture fluxes due to the TC translation, which lead to excessive drying and low entropy in the subsidence region. The TCs do not appear, in this study, to be decaying because of a lack of angular momentum. The drying occurs on the timescale of the secondary circulation, of order 40 days.

The entropy decrease in the air that subsides into the boundary layer leads to an entropy decrease in the core of the storm, as the source of entropy along the inflow leg is insufficient to compensate the deficit in the subsidence region. This leads to a decrease in the intensity of the TC, which is sensitive to the magnitude of the drying in CS and especially in ES. Adding a moisture relaxation term in the subsidence region reduces the decay. If the timescale of the moisture relaxation is small enough, the difference between ES and CS disappears, both in intensity, and in the area encompassed by the $T - s$ cycle. These results suggest a large sensitivity of the thermodynamic cycle of equilibrium TCs to the model configuration and parameterizations.

In general, for theories of potential intensity that just require steady state in the core, like those of Emanuel (1986) or Bryan and Rotunno (2009a), theories can be compared with CS, which is much less restrictive than ES, and allows examination

of the role of the initial environment, with the caveat that the fixed environment assumption is not very robust on timescales of 10 or more days. However, for theories like the Carnot Cycle of Emanuel (1988) or EK57, one requires that steady state be maintained on the timescale of a loop through the secondary circulation, because a steady state environment is necessary to a closed thermodynamic cycle. Considering that reaching ES takes longer than the lifetime of most real tropical cyclones, the CS concept is much more applicable to real storms. Since the effects of the drying affects peak intensity, just 10 days after the start of the simulations, it would be interesting to see if such drying limits the intensity of real-life TCs, or if the shallow convection and continuous translation into new environment are sufficient to counteract the effects of subsidence as does the moisture relaxation in RELAX.

Chapter 4

A Weak Temperature Gradient Framework to Quantify the Causes of Potential Intensity Variability in the Tropics

Abstract

Potential intensity (PI) has been shown to have a linear sensitivity to sea surface temperature (SST) of about 8 m s^{-1} K^{-1}, which is close to the sensitivity of PI in simulations subject to a weak temperature gradient (WTG) approximation. This suggests that most of the PI variance is associated with local rather than global SST variations. We verify that PI perturbations are approximately linear in SST, with slopes of 1.8±0.2 m s^{-1} K^{-1} in RCE and 9.1±0.9 m s^{-1} K^{-1} in WTG. To do so, we simulate the sensitivity of both RCE and WTG states in a single-column model (SCM) perturbed by changing in turn CO_2 concentration, aerosols, prescribed SST and surface winds. While PI is much more sensitive to SST in WTG than in RCE simulations, the SST itself is much less sensitive to radiative forcing in WTG than in RCE because of the absence of large atmospheric feedbacks. Using these results, we develop a linear model based on SST and midlevel saturation MSE perturbations. This allows one to partition SST and PI perturbations between local components occurring under a WTG constraint and global components that are representative of an RCE state. The linear model explains up to 95% of the variability of PI in reanalysis. The SCM-derived linear model coefficients are statistically indistinguishable from coefficients from a linear fit of reanalysis PI to SST and midlevel saturation MSE,

in most ocean basins. Our model shows that local and global forcings contribute similarly to basin average SST variations, while PI variations are explained almost entirely by local forcings.

4.1 Introduction

Potential intensity (PI, Emanuel, 1986, 1988; Bister and Emanuel, 1998; Bryan and Rotunno, 2009a) is a theoretical bound on the maximum achievable wind speed in tropical cyclones (TC). PI has been shown to provide fairly accurate bounds on the maximum wind speed in TCs both in observations (Emanuel, 2000) and in models (Rousseau-Rizzi and Emanuel, 2019), and can be seen as an indication of how favorable the thermodynamic environment is to the maintenance of strong TCs. It is one of the main predictors of TC activity as represented by the power dissipation index (PDI, Emanuel, 2007), an indication of the total amount of energy dissipated by all TCs over a given basin and a given TC season. In other words, PI is an important predictor of the amount of power dissipated by TCs and thus, of their destructive potential. For that reason, understanding the causes of past PI variability is useful to help predict future variability in TC activity.

TC intensity variability is often attributed to sea-surface temperature (SST) varability, and Vecchi and Soden (2007) showed that PI correlates well with sea-surface temperature spatial anomalies and that the slope of the linear regression is near 8 m s^{-1} K^{-1}. PI can be expressed as

$$PI^2 = \frac{C_k}{C_D}\frac{T_s - T_o}{T_o}(h_s^* - h_m^*) \tag{4.1}$$

(Bister and Emanuel, 1998; Wing et al., 2015) where C_k and C_D are the surface exchange coefficients of entalpy and momentum, T_s is the sea surface temperature, T_o is the outflow temperature of the storm, h_s^* is the surface temperature saturation moist static energy (MSE), and h_m^* is the tropospheric saturation MSE. Here we have

made use of the fact that, within the assumption of quasi equilibrium (Arakawa and Schubert, 1974) with a coupled boundary layer, $h_b = h_m^*$, where h_b is the boundary layer MSE.

PI and SST changes result from global (e.g., Sobel et al., 2019) or from local (e.g., Mann and Emanuel, 2006) forcing. Global forcing is generally understood as influencing the whole tropical region as if it were, on average, in a state of radiative-convective equilibrium (RCE). In RCE, a positive forcing causes an increase in sea surface temperature and h_s^*, which tends to increase PI, and an increase in h_m^*, which mitigates the increase in PI. However, the tropical atmosphere has large Rossby radii of deformation, especially at low latitudes. According to the weak temperature gradient approximation (WTG, Sobel and Bretherton, 2000), this means that h_m^* is almost horizontally uniform and can only change globally, not regionally. The implication is that a local forcing that increases SST also increases h_s^* but does not increase h_m^* since the additional energy supplied to the atmosphere is exported in the form of gravity waves. In the absence of a change in h_m^*, PI is much more sensitive to SST changes in a column constrained by WTG than to changes in RCE (Ramsay and Sobel, 2011; Emanuel and Sobel, 2013). Ramsay and Sobel (2011) shows that the sensitivity of PI to SST in an RCE system with imposed SST is around 1 m s^{-1} K^{-1}, while in a WTG-constrained column, it is near 8 m s^{-1} K^{-1}, which is much larger. The PI-SST regression coefficient found by Vecchi and Soden (2007) in reanalysis datasets is also close to 8 m s^{-1} K^{-1}, which suggests that local forcings and their effects on SST dominate PI variability worldwide.

For this reason there is particular interest in understanding the forcings responsible for local SST variability. Here, we will be focusing on SST as a proxy for PI variability because SST variability is well measured and studied. In the tropical North-Atlantic (TNA), SST multidecadal variability and the concurrent effects on PI have been attributed to a variety of causes such as the Atlantic Multidecadal Oscillation (AMO, Zhang and Delworth, 2006), sulfate aerosol forcing (Mann and Emanuel, 2006; Booth

et al., 2012; Dunstone et al., 2013), Saharan dust forcing (Strong et al., 2015, 2018), and surface wind and cloud feedbacks (e.g., Evan et al., 2011, 2016). Some of these explanations such as dust and cloud feedbacks are complementary and some, like the AMO and anthropogenic aerosols, are competing. Hence there exist multiple possible mechanisms that can act to set the SST in the TNA and that could help explain hurricane activity variability. Notably, the "hurricane drought" (decreased hurricane activity) of the 1970s and 1980s, has resisted a single explanation (e.g., Villarini and Vecchi, 2013). In this chapter we attempt to introduce a linear framework that can be used to compare and contrast these influences on SST and PI, using a well known strong constraint on tropical thermodynamics; WTG.

4.1.1 Objectives

In this chapter, we aim to:

1) Show that PI perturbations are approximately linear in SST, with different slopes in WTG and RCE.

2) Show that SST perturbations can be partitioned between local and and global components which allows one to partition PI variations as well.

3) Evaluate the local and global contributions to PI in the MDR and in other basins.

First, section 4.2 discusses the theoretical sensitivity of PI to SST in RCE and WTG, then section 4.3 describes the SCM setup and the data and reanalyses used in the chapter and section 4.4 describes and explains the results of the sensitivity experiments. Next, section 4.5 introduces the linear model for PI and obtains its coefficients, and section 4.6 applies the model to reanalysis products. Finally, section 4.7 discusses the results and section 4.8 summarizes and concludes.

4.2 Analytical estimates

Analytical estimates for PI sensitivity can be obtained fairly easily for WTG-constrained columns. In such a system, the free troposphere is constrained to a constant value of h^*, a thermodynamic variable, but it is not an energetically closed system. In RCE, the main constraint in the free troposphere is that of energy balance, which is much more complex as it relates to equilibrium climate sensitivity (ECS). For that reason, it is easiest to approach PI sensitivity in WTG from thermodynamic forms of the PI equation, and PI sensitivity in RCE from energy balance forms of the PI equation (e.g., Emanuel, 2007).

4.2.1 WTG PI sensitivity

We start by taking the derivative of the log of PI equation (1) with respect to T_s, along with the assumption that the outflow temperature is independent of the sea surface temperature ($dT_o/dT_s = 0$).

$$\frac{2}{PI}\frac{dPI}{dT_s} = \frac{1}{T_s - T_o} + \frac{1}{(h_s^* - h_m^*)}\Big(\frac{dh_s^*}{dT_s} - \frac{dh_m^*}{dT_s}\Big), \tag{4.2}$$

where subscript s denotes the surface and m denotes any point in the free troposphere. We write saturation MSE in the dilute limit

$$h^* = c_{pd}T + L_v r^* + \Phi, \tag{4.3}$$

where c_{pd} is the heat capacity of dry air at constant pressure, L_v is the latent heat of evaporation, r^* is the water vapor saturation mixing ratio, and Φ is the geopotential. Since r^* is a function of T and dry air pressure p_d, h^* is a function of T, p_d and Φ, and we have

$$\frac{dh^*}{dT_s} = \frac{\partial h^*}{\partial T}\frac{dT}{dT_s} + \frac{\partial h^*}{\partial p_d}\frac{dp_d}{dT_s} + \frac{\partial h^*}{\partial p_d}\frac{d\Phi}{dT_s}. \tag{4.4}$$

Neglecting the sensitivity of latent heat to temperature and using the equation of Clausius-Clapeyron, we have, within a few percent,

$$\frac{\partial h^*}{\partial T} \approx c_{pd} + \frac{L_v^2 r^*}{R_v T^2}, \tag{4.5}$$

where R_v is the ideal gas constant for water vapor. At the surface, $dT_s/dT_s = 1$, and the geopotential is constant. We also neglect the contribution of surface p_d changes to saturation MSE changes so that

$$\frac{\partial h^*}{\partial p_d}\frac{dp_d}{dT_s} \approx 0. \tag{4.6}$$

In addition, if we neglect virtual effects, the WTG approximation implies that h_m^* does not change in response to local SST changes. Hence, we can write

$$\frac{dh_h^*}{dT_s} \approx \left.\frac{\partial h^*}{\partial T}\right|_s, \quad \frac{dh_m^*}{dT_s} \approx 0, \tag{4.7}$$

and finally

$$\frac{dPI}{dT_s} \approx \frac{PI}{2}\left[\frac{1}{T_s - T_o} + \frac{1}{(h_s^* - h_m^*)}\left[c_{pd} + \frac{L_v^2 r^*}{R_v T_s^2}\right]\right] \tag{4.8}$$

This allows one to estimate the sensitivity of PI to SST in a column in quasi-equilibrium and under a WTG constraint. For typical values, it yields a sensitivity of about 10.5 m s^{-1} K^{-1}, which is somewhat higher than reported in the literature. Since the derivation relies only on QE and WTG assumptions, and the result depends only on thermodynamic variables, a departure between the PI sensitivity estimated from the thermodynamic state using Eq.4.8, and observed or modelled sensitivity, must arise from a violation of either QE or WTG assumptions. Next, we consider the RCE problem, which is a tad more complicated.

4.2.2 RCE PI sensitivity

In RCE, PI sensitivity is best approached from an energy balance standpoint (Emanuel, 2007). Assuming surface energy balance we can start with

$$PI^2 = \frac{T_s - T_o}{T_o} \frac{F_s + Q_{oc}}{\rho_d C_D |V_s|},$$

where F_s is the net radiative flux at the surface, Q_{oc} is the vertically integrated ocean heat flux convergence and $|V_s|$ is the magnitude of the environmental surface wind speed. In a climate change scenario, the response of all of the terms in this equation needs to be considered, as a change in global radiative forcing will likely affect the surface wind speed and the ocean heat flux convergence as well as the net surface radiative flux. The complexity of the problem is that of the climate sensitivity of the tropics. In equilibrium, we can write

$$F_{atm} + Q_{atm} = F_s + Q_{oc}$$

where F_{atm} is the net radiative heat flux integrated over the whole atmosphere and Q_{atm} is the net dynamical heat flux convergence integrated over the atmosphere. Any study attempting to assess the full impact of a global forcing on PI would need to take into account changes in the large scale circulation. Here, we focus on the narrower topic of column RCE where the wind speed is imposed and there is no atmospheric heat export. Then, when SST is determined by energy balance, $Q_{oc} = 0$, and when SST is imposed, Q_{oc} is implied.

In single-column RCE, with $Q_{oc} = 0$, we can think about the sensitivity of net surface radiative flux in terms of net atmopsheric cooling, which is a function of the atmosphere radiative properties. Hence neglecting changes in near surface density and winds, we have

$$\frac{2}{PI} \frac{dPI}{dT_s} = \frac{1}{T_s - T_o} + \frac{1}{F_{atm}} \frac{dF_{atm}}{dT_s}.$$

That is, the climate sensitivity of the turbulent enthalpy flux, at the surface is equal to that of the net column-integrated radiative cooling of the atmosphere, F_{atm}. Obtaining an analytical estimate for dF_{atm}/dT_s is beyond the scope of this chapter but, using a combination of theory and modelling, Jeevanjee and Romps (2018) show

that

$$\frac{1}{F_{atm}}\frac{dF_{atm}}{dT_s} \approx 3\%\ K^{-1}.$$

If we then take surface wind speed, exchange coefficients and density to be fixed and we substitute this in the formula for PI along with $T_o = 200$ K, $T_s = 300$ K and $PI = 75$ m s^{-1}, we get

$$\frac{dPI}{dT_s} \approx 1.5\ m\,s^{-1}\,K^{-1},$$

which is very close to the simulation estimate of Ramsay and Sobel (2011). Interestingly, 1/4th of the total PI sensitivity comes from that of the thermodynamic efficiency.

4.3 Methodology

Next we obtain the sensitivity of PI to SST in simulations. We use the MIT single-column model (Bony and Emanuel, 2001), which uses the convection parameterization of Emanuel and Živković-Rothman (1999) and the radiation parameterizations of Fouquart et al. (1980) and Morcrette (1991). The simulations use fixed vertical profiles of cloud fraction because allowing the cloud fraction to evolve adds a lot of noise to the sensitivity experiment results. Water vapor and its effects on radiation are allowed to evolve. The ocean is a 2 m deep slab ocean, to allow for sea surface temperature to vary and to maintain energy balance in RCE, except for the prescribed SST simulations. The small depth of the ocean allows the system to reach equilibrium faster. In this chapter we are not concerned with the timescales of the evolution towards equilibrium.

We run four series of experiments in RCE and three series under the WTG constraint. We test the sensitivity of the RCE state to CO_2 concentration, and we test both the sensitivity of RCE columns and of WTG-constrained columns to dust aerosol

direct effect, to prescribed SST variations, and to near surface wind variations. CO_2 is varied from 200 to 800 ppm, dust aerosol optical depth (AOD) is varied from 0 to 1, imposed SST is varied from 28.6 to 32.6 K and surface wind speed is varied from 3 to 14 m s^{-1}. The effect of imposing SST can be likened to imposing some value of column-integrated ocean heat flux convergence. The variety of sensitivity experiments aims to confirm that the choice of dynamical constraint (either RCE or WTG) has a more important influence on the PI-SST relation than does the precise cause of the system perturbation. These experiments are very similar to those of Emanuel and Sobel (2013) who perturbed CO_2, SST, surface winds and the solar constant in RCE and WTG simulations. The main difference between our choice of experiments and theirs is that where they modified the solar constant, we perturbed dust aerosol concentrations. Since dust is a fairly absorptive aerosol, it acts to heat the atmosphere as it cools the surface.

All simulations are perturbed with respect to a control case which we try to choose as representative of the mean state over the TNA main development region (MDR) during the August-September-October hurricane season (ASO). In RCE sensitivity experiments, the chosen control case broadly defines the center of the parameter space to be explored and all simulations are independent from one another. In the WTG-constrained column however, the control case also determines the virtual temperature profile above the 850 hPa level based upon which the WTG vertical velocities will be computed. In reanalysis (NOAA 20CR), the mean near surface wind speed during ASO in the MDR is 4.8 m/s, so we take our control case to have a near surface wind speed of 5 m/s. We'll use an dust optical thickness of 0.3 as the ASO MDR-averaged baseline based on Evan and Mukhopadhyay (2010). The control case has 360 ppm CO_2, which is representative of the near past.

In our simulations and in reanalysis data, PI is computed using a nonlinear iterative algorithm developed by Bister and Emanuel (2002), which takes as an input sea surface temperature and vertical profiles of pressure, temperature, and mixing ratio.

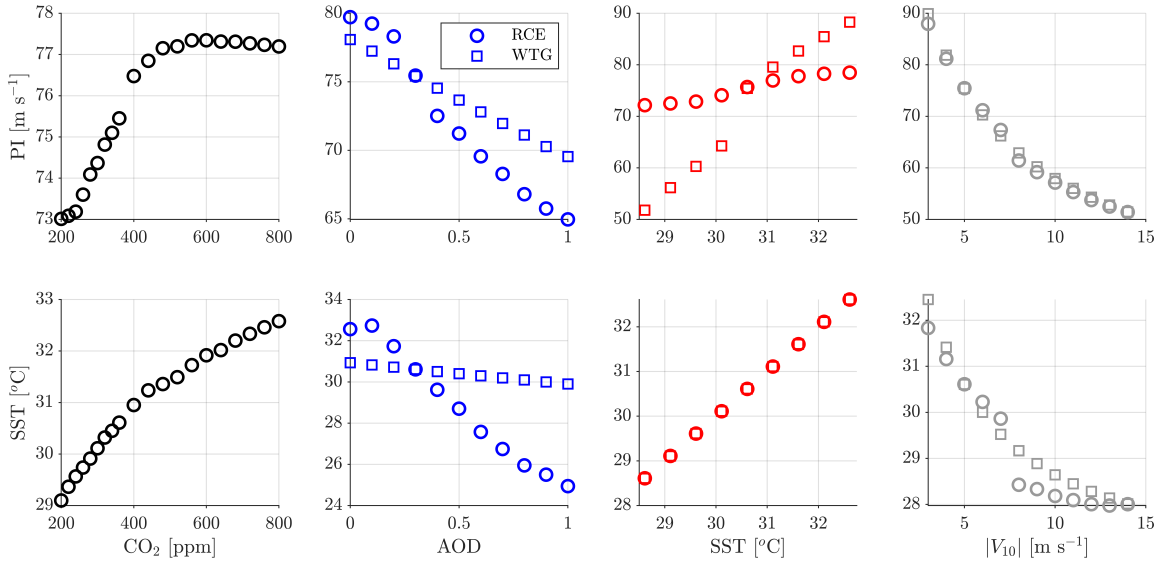

Figure 4-1: Sensitivity of PI (top row) and SST (bottom row) to changes in: CO_2 concentration (black), aerosol optical depth (blue), imposed SST (red) and near-surface wind speed (gray). All plots superimpose the RCE experiments (full line) to the WTG experiment (dashed line), except for the CO_2 experiment, which is only performed in RCE.

In cases where the boundary layer decouples from the free troposphere, PI can be multi-valued. For example, an existing storm translating into such an environment could be sustained and strong (upper PI value), but a new storm could likely not develop (lower PI value) in this environment. When computing PI in simulations, we purposely select the lowest of the possible PI values in the few cases where the BL is decoupled because it is more appropriate to the development of our linear model. Situations where decoupling affects the results will be discussed.

4.4 Sensitivity experiment results

Figure 4-1 introduces the results of the sensitivity experiments. Each point in the figure represents either PI or T_s at equilibrium in one simulation, plotted against the corresponding perturbed parameter.

4.4.1 CO_2 sensitivity

In the CO_2 panels, we can see PI levelling off as temperature increases. This is partly due to the effect of high CO_2 concentrations where the net infrared flux to the surface stops increasing with temperature which causes the PI profile to flatten even though SST keeps increasing (e.g., O'Gorman and Schneider, 2008). In addition, the fixed cloud profile used in the simulations increases stability near the outflow of the TCs, which prevents PI from increasing further. In our simulations, a doubling of CO_2 is associated with an SST change of 1.5 to 2 K, which is on the low end of the response expected from the Earth's climate.

4.4.2 Imposed SST sensitivity

In the next experiment, SST is imposed, which is why the SST plot has a unique slope of 1. The values are the same for both RCE and WTG. The PI-SST relationship conforms reasonably well with the literature, with a slope of about 1.6 m s^{-1} K^{-1} in the RCE experiment, and a slope of about 9 m s^{-1} K^{-1} in the WTG experiment. The RCE slope is very similar to the 1.4 m s^{-1} K^{-1} slope of (Ramsay and Sobel, 2011) and small modelling differences, such as control simulation background wind can easily account for the difference. The WTG slope is somewhat higher than the 7.6 m s^{-1} K^{-1} introduced by (Ramsay and Sobel, 2011) which may be due to the fact that in our simulations, the boundary layer decouples from the free troposphere at low temperatures, which causes a slightly sharper decrease in PI. These plots do not provide much new insight, but confirm that the simulations are not very different from results from the literature.

4.4.3 Aerosol sensitivity

Now looking at the sensitivity of SST to aerosol optical thickness variations, we notice that the slope of SST in WTG is much smaller than that in RCE (-1 K per unit AOD by comparison to -8 K). We surmise that this is due to the atmospheric heat transport by gravity waves implied by the WTG parameterization, which prevents any strong

feedback between the atmosphere and the ocean and makes SST less sensitive to aerosol forcing. An interesting consequence of this difference in SST sensitivities to aerosol forcing is that the PI sensitivity to aerosol forcing in RCE is larger than that in WTG, even though the PI-SST slope is much steeper in WTG (as will be seen in Fig.4-2). Interestingly, this suggests that the reason why PI variability is dominated by local variability is that the local variability of forcings (like ocean heat flux convergence or aerosol forcing) is much larger than the global variability, and not because PI is intrinsically more sensitive to a given forcing in WTG than in RCE (if anything, it is less sensitive).

4.4.4 Wind sensitivity

The wind sensitivity experiments test wind speed variations from 3 [m s^{-1}] to 14 [m s^{-1}] in unit increments. Contrarily to other parameters which produce very different responses in RCE and in WTG, the results of the wind sensitivity experiments are similar in both cases. Not only are both SST-$|V|$ relations similar, the PI-$|V|$ relations are as well, and both cases have PI-SST slopes close to 9 m s^{-1} K^{-1}. One way to understand this similarity is that, in RCE, if we neglect the change in longwave radiation emitted by the surface and assume a constant bowen ratio, then the atmospheric properties remain identical as surface wind speeds change, and the ocean temperature adjusts to keep the turbulent heat flux constant. This lack of tropospheric temperature change is very similar to what would happen in a WTG scenario, and correspondingly, surface wind perturbations in WTG do not cause large compensating vertical velocities. In other words, under the assumptions mentioned above, both cases are equivalent.

4.5 Linear PI model

The idea we are pursuing here is to partition annual to multidecadal potential intensity variations between global perturbations to the state of the tropical atmosphere, approximated to be in RCE, and local perturbations to that RCE state, approxi-

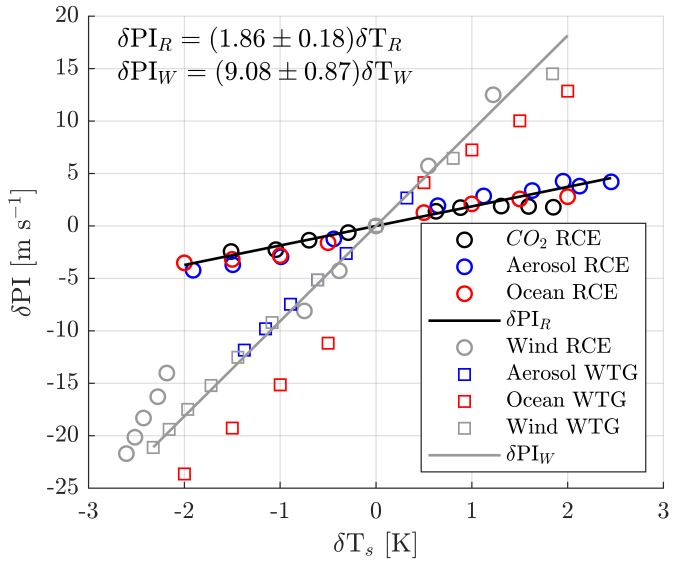

Figure 4-2: Plot of δPI against δT for CO_2 (black), dust aerosol (blue), SST (red) and surface wind (gray) sensitivity experiments in RCE (circles), and in WTG (squares). Linear fit for the $\delta PI - \delta T$ relations in RCE (black) and in WTG (gray).

mated to occurs under a WTG constraint. To achieve this goal, we start by showing that changes of PI in both RCE and WTG can reasonably be assumed to vary linearly with SST within the domain of observed SST variation. Hereafter, we write $PI = PI_0 + \delta PI$ and $T = T_0 + \delta T$, where PI_0 and T_0 are climatological mean values in a given basin, and δPI and δT are departures from that mean.

Figure 4-2 shows the change of PI for a given change in SST, with respect to a reference state and for all sensitivity experiments. The domain of the simulations plotted is restricted to ± 2 K to outline realistic variations with respect to the control case. As can see, all the experiments fall more or less along two distinct linear slopes (especially near the origin). The shallower slope (1.8 [m s^{-1} K^{-1}]) is a regression of δPI on δT for all experiments in RCE, except the wind. The steeper slope (9.0 [m s^{-1} K^{-1}]) is a similar regression for the aerosol, SST, and wind experiments in WTG. The wind experiment was excluded from the RCE case because it behaves similarly to the WTG case, and that remote wind changes should not impact PI much, by comparison to remote SST or radiative forcing changes. The relation between δPI and δT for imposed SST in WTG does not look as linear, because a decrease in

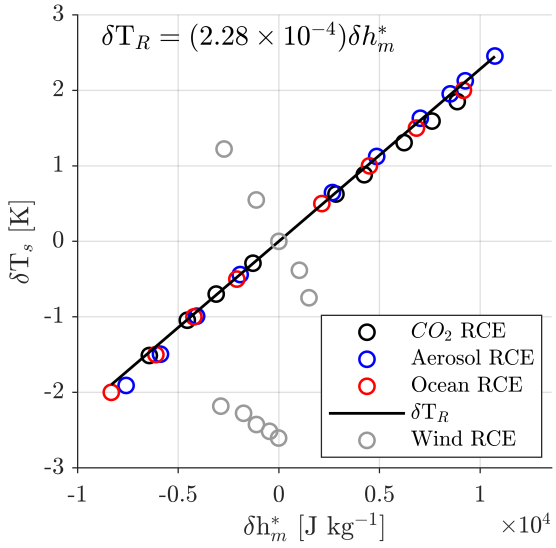

Figure 4-3: Same RCE simulations and colors as in Fig.1, but in $\delta SST - \delta h_m^*$ space.

SST from the control case leads to the uncoupling of the boundary layer from the troposphere. Those regression slopes are similar to, if somewhat larger than, the re-analysis PI sensitivity (Vecchi and Soden, 2007) or other modeled relations (Ramsay and Sobel, 2011). To compute the regression, we have selected a similar number of simulations for each sensitivity experiment included, roughly equally spaced to span the δT domain. We note that, as reported in the literature (e.g., Sobel et al., 2019), there are differences in the PI-SST relations between experiments in RCE. For example, RCE PI is more sensitive to SST under an aerosol forcing than under a CO_2 forcing. However, this is not a problem for our model since the difference between the RCE and WTG cases is much larger.

This suggests that we can express PI as two linear functions: one for WTG and the other for RCE perturbations. To achieve this, we need to partition observed SST perturbations between their RCE and WTG components. To do so, we consider the fact that because of the WTG constraint, any large change to the mid-tropospheric saturation MSE (δh_m^*) must be due to changes in the RCE state. To simplify the problem, we seek a unique function relating δh_m^* to δT_{RCE}.

Figure 4-3 shows the RCE sensitivity experiments introduced earlier, plotted in

$\delta T - \delta h_m^*$ space. The WTG simulations are omitted as h_m^* doesn't change with SST in WTG. Second we note that most RCE simulations fall on a single profile that is quite linear over the plotted domain. That profile does not vary much between sensitivity experiments. The regression coefficient for δPI and δT for all RCE experiments but the wind is about 2.28×10^{-4} kg K J^{-1}. Finally, we note that h_m^* changes non-monotonically with SST in the RCE-wind sensitivity experiment. This is due to the model transitioning between two stable configurations and is a consequence of using a single column model. We circumvent that issue by considering that local changes in winds are much larger than tropics-wide changes (which is supported by reanalysis) and by neglecting the wind contribution to RCE changes altogether. This leaves us with two linear slopes for the $\delta PI - \delta T$ relation in RCE and WTG and one for the $\delta T - \delta h_m^*$ relation in RCE.

4.5.1 A linear model informed by theory and the a single-column model

To develop a linear model for δPI as a function of δT and δh_m^*, we first partition δT, the total SST change, between SST changes in RCE, and a perturbation with respect to the RCE state. We pose

$$\delta T = \delta T_R + \delta T_W, \tag{4.9}$$

where δT_R is the SST change in RCE, and the δT_W is the remainder of the total SST change. Then, δT_R can be related to δh_m^* by posing

$$\delta T_R = C_m \delta h_m^*, \tag{4.10}$$

where m refers to the mid-troposphere and from Fig.4-3, we have $C_m = 2.28 \times 10^{-4}$ kg K J^{-1} is a constant. Defined in that way, the PI sensitivity to δT_R should be the PI sensitivity to SST in RCE. The remainder δT_W, which is given by

$$\delta T_W = \delta T - C_m \delta h_m^*, \tag{4.11}$$

is not associated with any change in h_m^* and will control PI as if in WTG, hence the subscript W. Adding in the linear coefficients for PI sensitivity in RCE and WTG from Fig.4-2, we introduce the fundamental partition we want to make:

$$\delta PI = C_R \delta T_R + C_W \delta T_W, \tag{4.12}$$

where C_R =1.8 m s^{-1} K^{-1} and C_W =9.0 m s^{-1} K^{-1}. The quantity δT can be readily retrieved from models or observations. The quantity δh_m^* is mostly a function of temperature on a given pressure level (and to a small extent, of moisture), and can also be retrieved from reanalysis products. Combining the equations, we obtain

$$\delta PI = C_R C_m \delta h_m^* + C_W(\delta T - C_m \delta h_m^*), \tag{4.13}$$

where the first term on the RHS is the contribution to PI changes from changes to the RCE state, and the second term is the contribution from changes in the WTG state. Rearranging to combine the predictors we get

$$\delta PI = C_m(C_R - C_W)\delta h_m^* + C_W \delta T. \tag{4.14}$$

Here the physical interpretation of the two terms changes to provide further insight. Since $C_W > C_R$ and $C_m > 0$, we can see that the coefficient of the first term is negative, which reflects the fact that a positive δh_m^*, in the absence of a compensating increase in SST, will cause a decrease in PI. Conversely, the second coefficient is the large positive increase in PI that occurs when SST increases locally, while the mid-troposphere remains fixed. The coefficients for this form of the equation can be obtained from both the SCM and from a linear fit based on reanalysis data, and compared to verify the model.

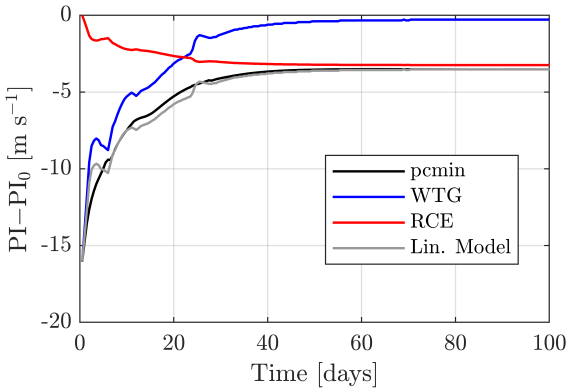

Figure 4-4: Evolution of PI towards RCE in a fixed SST single-column simulation, when SST is perturbed by -2 K. Timeseries of algorithm PI (black) and linear model PI (gray) and the equilibrium (red) and transient (blue) components of linear model PI. The red and the blue lines correspond respectively to the first and second terms on the RHS of Eq.4.12.

4.5.2 Unsteadiness

We note that the component of SST or PI we called "WTG" is for now just a component that departs from the RCE state and does not entail that the SST perturbation is local in space. This will have to be verified using reanalysis data. Consider the application of the linear model to the time-dependent evolution of single-column simulation towards RCE. If our linear model is correct, we should be able to reproduce PI variations based only on the departure of δT and δh_m^* from the initial conditions. For example, let's consider the evolution of the fixed SST simulation where SST is perturbed by -2 K. Initially, as shown by Fig.4-4, we have $\delta PI = C_W \delta T_W$ and the PI perturbation does not reflect any RCE change. For this plot, we have arbitrarily taken $C_W = 7.5$ m s^{-1} K^{-1} for best results. Our only goal here is to show that PI can be represented at each point in the evolution by a linear model. As time goes on, the RCE component increases and the transient component decreases. At the end, as the system has reached RCE, $\delta PI = C_R \delta T_R$, and there is no more departure from RCE.

In between the initial time and equilibrium, δT_R increases and δT_W decreases, and if we substitute both time dependent values in Eq.4.12, we can reproduce the evolution of PI as captured by the Bister and Emanuel (2002) algorithm.

This means that a linear model can't, on it's own, distinguish between WTG perturbations and transience, but it can identify the part of SST variations that is coherent with an RCE state. To show that the remainder of SST variations corresponds to a state in WTG, we need to apply the linear model to reanalysis data, and show that the use of a tropical average value of δh_m^* is sufficient to capture PI variations.

4.6 Application to reanalysis products

To verify that the linear model captures PI variations, we apply it to ERA5 reanalysis (Hersbach et al., 2020) monthly-averaged data. The resulting linear model PI (LPI) variations are then compared to a reference PI dataset computed using ERA5 data and pyPI (Gilford, 2020), a Python package for the nonlinear iterative algorithm developed by Bister and Emanuel (2002). The PI dataset was graciously provided by Daniel Gilford. In this dataset, which is most appropriate for the study of the maintenance of TCs, the highest value of PI is selected when a decoupled BL results in a multi-valued PI. As we will show, this causes linear PI variability to be underestimated in ocean basins where decoupling occurs frequently. To compute LPI for each basin, the saturation MSE predictor δh_m^*, which is assumed to be uniform over the tropics, is averaged from -20 to 20 N and from -180 to 180 E, and the sea-surface temperature predictor δT is averaged over each tropical ocean basin separately. The averaging of PI and SST excludes land in all basins. As shown in Fig.4-5, we define five ocean basins in total; the North-Atlantic (NA), eastern North-Pacific (EP), western North-Pacific (WP), northern Indian Ocean (IO), and a single large basin for the southern hemisphere (SH), in the Pacific. To make sure that the quantities computed are relevant to TC activity, PI variations are computed from predictors averaged over the tropical storm season of each basin respectively. Table 4.1 summarizes the basin and season definitions.

Basin	Latitudinal extent	Longitudinal extent	averaging season
NA	6 to 18 N	-60 to -20 W	Aug-Oct
EP	5 to 15 N	-170 to -90 W	Jun-Sept
WP	5 to 15 N	130 to 180 E	Jul-Nov
IO	5 to 20 N	50 to 110 E	Apr-Nov
SH	-18 to -5 S	60 to 180 E	Jan-May

Table 4.1: Basin definitions in terms of latitudinal extent, longitudinal extent, and tropical storms season.

We then apply the linear model to the spatially and seasonally averaged predictors to compute one value of PI per basin per year. In the reference PI dataset, graciously provided by Daniel Gilford, pyPI is applied to ERA5 monthly-averaged SST and vertical profiles of p, T and r at each latitude-longitude point. The PI dataset is also averaged over each basin and over the corresponding tropical storm season. A comparison between LPI and the algorithm PI allows one to evaluate the linear model, but to ensure that our SCM-derived coefficients are valid, we also compute a linear fit of the algorithm PI to our two LPI predictors, δT and δh_m^*. This is equivalent to employing Eq.4.14, with the coefficients of both predictors determined statistically rather than numerically. To sum up we are left with three ways to compute potential intensity: 1) LPI, 2) algorithm PI and 3) linear fit PI.

Figure 4-6a) shows that, in the tropical North-Atlantic main development region (MDR), LPI captures very well the variations of the algorithm PI ($R = 0.97$) and is almost indistinguishable from the linear fit PI. This shows that δT_s and δh_m^* are a good choice of predictors, and also that the SCM-derived coefficients are very close to the linear fit coefficients (as we will see later). This suggest that we can interpret past PI variations in light of the SCM-derived coefficients, which provide physical meaning.

In Fig. 4-6b), we have used Eqs. 4.10 and 4.11 to partition the variations of SST

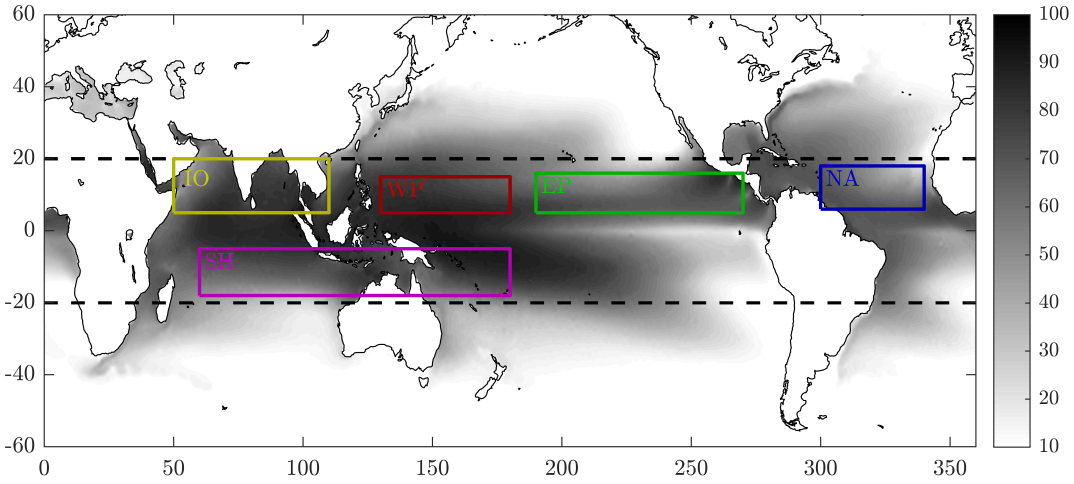

Figure 4-5: Tropical ocean basins for PI analysis plotted over a map of average PI in ERA5 reanalysis from 1979 to 2018. SST is averaged seasonnaly and over each basin: North-Atlantice (NA, blue), East Pacific (EP, green), West Pacific (WP, red), Indian Oceam (IO, yellow), and a large basin for the Southern Hemisphere (SH, magenta). Midlevel saturation MSE is averaged over the area enclosed by the two black dashed lines.

into WTG and RCE contributions in the MDR. We can see that while the variations of δT_R have been smaller than those of δT_W over the last 40 years, the magnitudes are comparable. δT_R exhibits a positive trend in time which is likely due to global warming. The detrended variability in δT_R correlates well with the Nino3.4 index (not shown) because large-scale ocean heat flux has an important influence on the global atmosphere. Determining the causes of δT_W, or δPI_W, variability exceeds the scope of the present chapter and will be the topic of subsequent research. Causes can include aerosol radiative forcings, wind induced surface heat exchange and ocean circulations like the Atlantic Meridional Overturning Circulation.

Finally, in Fig. 4-6c) we look at the partition of PI variations into global (δPI_R) and local (δPI_W) contributions. Clearly, in the MDR, the global contribution to PI variations is negligible compared to the local contribution, in the last 40 years. However, even though δPI_R is small, we still need to know δT_R, in order to be able to estimate δT_W and have an accurate estimate of δPI_W, which dominates the variabil-

ity. Note that the fact that global effects on PI are small in the Atlantic MDR does not mean that they are small polewards of the tropics.

4.6.1 Other basins

Figure 4-8 shows the coefficient of determination (R^2) of the linear model in all ocean basins, and as we can see, LPI reproduces algorithm PI well in all basins. The basin with the smallest R^2 is the Eastern North Pacific with 80% of the interannual PI variance captured by LPI. The maximum variance explained by the model is 95%, in the North-Atlantic. It is not surprising that the linear model works best in the North-Atlantic MDR since the simulations from which the model coefficients are derived vary around a control simulation designed to resemble the conditions over that basin.

To illustrate the relative roles of global and local influences, Fig. 4-9 shows the partition of SST between local and global contributions, in the four additional basins. Since the global contribution to SST depends only on δh_m^*, which is averaged over the whole tropics and is common to all basins, the only difference between the δT_R timeseries across different basins is just the averaging season. If two basins had the same TC season, they would have the same δT_R every year. In basins that have much smaller SST variability than the NA, like the IO or the SH, the local contribution to SST changes δT_W is smaller than δT_R. In the SH basin δT_R very clearly shows El Nino events, notably in 1983, 1998, 2010 and 2016, because the averaging includes the months of January and February, during which the events tend to reach peak magnitude. We have not included a figure showing the partition between δPI_R and δPI_W for all basins because the information can be retrieved by multiplying δT_R by $C_R = 1.8$ m s^{-1} K^{-1} and δT_W by $C_W = 9.0$ m s^{-1} K^{-1}. The timeseries of δPI_R is similar across all basins and is everywhere smaller than δPI_W with the difference being largest in basins with large SST variability like the ENP.

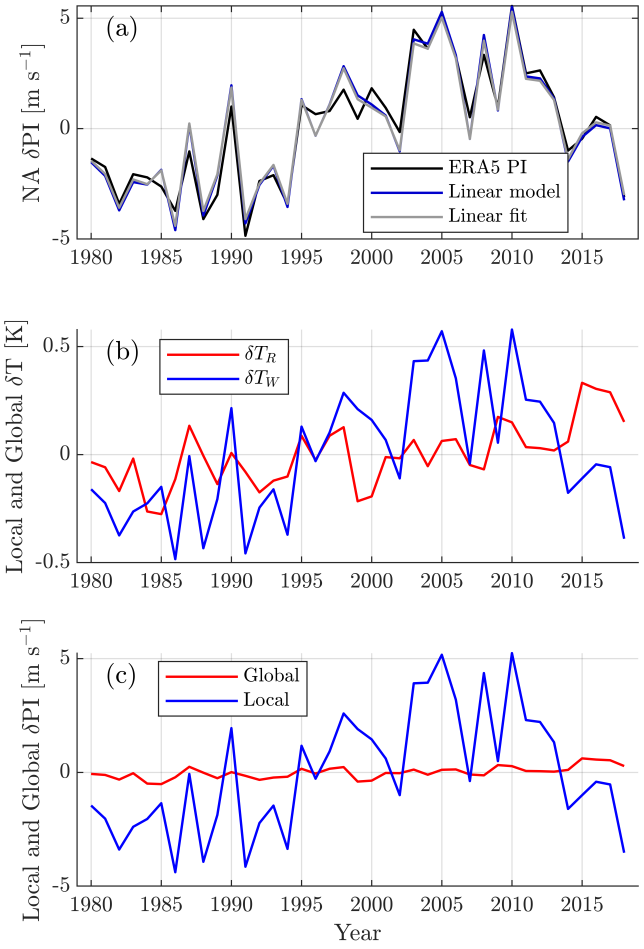

Figure 4-6: (a) Timeseries computed over the MDR and ASO of “true" algorithm δPI (black), of δPI estimated using the SCM-derived linear model (blue) and of δPI estimated using an in-sample linear fit on δT and δh_m^* (gray). (b) Timeseries of SST change (δT) over the MDR and averaged over hurricane season partitioned between its RCE (red) and WTG (blue) components. (c) Partition of δPI averaged over the MDR and ASO, between its RCE (red) and WTG (blue) components.

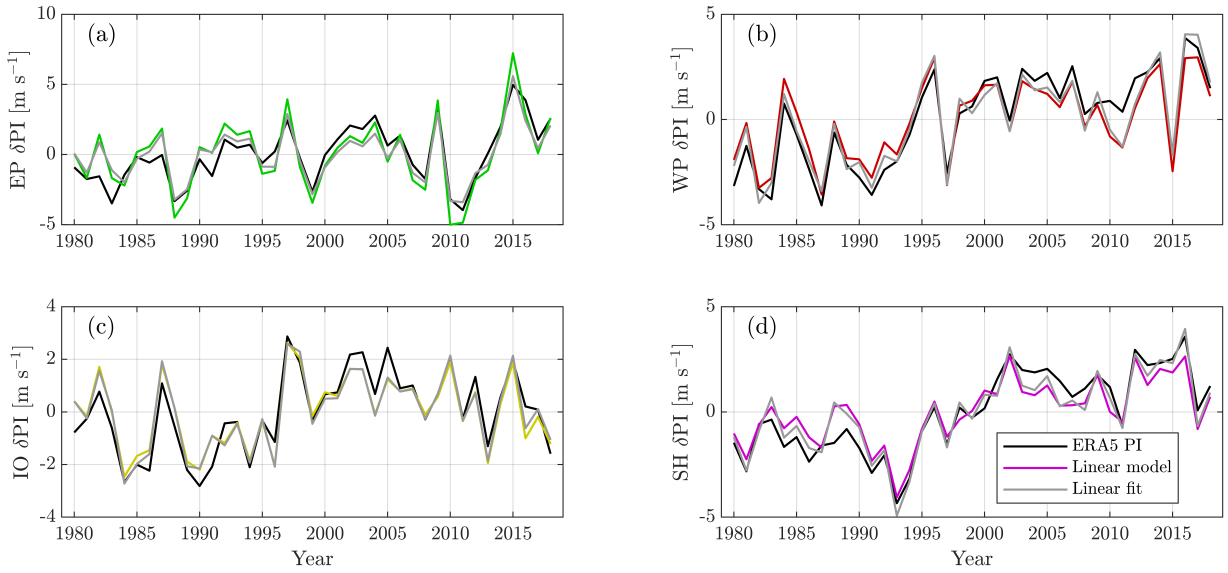

Figure 4-7: Timeseries computed over each basin of "true" algorithm δPI (black), of δPI estimated using the SCM-derived linear model (colors) and of δPI estimated using an in-sample linear fit on δT and δh_m^* (gray) for (a) the Eastern North Pacific, (b) the Western North Pacific, (c) the Northern Indian Ocean and (d) the Southern Hemisphere basin. The colors of LPI plots over each basin correspond to those used in Fig.4-5

.

4.6.2 Reanalysis coefficients

So far we have shown that LPI correlates well with algorithm PI across all basins. Next, we want to show that the coefficients derived from the SCM simulations have a physical meaning that can be used to interpret PI variations in reanalysis data. To do so, we obtain linear fit coefficients by regressing PI on δT and δh_m^* in ERA5. This yields a formula of the form $\delta PI = C_1 \delta T + C_2 \delta h_m^*$. This linear fit PI is plotted in gray in Fig.4-6a) and unsurprisingly also captures PI variation very well. Comparison of the linear fit with Eq.4.14 yields that, if the SCM model assumptions are valid, then $C_1 = C_W$ and $C_2 = C_m(C_R - C_W)$. Figure 4-10a) shows coefficient C_W derived from SCM simulations (same as in Fig.4-2) along with coefficient $C_1 = C_W$ for each ocean basin, in black. The coefficients are plotted with 95% confidence intervals. This shows that, except for EP, the coefficients from all ocean basins are indistinguishable from the SCM-derived coefficient. The reason why EP has a different coefficient will be ex-

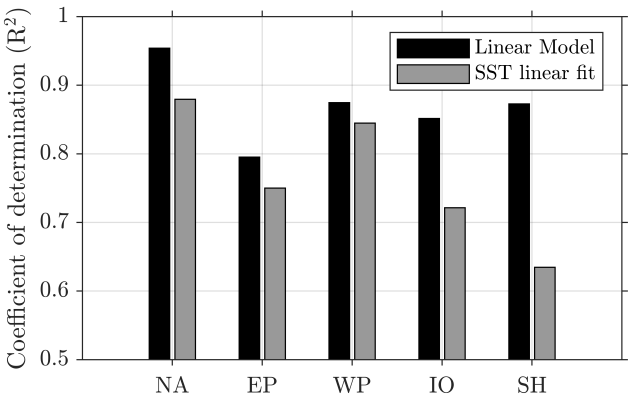

Figure 4-8: Coefficient of determination between algorithm PI and LPI (black bars) and between algorithm PI and SST (gray bars) for each basin.

plained below. The red "x" denotes an analytical estimate for coefficient C_W, obtained from the control simulation and Eq.4.8 and is just slightly higher than the model-based estimate. Figure 4-10b) shows the combination of coefficients $C_m(C_R - C_W)$ derived from SCM simulations along with coefficient $C_2 = C_m(C_R - C_W)$ for each ocean basin. Although there is a lot of uncertainty on the coefficients in some basins, like in the EP, all uncertainty bounds overlap so that all coefficients are indistinguishable from a value of about -1.5 m kg s^{-1} J^{-1}. The negative value implies that, for an unchanged SST, if h_m^* increases, potential intensity must decrease.

In Fig.4-10a), we have also plotted a coefficient of linear regression of PI on SST alone such that $\delta PI \approx C_3 \delta T$. Since δT is positively correlated with δh_m^* (not shown), the coefficient C_3 must be smaller than C_W. If the correlation was perfect we should have $C_3 \approx C_R$, so C_R and C_W are essentially lower and upper bounds on C_3. In our figure 4-10a), the SH basin, which has the largest correlation between δh_m^* and δT has the largest difference between C_3 and C_R, and conversely for the EP basin which has the smallest correlation. This is worth pointing out because it contextualises the use of SST alone as a predictor of tropical cyclone intensity: it only works well if that SST is independent of mid-tropospheric conditions. To support this, we look at the coefficients of determination for SST alone in Fig.4-8 and notice they are always smaller than the R^2 of the SCM-derived model which also includes δh_m^*. Further, the

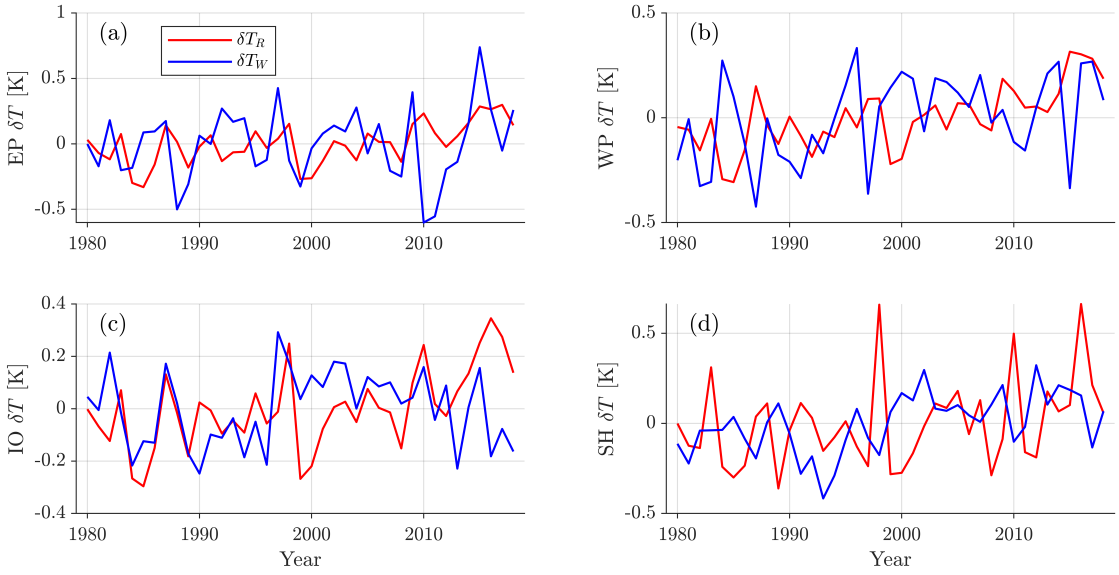

Figure 4-9: Timeseries of SST change (δT) averaged over each basin and the corresponding TC season partitioned between their RCE (red) and WTG (blue) components for (a) the Eastern North Pacific, (b) the Western North Pacific, (c) the Northern Indian Ocean and (d) the Southern Hemisphere basin.

difference is again largest in the SH basin, where the correlation between δh_m^* and δT is strongest.

4.7 Discussion

Our results outline the importance of coefficient C_W in determining the magnitude of PI variations associated with a given SST perturbation. In addition, C_m allows one to define that perturbation based on the mean tropical state and is also important. On the other hand, C_R is not very important up to multidecadal time scales because RCE PI changes account only for a small fraction of the total. The local coefficients C_W found here are larger than those presented in (Vecchi and Soden, 2007), which relied on fitting algorithm PI to a temperature anomaly computed with respect to the tropical average at each time step. This method is the equivalent to setting $\delta T_W = \delta T - \delta\bar{T}$, where $\delta\bar{T}$ are tropical mean SST changes. In addition, it assumes $\delta PI_R = C_R\delta\bar{T} \approx 0$, and we indeed have found δPI_R to be small. So the main

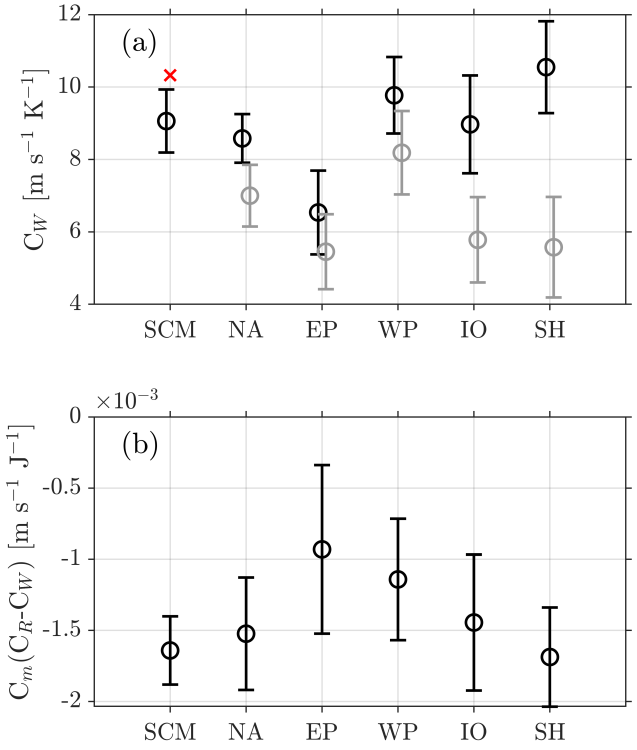

Figure 4-10: a) Linear model coefficients C_W derived from the SCM simulations (black, SCM label) and derived from ERA5 PI regression on both δT and δh_m^* (black, basin labels), analytical estimate of C_W using Eq.4.8 (red x), and coefficient of ERA5 PI regression on δT only (gray). b) Combination of linear coefficients $C_m(C_R - C_W)$ derived from the SCM simulations (SCM label) and derived from ERA5 PI regression (basin labels). The error bars denote 95% confidence interval on the regression coefficients

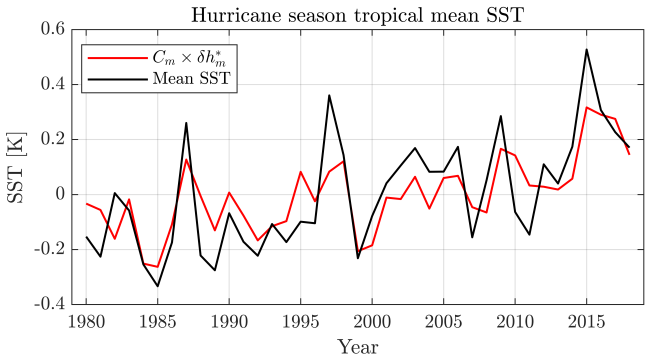

Figure 4-11: Comparison between tropical mean SST (black), and an estimate of SST representative of global changes by our linear model (red). Both quantities are averaged over the North-Atlantic hurricane season.

difference lies in the assumption that $\delta\bar{T}$ is representative of δh^*_m, which depends not only on SST, but on the degree of coupling of the sea surface to the atmosphere.We illustrate this assumption in Fig.4-11, where we show a timeseries $\delta\bar{T}$ averaged over tropical North-Atlantic hurricane season, along with $C_m\delta h^*_m$ averaged over the same season. As we can see, in general, $\delta\bar{T} \propto \delta h^*_m$. The linear regression coefficient between both variables over the last 40 years is $(2.69 \pm 0.64) \times 10^{-4}$ kg K J^{-1}, which is indistinguishable from the value of the coefficient C_m. This is interesting because the value of the linear regression coefficient between $\delta\bar{T}$ and δh^*_m is expected to depend on the level of coupling between the sea-surface and the mid-troposphere. Hence this result suggests that large-scale changes in coupling, for example due to global trade wind changes, were not very important in the last 40 years. Further, we can notice that the largest departures between $\delta\bar{T}$ and $C_m\delta h^*_m$ occur during El-Nino years, where large changes in the pattern of SST is bound to change the level of coupling on a large scale. On multidecadal timescales, the assumption $\delta\bar{T} \propto \delta h^*_m$ seems a good one, but it is insufficient to capture the effects of interannual variability on PI.

4.7.1 The East-Pacific

The EP basin stands against an oceanic boundary with lots of cold water upwelling, which causes the BL to decouple from the free troposphere much more frequently than occurs in other basins. This decoupling causes PI to be multi-valued and to vary non-

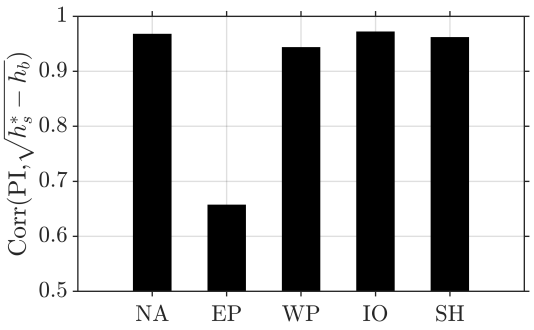

Figure 4-12: Correlation coefficients between PI and the square root of thermodynamic disequilibrium for each basin.

monotonically in temperature, which results in a lower PI variability than predicted by the SCM linear model. In other words, this is the reason why the EP linear fit C_W coefficient is considerably lower than the linear model C_W in Fig.4-10a). Figure 4-12 shows that the BL decouples far more often in the EP than in other basins, by comparing the correlation coefficients between algorithm PI and the square root of the thermodynamic disequilibrium in each basin. Examining the PI computation algorithm (e.g., Gilford, 2020) shows that a frequent decoupling should decrease that correlation. And we can see that correlations are about 0.95 for all basins except the EP, where it is 0.65.

4.7.2 Applications

The goal of this chapter is to provide a framework for quantifying the causes of PI variability in the tropics. So far, we have shown that PI variations are well captured by a novel linear model based on two simple and intuitive predictors. This linearity of PI, along with the fact that the model coefficients have a clear physical meaning, constitute the basis of our framework. First, the linearity of PI will allow to study the different local influences on SST perturbations independently from one another and then convert the SST perturbations corresponding to each influence to PI perturbations. For example, if it is known that dust aerosol forcing accounts for twice as much TNA SST variability as ocean heat flux convergence, then it also accounts for twice as much PI variability. Then, the physical meaning of the model coefficients

allows us to obtain information on the cause of PI changes since SST and PI can be partitioned between an RCE component, corresponding to large-scale changes to the tropical atmosphere, and a WTG departure from those large scale changes.

The coefficient C_W derives from Clausius-Clapeyron and could apply to any departure from RCE, but the fact that the tropical average h_m^* predictor greatly improves the linear model, confirms that these departures occur in WTG. Throughout all basins, PI variations are dominated by WTG variations, at least over the last 40 years, which suggests that changes in SST patterns due to global change might be more important for PI and TC activity than the changes in global mean temperature themselves. This highlights that any small domain simulation or idealized model that attempts to capture the response of SST and PI to local parameter changes should be constrained by WTG. The coefficient C_m, however, is a fundamental property of Earth's atmosphere, that can be related to atmospheric cooling and indicates the slope of the relation between midlevel saturation entropy and SST. This coefficient outlines why PI is relatively insensitive to global warming.

We note that those coefficients were derived from equilibrium simulations but do not actually require a steady-state to be applicable. For example, if large scale oceanic fluxes like those due to ENSO increase rapidly and heat up the atmosphere, small remote basins like TNA will see a drop in PI before their temperature adjusts, and an increase afterwards. Conversely, rapid changes in large coupled basin SST will result in large basin PI changes before the atmosphere has time to adjust, and more modest ones afterwards. For example, the 2015-2016 El-Nino event is clearly visible in Fig. 4-9, where there is a large increase in WTG-like perturbation temperature in the EP basin, and a correspondingly large decrease in the WP basin. In those plots, the fraction of SST that correlates with h_m^* is not very large, outlining that the atmosphere has not adjusted yet to these perturbed SSTs during the Boreal summer. Early the next year, during the averaging season of the SH in the Austral summer, we can see that the RCE temperature component is much larger while the absolute

anomalous component is much smaller than in the two other basins, earlier in the year. This suggests that the SSTs are closer to equilibrium with the atmosphere then, in the SH basin.

4.8 Conclusion

In this chapter, we introduced a new linear model for potential intensity, based on SCM simulations, and on the sensitivities of PI to SST in atmospheres in RCE and under WTG constraint. The model coefficients are derived from a control simulation designed to be similar to Atlantic conditions, and from a set of sensitivity experiments to CO_2 in RCE and to dust optical depth, imposed SST changes, and surface winds, in RCE and under WTG constraints. The resulting linear model allows us to partition SST and PI changes into local and global components, and explains up to 95% of the inter-annual to multidecadal basin-averaged seasonal PI variance. The basin where the model works best is the NA, which may be due to the fact that the control simulation was designed to have similar conditions as the NA. The basin where the model captures the least variance is the EP, which may be due to cold water upwelling intermittently decoupling the boundary layer from the midlevels, and decreasing PI sensitivity. Apart from the EP, the linear model coefficients derived from SCM simulations are indistinguishable in all basins from linear fit coefficients derived using ERA5.

Future work will demonstrate applications of this framework, including estimating the relative contributions of various mechanisms to the historical PI variations, and quantifying the thermodynamic effect of ENSO on Atlantic hurricane activity. In addition, the results suggest that it would be interesting to evaluate the sensitivity of PI and SST to direct and indirect dust aerosol effects, and the associated cloud feedbacks, in WTG-constrained cloud resolving model simulations.

Chapter 5

Natural and Forced Contributions to the Hurricane Drought of the 1970s-1980s

Abstract

Multidecadal climate variability around the Atlantic basin is due to volcanic and anthropogenic sulfate aerosol forcing. However, to explain the full variability of hurricane activity at those time scales, the radiative effects of Saharan mineral dust over the tropical North-Atlantic must also be considered. In this chapter, we argue that sulfate aerosol and dust radiative forcings are not independent. Instead, we propose that by causing drought conditions in the Sahel, which enhanced dust emissions, past sulfate aerosols emissions contributed not only directly, but also indirectly to hurricane variability. Using Sahel precipitation records as a proxy, we estimate the dust optical depth over the hurricane main development region. This dust proxy correlates well with an AMO-like mode of sea-surface temperature (SST) anomaly variations. Using single-column model simulations, we then estimate the sensitivity of SST to dust optical depth, and we find that about 40% of the SST anomaly variability at time scales from 30 to 100 years can be explained by dust direct forcing, from 1900 to the present day. Since simulated sulfate aerosol radiative forcing alone is insufficient to explain main development region SST variability, and that Sahel drought conditions are known to be caused by sulfate forcing, we conclude that the dust feedback is necessary to explain the observed past SST and hurricane activity variations.

5.1 Introduction

Tropical cyclone (TC) activity can be envisioned as a measure of the destructive potential of all tropical cyclones in a given basin and in a given year. North-Atlantic hurricane activity, as defined by the power dissipation index (Emanuel, 2007) or the accumulated cyclone energy (Bell et al., 2000), was multiple times smaller during the 1970s and 1980s than in the preceding or following decades. The high hurricane activity we have witnessed in the recent decades (Emanuel, 2005) poses the pressing question of whether the “hurricane drought" of the 1970s and 1980s was natural or anthropogenic in nature. In the former case, we can expect similar “droughts" to occur periodically, providing a respite from hurricane hazards. In the latter case we need to consider the recent hurricane activity as the new normal and prepare accordingly.

Hurricane activity depends on the number of hurricanes during each season, their intensity and their duration. These in turn depend on a variety of proximal environmental causes like variations in mid-tropospheric saturation deficit, vertical wind shear, horizontal vorticity and potential intensity (Emanuel, 1988; Rousseau-Rizzi and Emanuel, 2019). The differences in TC activity between the 1970s-1980s and the two following decades are illustrated in Fig. 5-1. The left panel shows that, during the hurricane drought, there was a smaller number of storms of all categories, with the largest relative differences occurring for major hurricances. The center panel then shows that major hurricances are responsible for almost all of the difference in power dissipation index between the two periods and result in a total power dissipation index that is about twice as large in 1990-2010 than in 1970-1990 (not shown but can be inferred from the figure). The power dissipation index is computed using the IbTRACS dataset (Knapp et al., 2010). Finally, the right panel shows the differences in seasonal cycle between the two periods and outlines that the decrease in TC activity was not confined to only a part of the season.

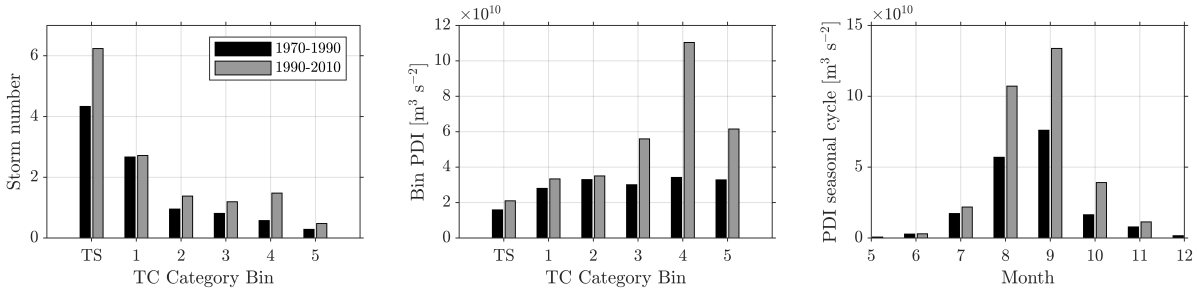

Figure 5-1: Average storm number per year and per category (left), average power dissipation index (PDI) per year and per category (center) and average PDI seasonal cycle (right) for the period from 1970 to 1990 (black bars) and from 1990 to 2010 (gray bars).

Fortunately, to explain the ultimate cause of hurricane activity variability, as defined by the power dissipation index, we mostly need to explain variations in sea-surface temperature anomaly (SST) in the tropical North Atlantic main development region during hurricane season (August-September-October) since both variables are well correlated (Emanuel, 2007; Villarini and Vecchi, 2012). This is illustrated in Fig.5-2 which shows a scatter plot of main development region SST anomaly against power dissipation index, over the 40 years period described above. Over that period, the linear correlation coefficient between SST anomaly and the power dissipation index is $R = 0.75$. When we consider only the low-frequency variability, by filtering out the interannual variability using a 7 years low-pass Lanczos filter we obtain $R = 0.84$, which is very high. The focus on low-frequency variability is appropriate to help explain multidecadal variability like the hurricane drought, and the 7 years cutoff was chosen to filter out El-Nino Southern Oscillation. Considering all years over which we can reasonably trust the power dissipation index estimate, from 1950 to the present day, and without applying any filtering, we still obtain $R = 0.6$, with most of the decrease in correlation occurring in the latest decade (not shown). This is still a surprisingly strong correlation, considering that we have no reason to expect the relation between the power dissipation index and SST to be linear. These analyses warrant the use of main development region SST anomaly as a predictor of Atlantic hurricane activity.

Multiple mechanisms have been proposed to explain past changes in tropical North

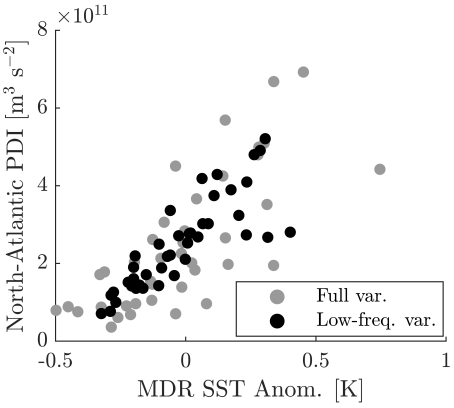

Figure 5-2: Scatter plot of power dissipation index (PDI) against main development region SST anomaly (gray), and 7-year cutoff low-pass filtered PDI against main development region SST anomaly (black).

Atlantic SST anomaly, and hurricane activity. Most prominently, basin-wide natural multidecadal variability, called the Atlantic Multidecadal Oscillation (AMO, Zhang and Delworth, 2006; Zhang et al., 2013), was for a while thought to be an important driver of tropical North Atlantic SST and hurricane activity. On the other hand, the evidence presented in a steadily growing number of papers using both statistical (Mann and Emanuel, 2006), and numerical (Booth et al., 2012; Dunstone et al., 2013; Villarini and Vecchi, 2013) methods suggests an important role of anthropogenic aerosol direct and indirect effects in setting basin-wide SSTs. Further, the North-Atlantic-wide 70-year period spectral peak attributed to the AMO in paleoclimate records and CMIP5 preindustrial simulations was recently shown to result from volcanic aerosol emissions (Mann et al., 2021), and more precisely from a multidecadal periodicity in explosive volcanic eruptions as reported by Ammann and Naveau (2003). Similarly, 20th century multidecadal variability attributed to the AMO was shown not to require an interactive ocean (Clement et al., 2015) but instead to be due to anthropogenic (Murphy et al., 2017; Mann et al., 2020; Si et al., 2020) and volcanic (Birkel et al., 2018) radiative forcing. Throughout this chapter, we will use the acronym AMO to denote a hypothetical mode of natural multidecadal variability. To qualify Atlantic multidecadal variability without implying that it is due to natural causes, we will use the adjective "AMO-like".

Despite the evidence that SST multidecadal variations on the scale of the North-Atlantic do not result from internal variability, climate model simulations focusing more narrowly on the effects of anthropogenic sulfate aerosols in the tropics, and on hurricane activity, fail to capture the full observed variability, missing specifically the magnitude of the multidecadal drought of the 1970s and 1980s (Dunstone et al., 2013; Villarini and Vecchi, 2013). The large statistical dependence of TC activity on the emissions of SO_2 (e.g., Mann and Emanuel, 2006), a sulfate aerosol precursor, along with this relatively small modelled dependence suggests that the effects of anthropogenic sulfates could be amplified locally by positive climate feedbacks that are not well captured in climate models.

In the present chapter we propose such a positive feedback, by which sulfate aerosol forcing can enhance Saharan dust lofting and transport over the tropical North Atlantic. Saharan dust is an environmental factor that was recently shown as key in accounting for the magnitude of the hurricane drought (Strong et al., 2015, 2018) and that is poorly represented in climate models (Evan, 2018). A deeper understanding of the mechanisms controlling dust variability is important for tropical cyclone climate predictions as it will allow us to better constrain near-future TC variability. Thus far, the literature on tropical cyclones has been silent about the causes of dust variation. In this chapter, we will argue that most of the 20th century dust variability cannot be considered to be internal to the climate system, but should be considered a feedback to anthropogenic sulfate forcing that might possibly exceed the direct and indirect effects of sulfates themselves in the tropical North Atlantic main development region. Perturbations to SST in the tropical North Atlantic are also thought to be enhanced by surface wind speed and cloud feedbacks (e.g., Bellomo et al., 2016). This is an interesting hypothesis that relates to the effects of dust (Evan et al., 2011, 2013; Doherty and Evan, 2014) and to which we will return, in future research.

5.1.1 The causes of dust variability: A possible anthropogenic aerosol dust feedback

Sulfates aerosols originating from European SO_2 emissions are swept South by dominant lower tropospheric winds, across the Mediterranean and over North Africa (Lelieveld et al., 2002; Kallos et al., 2007). There, during the peak in precursor emissions and atmospheric concentration of the early 1980s (Mylona, 1996; Preunkert et al., 2001; Smith et al., 2011; Hoesly et al., 2018), the aerosol direct shortwave forcing was about -2.7 W m^{-2} at the top of the atmosphere (Marmer et al., 2007). Afterwards, the sulfates from Europe, along with additional anthropogenic aerosols emitted over North-Africa, are swept West over the tropical Atlantic where they mix with the Saharan dust plume and are scavenged by the eolian dust. Measurements show that this scavenging largely decreases the direct radiative effects of the sulfates over the tropical North Atlantic (Li et al., 1996; Li-Jones and Prospero, 1998) which stands in contrast with the idea that sulfate aerosol direct forcing was the main proximal cause for the tropical North Atlantic SST variability of the 1970s and 1980s.

Outside of the Saharan dust plume, the radiative forcing by sulfate aerosols originating in the northern hemisphere acts to weaken the inter-hemispheric temperature gradient during summer (Zeng, 2003; Held et al., 2005). This causes a reduction of the northward extent of the African monsoon and has been shown by multiple studies to cause or worsen drought conditions in the Sahel (Giannini et al., 2003; Rotstayn and Lohmann, 2002; Biasutti, 2011; Martin et al., 2014; Allen et al., 2015; Ackerley et al., 2011; Xue et al., 2016; Westervelt et al., 2017, 2018; Giannini and Kaplan, 2019). In turn, the dust which covers the Atlantic correlates well with drought conditions in the Sahel (Prospero and Lamb, 2003; Prospero et al., 2014). Rather than the drought itself, the associated large-scale low-level wind changes (e.g., Newell and Kidson, 1984; Grist and Nicholson, 2001; Nicholson, 2009) are thought to be the proximal cause of enhanced emission and transport of dust (Ridley et al., 2013, 2014; Doherty et al., 2014; Wang et al., 2015; Evan et al., 2016), but here, similarly to (Mahowald et al.,

2010), we will use drought as a proxy for windy and dusty conditions. Precipitation has been directly observed for over two centuries in the Sahel (Nicholson et al., 2012) making drought a more reliable proxy for dust than reanalysis wind data for the first part of the 20th century.

The sulfate forcing, Sahelian drought and dust optical depth over the ocean all reach a maximum in the 1970s and 1980s, at the same time as the poorly explained decrease in hurricane activity. The enormous amounts of dust lofted in warm Saharan air get transported over the North-Atlantic all the way to the Caribbeans. This far from the source, dust originating from the Sahara-Sahel (Bozlaker et al., 2018) still has the largest direct radiative effect of any aerosol species present (Prospero and Carlson, 1972; Li et al., 1996), the effect of which on the climate acts to reduce hurricane activity (Dunion and Velden, 2004; Strong et al., 2018). The fact that the mean and variance of dust emissions are vastly underrepresented in climate models, at least up to CMIP5 (Evan et al., 2014; Evan, 2018), might explain why thus far, GCM simulations of hurricane activity failed to capture the observed variability, unless dust optical thickness was prescribed (e.g., Strong et al., 2018). Similarly to anthropogenic aerosols, volcanic stratospheric aerosols have been hypothesized to modulate drought conditions in the Sahel, especially when they are asymmetric about the equator (Haywood et al., 2013). This bolsters the argument that hemispherically asymmetric aerosol forcing is responsible for the enhanced dust concentrations of the 1970s and 1980s.

Hence we suggest that past hurricane activity has been controlled by local dust forcing, the variability of which has been modulated by remote sulfate aerosol forcing. A paleoclimate analogue to this hypothesis can be found in the case of the mid-holocene green Sahara, which was due to orbital forcing changes (e.g., Kutzbach and Liu, 1997) and associated with large dust emissions and transport reductions (Williams et al., 2016), which would have reduced tropical cyclone activity (Pausata et al., 2017).

5.1.2 Objectives

In summary, in this chapter, we propose an indirect mechanism through which sulfate forcing may have further enhanced the hurricane drought; by enhancing dust emissions. To help explain the 1970-1990 TC drought, we first aim to establish a relation between dust cover over the tropical North-Atlantic and sulfates, by relating dust to basin-wide multidecadal SST variability and to Sahel drought conditions, which have been shown to be due to sulfate forcing. Then, we aim to show that dust direct radiative effects can explain a large fraction of the SST anomaly multidecadal variability in the hurricane main development region, and hence is necessary to explain the hurricane drought of the 1970s-1980s. First, section 5.2 exposes the methods used to reach those goals. Then, section 5.3 describes the main results and section 5.4 discusses the interpretation and relevance of the findings. Finally, section 5.5 summarizes and concludes the chapter.

5.2 Methods

Since forced SST response in the Atlantic is thought to have longer time scales than natural variability (Bellomo et al., 2018), we aim to isolate low-frequency variability modes by using the low-frequency component analysis method introduced by (Wills et al., 2018). This method finds linear combinations of the leading empirical orthogonal functions in a dataset, that maximize the ratio of low-frequency to total variance while retaining variance at all frequencies. This method can be thought of as a signal-to-noise maximizing empirical orthogonal functions analysis method (e.g., Ting et al., 2009). The results are low-frequency patterns (LFPs), which are not orthogonal to one-another, and the associated low-frequency components (LFCs), which are uncorrelated. The resulting modes are sorted by the ratio of low-frequency to total variance, so that we expect the first LFC, named LFC1, to have the longest time scale. This method has two input parameter: the low-pass filter cutoff, used to define low-frequency, and the number of leading empirical orthogonal functions used. Here, we set the low-pass filter cutoff at 7 years, to filter out the interannual

variability associated with El-Nino Southern Oscillation while retaining interdecadal variability in the Atlantic, and the number of leading empirical orthogonal functions to 25, based on previous work (Wills et al., 2018, 2019). The results are not very sensitive to the choice of parameters. This method has been shown to capture accurately both forced (global warming) and natural (El-Nino Southern Oscillation) modes of variability, and we apply it here to gain insight into the modes of variability of the tropical North Atlantic SST and to see whether we can isolate the signal of the sulfate aerosols and the dust feedback. We analyse SST data from the the Hadley Centre Global Sea Ice and Sea Surface Temperature (HadISST) dataset (Rayner et al., 2003) from 1870 to the present. The mean seasonal cycle is removed from the data, but the global warming trend is not.

5.2.1 MIT single column model

In order to see if the amplitude of the main development region SST anomaly can be attributed to dust, we run simulations using the MIT single column model (SCM) (Bony and Emanuel, 2001) under a weak temperature gradient (WTG) constraint, with added aerosols. We use the MIT SCM along with the two-spectral-intervals radiation scheme of Fouquart et al. (1980) and Morcrette (1991). The model uses the convection parameterization of Emanuel and Živković-Rothman (1999) to compute the evolution of water vapor. The simulations do not allow for cloud feedbacks on radiation and instead use fixed profiles of cloud fraction to decrease the noisiness of the sensitivity experiments. Despite this simplification, we acknowledge that the feedback of clouds in WTG is an important topic in its own right which may be relevant to main development region SSTs, as suggested by the observational results of Bellomo et al. (2016). The ocean is a 2 m deep slab which allows the system to equilibrate rapidly. Even with slab depths representative of summer mixed layers mixed-layer ($\sim$70 m), WTG-contrained simulations equilibrate within a few months, much faster than radiative convective equilibrium simulations.

To gain insight into the sensitivity of SST, potential intensity and other TC-relevant

quantities like the genesis potential index (Emanuel and Nolan, 2004) to dust optical thickness, we adjust the simulated dust shortwave (SW) asymmetry parameter ($\hat{g}$) and single scattering albedo (ω_0), and the longwave (LW) extinction efficiency of dust to produce similar surface and top-of-atmosphere (TOA) forcing efficiencies as documented by Song et al. (2018). Forcing efficiency is defined as the aerosol direct radiative forcing, normalized by the optical thickness (τ) at 0.55 μm (e.g., Zhou et al., 2005). We take $g = 0.70$ and a single scattering albedo of $\omega_0 = 0.88$ for SW. We retain the assumption of the scheme of Morcrette (1991) that aerosols do not scatter LW and set $\tau_{10\mu m}/\tau_{0.55\mu m} = 0.5$. As will be shown later, these parameters are broadly consistent with dust observations and, more importantly, yield similar dust forcing efficiencies as those derived from observations. As a reference and to test the sensitivity of the results to the dust optical properties, we vary $\hat{g}$ between 0.6 and 0.8 and ω_0 between 0.78 and 0.98, both implausibly low and implausibly high values for dust optical properties. The vertical dust profile is gaussian shaped with a maximum at 700 hPa and a standard deviation of 100 hPa. This is an idealized version of the Saharan air layer dust profile as it moves from West Africa over the ocean (e.g., Kuciauskas et al., 2018). As the dust moves further West the altitude of the layer decreases progressively, which might impact its longwave radiative effects.

5.2.2 Dust proxy

In order to get an estimate of dust optical thickness as a function of time over the main development region during the 20th century, we combine three different datasets. First we convert boundary layer dust concentration measured at Barbados (Prospero, 2015) from 1965 to 2012 to dust optical depth over the main development region by using satellite measurements (Evan and Mukhopadhyay, 2010) of the peak dust period of the early 1980s. The Barbados dataset includes both high-dust and low-dust decades and, along with the satellite measurements, it provides an estimate of the multidecadal dust optical thickness variations over the main development region. Then, to further extend the dust record in time, we make use of the strong correlation between Barbados dust and Sahel rainfall and compute a regression of Barbados dust

on a Sahel precipitation index (mm/month) extending from 1901 to 2017 (Mitchell, 2013). This is a method similar to that employed by Mahowald et al. (2010).

5.3 Results

5.3.1 Dust reconstruction

The top panel of Fig. 5-3 shows the reconstructed aerosol optical depth over the main development region, based on the Barbados dust record (black) and on the Sahel precipitation index (gray). The timeseries are low-pass filtered with a 7 years period to remove the influence of El-Nino Southern Oscillation on precipitation and dust, but the filtering does not change the results qualitatively. The dust at Barbados is rescaled by the aerosol optical depth and seasonally averaged from May to October, and we just take the annual average Sahel precipitation index since almost all of the precipitation in Sahel falls during the summer when dust concentration is high over the tropical North Atlantic main development region. We consider dust cover up to a few months before the start of hurricane season because of the thermal inertia of the ocean mixed layer. The correlation between the low-pass filtered dust and the Sahel precipitation index is $R = -0.85$, which is very strong and consistent with the similarity between the Barbados record and the Sahel precipitation index proxy (without low-pass filtering, the correlation is $R = -0.71$).

The bottom panel of Fig. 5-3 shows the Sahel precipitation index in mm/month (blue) computed over the region [20-10N, 20W-10E], along with a simulated hemispheric asymmetry in sulfate aerosol optical depth of volcanic and anthropogenic origins (black). The aerosol optical depth asymmetry is an ad hoc index for the radiative forcing, computed from GISS-E2-1-G climate model (Bauer et al., 2020; Miller et al., 2021) CMIP6 simulations, over the region from 60 S to 60 N, and 35 W to 55 E, to focus on Africa and Europe. The asymmetry is due in large part to the change in anthropogenic emissions in the northern hemisphere since southern hemisphere emissions are comparatively small in the region considered. The correlation between

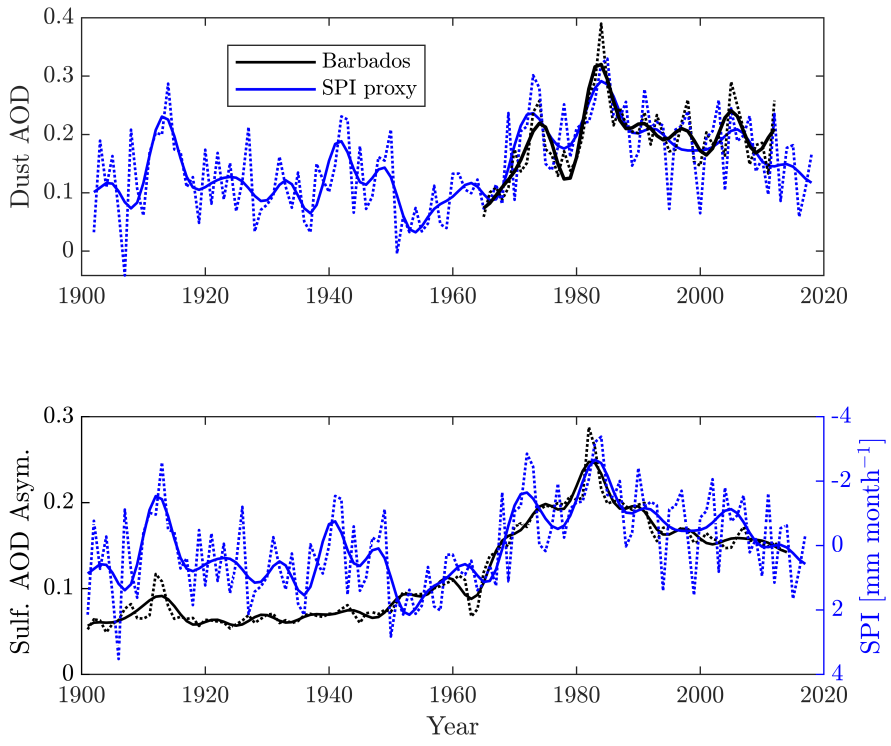

Figure 5-3: Top panel: Barbados summer dust measurements rescaled by satellite measurements of main development region aerosol optical depth (AOD) during the 1980s (black) and main development region AOD reconstruction based on the Sahel precipitation index (SPI) proxy (blue). Dotted lines are not filtered, and solid lines are low-pass filtered. Bottom panel: Low-pass filtered anthropogenic and volcanic sulfate AOD asymmetry (black), and SPI (blue). The y-axis for the precipitation index is reversed so that peaks indicate dry years. Dotted lines are not filtered, and solid lines are low-pass filtered.

this sulfate aerosol asymmetry index and the Sahel precipitation index is $R = -0.76$, supporting the idea that European sulfate emissions enhanced Sahel drought.

The contribution of the volcanoes to the asymmetry index, like that of the anthropogenic emissions, depends on the location of the aerosols. Explosive volcanic eruptions like that of Pinatubo (1991) expel long-lived stratospheric sulfate aerosols causing large radiative forcings, but the eruptions that have the largest influence on Sahel precipitation are not always the strongest, but the most asymmetric (Haywood

et al., 2013). For example, the northern hemisphere radiative forcing associated with the Pinatubo eruption (1991) was larger than that associated with the El Chichon eruption (1982) but it was also much more symmetric about the equator (e.g., Thomason et al., 2018) and isn't associated with a spike in Sahel drought conditions. The strongly asymmetric El Chichon eruption, on the other hand, is associated with the most severe drought on record in the Sahel, and the dustiest year on record in Barbados. One other notable example is the eruption of Novarupta (1912) which was confined to the northern hemisphere and is also associated with a spike in drought conditions early in the record. We also note that while hemispherically symmetric large eruptions like that of Pinatubo might not impact Sahel drought conditions and dust emissions as strongly as asymetric eruptions, the increased planetary albedo will still decrease global precipitation (Trenberth and Dai, 2007) and will affect sea surface temperatures directly (Birkel et al., 2018).

Other factors influencing drought conditions in the Sahel may include global warming (Hill et al., 2017, 2018) and vegetation feedbacks (Yu et al., 2015; Tierney et al., 2017). In addition, a dust feedback on drought was proposed in multiple studies, by which dust optical scattering and absorption influence the precipitation over the Sahara-Sahel (e.g., Miller and Tegen, 1998; Wang et al., 2012; Colarco et al., 2014; Pausata et al., 2016; Jordan et al., 2018). However, the sign of this feedback itself remains unclear due to uncertainty over the optical properties of dust. As evidenced by (Strong et al., 2015), for scattering dust, the feedback is positive and destabilizing, and for absorbing dust, the feedback is negative and stabilizing. Recent research suggests that dust might be more absorptive than previously thought (e.g., Kok et al., 2017; Song et al., 2018) and so here we will consider that if dust acts on Sahel drought in any way, it is as a negative feedback.

5.3.2 Simulations of dust radiative impacts

Figure 5-4 (left panel) shows the sensitivity of SCM simulations to dust aerosol direct radiative effect , under a WTG constraint. The aerosols optical depth (τ) is varied

from from 0 to 0.5 in increments of 0.05. The sensitivity of SST to the optical depth is linear and has a value $\delta SST/\delta\tau$ = -1.4 K τ^{-1}. We note that this sensitivity is very dependent on the choice of dynamical constraint applied to the SCM. Simulations run to radiative-convective equilibrium have a sensitivity to optical thickness almost an order of magnitude larger (not shown), but the WTG constraint is more appropriate to simulating the effects of dust over a limited area of ocean (Rousseau-Rizzi and Emanuel, In review). Comparatively, modifying the single scattering albedo and asymmetry parameter to implausibly low or high values yield sensitivities between $\delta SST/\delta\tau$ = -0.8 K τ^{-1} and $\delta SST/\delta\tau$ = -2.0 K τ^{-1}, which is not all that different from -1.4 K τ^{-1}. Another aspect to consider is that stratocumulus feedbacks in WTG could enhance the sensitivity of SST to dust aerosol optical depth, but this effect is not captured here because we fixed the cloud profiles. The center and right panels show the forcing efficiency of the prescribed aerosols as a function of optical thickness. Black squares denote a surface forcing efficiency and blue squares a TOA efficiency. The horizontal dashed lines are state-of-the-art estimates of dust forcing efficiency computed by Song et al. (2018), based on particle size distributions from the 2011 Fennec aircraft campaign (Ryder et al., 2013a,b), refractive indices from Colarco et al. (2014) in the SW and Biagio et al. (2017) in the LW, and particle shape distributions from Dubovik et al. (2006). At high values of dust concentration ($\tau > 0.3$), the forcing efficiencies produced by the MIT SCM are within 10% of the state-of-the-art estimates of Song et al. (2018). Considering different models for particle size distribution, refractive indices and particle shape distributions, yields a broader range of radiative forcing efficiencies than the ones simulated here (Song et al., 2018). This correspondence is a consequence of setting $g = 0.70$, $\omega_0 = 0.88$ and $\tau_{10\mu m}/\tau_{0.5\mu m} = 0.5$ purposely to reproduce the observed forcing efficiency (all parameter values are reasonable).

Since we are confident that our simulated forcing efficiency is reasonable, we turn our attention to the sensitivity of TC activity-relevant physical parameters to dust aerosol optical depth . Figure 5-5 (left panel), shows equilibrium potential intensity

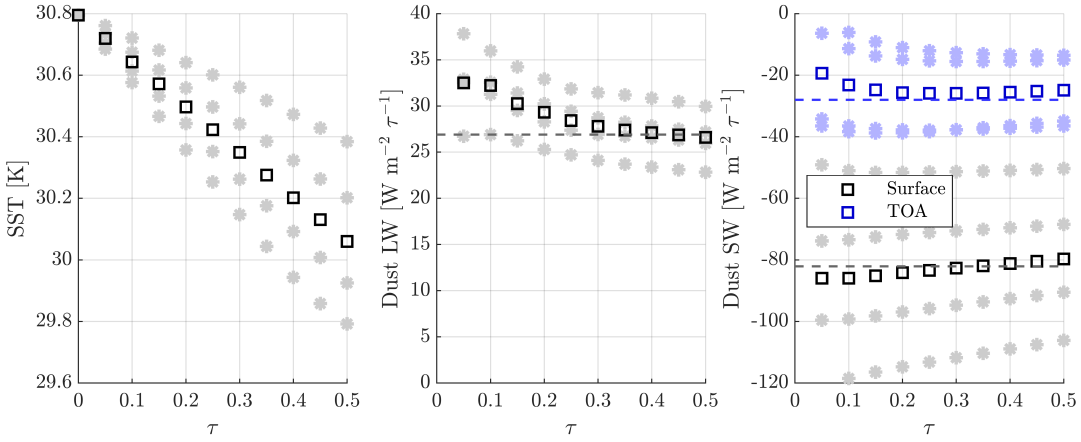

Figure 5-4: Left: simulated SST as a function of dust optical thickness (τ) at 0.55μm. Center: Simulated dust longwave surface forcing (black squares), and estimate from Song et al. (2018) (dashed black line). Right: Simulated dust shortwave surface forcing (black squares), and estimate from Song et al. (2018) (dashed black line), and dust shortwave TOA forcing (blue squares), and estimate from Song et al. (2018) (dashed blue line). The faded profiles represent the simulations with $\hat{g}$ between 0.6 and 0.8 and ω_0 between 0.78 and 0.98.

(PI) as a function of aerosol optical depth . Over the range of aerosol optical depth used in these simulations, potential intensity varies by about 6 m s^{-1}, very linearly. Over the range of aerosol optical depth values occurring on multidecadal time scales over the main development region, potential intensity varies by about 3 m s^{-1}. The potential intensity sensitivity to SST under a WTG constraint corresponds well to values reported in the literature (e.g. Rousseau-Rizzi and Emanuel, In review), with $\delta PI/\delta SST \approx 8.6$ m s^{-1} K^{-1}. The center panel of Fig.5-5 shows saturation deficit (χ), defined as

$$\chi = \frac{s_m^* - s_m}{s_0^* - s_m^*} \tag{5.1}$$

where s is entropy, $*$ denotes saturation, 0 denotes the surface and m denotes the mid-troposphere at 600 hPa. χ is a component of the genesis potential index and is an indication of the dryness of the mid-troposphere. The increase in χ indicates that the aerosols lead to large-scale descent and drying. Finally, the right panel of Fig.5-5 shows the thermodynamic component of the genesis potential index of Emanuel and

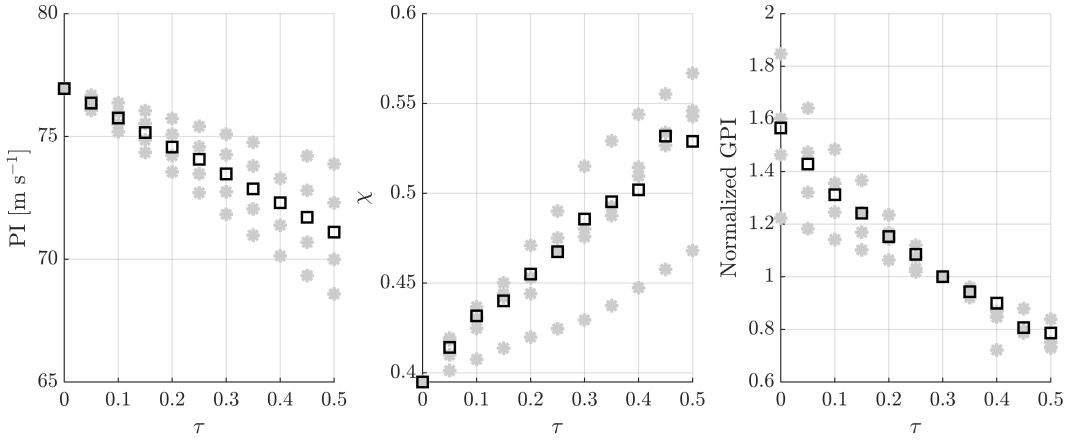

Figure 5-5: Simulated potential intensity (PI, left), saturation deficit (χ, center) and normalized thermodynamic component of the genesis potential index (GPI_T, right) as a function of dust optical thickness (τ) at $0.55\mu m$. The faded profiles represent the simulations with $\hat{g}$ between 0.6 and 0.8 and ω_0 between 0.78 and 0.98.

Nolan (2004) defined as

$$GPI_T = \chi^{-4/3}(PI - 35)^2, \tag{5.2}$$

with GPI_T being normalized by its "high dust" value at $\tau = 0.3$. This shows that, suppressing dust entirely from an ocean basin where $\tau = 0.3$ would lead to an increase in GPI_T of about 55% if all dynamical parameters stay identical. Since the Saharan air layer that carries dust is generally associated with a high shear environment (Dunion and Velden, 2004), it is likely that the increase in GPI_T would be larger. We note that while this is a large relative difference, the statistical linear sensitivity of PDI to SST anomaly is such that PDI drops by about a factor 5 over less than a degree difference. This is larger than can be expected from thermodynamics alone, and points to the likely contribution of changes in vertical shear that correlate with the changes in SST (E.g., Dunstone et al., 2013).

5.3.3 Global pattern

Figure 5-6 shows the two first low-frequency components (LFCs) and low-frequency patterns (LFPs) because they have the highest low-frequency to total variance ratios

and jointly represent most of the low-frequency variability, along with LFPC6 and LFP6 which are important in the main development region. We first look at LFC1 and LFP1 and notice that they look very similar to global warming signals. This isn't surprising since (Wills et al., 2018, 2019) reported a similar result and we used the same method. To verify that the first component captures all of the global warming signal, we compute correlations between the first 10 LFCs and the tropical mean SST. The tropical mean SST is computed using the same data set, and filtered using the same 7-year low-pass threshold. The top panel of Fig. 5-7 shows that indeed, the correlation between tropical mean SST and LFC1 is very high ($R = 0.98$), even if the low-frequency component analysis is restricted to the Atlantic Ocean, which is a fairly small part of the global oceans. The correlations between the next 9 modes and tropical mean SST are very small, which is expected given that the modes are uncorrelated. Correlations between LFCs and the global mean ocean temperature are very similar (not shown). This indicates that none of the other modes of variability are representative of global changes.

Clearly identifying the global warming signal gives us confidence that this method can precisely identify forced signals that are distinct from natural variability. In addition, the variations of SST associated with this global mode and averaged over the main development region have a regression coefficient with the tropical mean SST of 0.97. This means that for every degree the tropics warm, the main development region warms by very nearly a degree in this pattern. This is a very useful result because it allow us to treat all the other patterns as local anomalies with respect to the tropical average. It has been shown that potential intensity, and thus the genesis potential index, is much more sensitive to local SST changes than to global ones, so long as the global changes are not due to near surface wind speed changes (e.g., Vecchi and Soden, 2007; Ramsay and Sobel, 2011; Emanuel and Sobel, 2013; Rousseau-Rizzi and Emanuel, In review). In addition, potential intensity varies very linearly with SST perturbations in the tropics, with a slope of about 9 m s^{-1} K^{-1}. This means that in LFC1, changes in SST are not associated with large changes in potential intensity or TC activity in the tropics and that, in any mode other than LFC1, a 1 K variation

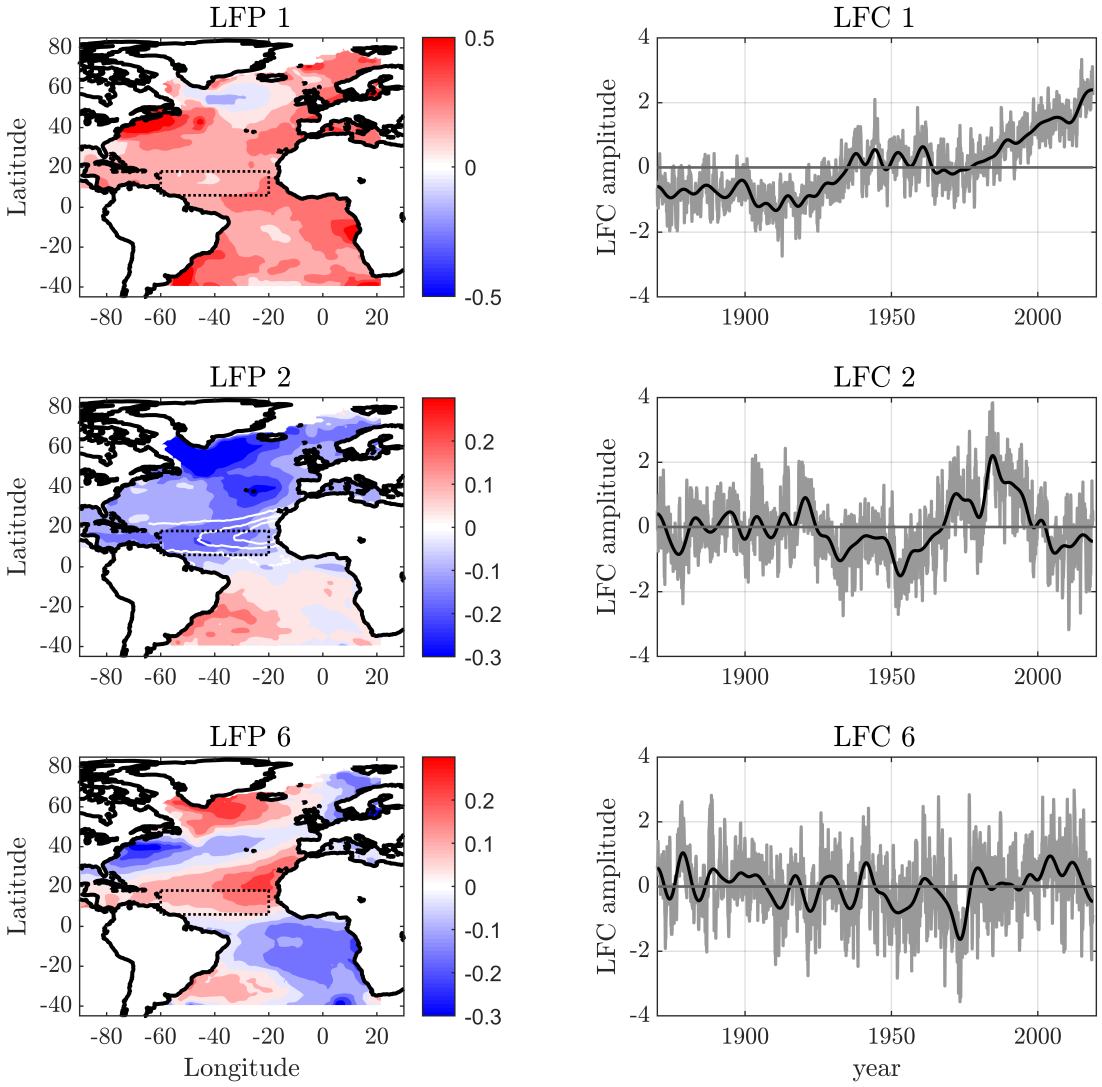

Figure 5-6: Left: first (top), second (middle) and sixth (bottom) low-frequency patterns (LFPs) of temperature (color shading) with main development region identified (dotted black box). LFP2 is plotted along with dust aerosol optical depth contours from (Evan and Mukhopadhyay, 2010) for $\tau = [0.150.30.45]$ (white contours). Right: corresponding low-frequency components (LFCs) including variability at all frequencies (gray) and only at low frequencies (black).

of SST over the main development region will correspond fairly precisely to a 9 m s^{-1} variation of potential intensity.

5.3.4 Local patterns

TC activity being more sensitive to local changes than global ones means that, over a timescale of a few decades, the first low-frequency component, LFC1 is unimportant for hurricane activity relative to several higher order modes (e.g., Rousseau-Rizzi and Emanuel, In review). Hence we next look at the remaining LFCs to explain the variance in potential intensity and in TC activity. To do so, we look for the patterns associated with the largest main development region SST anomaly. Figure 5-8 (top panel) shows the square root of the low-frequency main development region SST variance associated with each low-frequency component analysis mode. Apart from LFC1, which we argued not to be as important an influence on potential intensity as some of the other modes, the component with the highest low-frequency variance in the main development region is LFC2. The index "2" means that the associated low-frequency variance is the second largest over the whole of the Atlantic basin. Figure 5-6 shows the second low-frequency pattern LFP2 along with LFC2, which closely resemble the pattern and time series of the AMO as defined by Trenberth and Shea (2006). This is not surprising considering that our LFC1 correlates very well with global temperatures, and that the AMO of Trenberth and Shea (2006) is defined with respect to the global mean temperature, and not with respect to a linear trend, as defined for example in Murphy et al. (2017). In the NH, LFP2 exhibits a large variability in a horseshoe pattern starting from a maximum in the region of the subpolar gyre and decreasing progressively until the tropical North Atlantic. The amplitude of the pattern in the SH is much smaller and almost uniformly of opposite sign to the NH. Finally, Fig.5-6 also shows LFP6 and LFC6, which explain the most SST variability in the main development region after LFC2. This component only has the sixth highest low-frequency to total variance ratio because it has comparatively less variability in the subpolar regions than other components, but still explains a substantial part of the SST variance in the main development region. Interestingly,

multidecadal time scales are much less important in LFC6 than in LFC2, with time scales of 10 to 15 years being much more prominent. Since the timescale of LFC6 is not much larger than the low-pass filter cutoff, it is possible that the signal is somewhat damped.

Since we are mostly interested in the 1970s and 1980s, we look at the pattern responsible for the main development region SST anomaly during that period by averaging the product of the LFPs and the LFCs over the main development region and from 1970 to 1990. As can be seen in Fig. 5-8 (bottom), LFP2×LFC2 is responsible for the vast majority of the main development region SST anomaly during that period. Its contribution is multiple times larger than that of any other component when averaged over those two decades. Note that LFC1 is still plotted for comparison, but it reflects a global change, not an anomaly.

5.4 Discussion

5.4.1 Natural vs forced variability

The low-frequency component analysis method is objective and, in itself, tells us nothing about the physical origin of the components, which must be deduced independently. For example, we have established a posteriori that the first low-frequency component, LFC1 is the global warming signal. Similarly, LFC2 is an AMO-like signal, which we will interpret in light of the recent literature on the topic. Notably, (Murphy et al., 2017; Birkel et al., 2018; Mann et al., 2020) show that the ultimate cause of the multidecadal component of the Atlantic ocean SST variability is sulfate aerosol loading, from volcanic and anthropogenic origins. In addition, a LFC forced by asymmetric sulfate loading and dust feedbacks should have a large interhemispheric temperature contrast. This is coherent with the second low-frequency

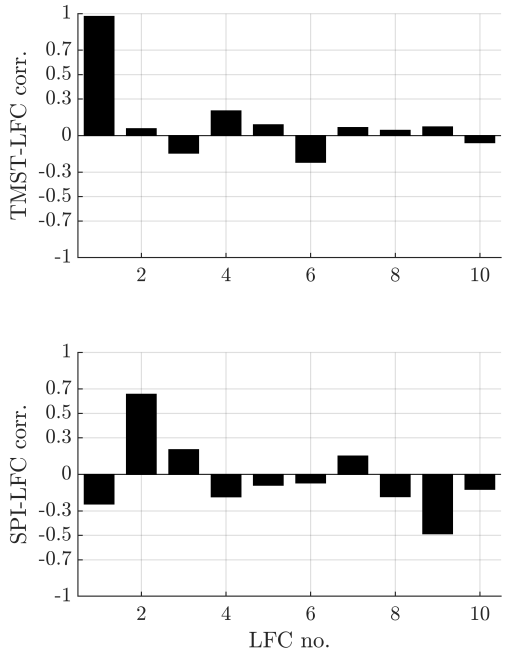

Figure 5-7: Top: correlation coefficient between the tropical mean SST (TMST) and each of the 10 first low-frequency components (LFCs). Bottom: correlation coefficient between the Sahel precipitation index (SPI), and each of the 10 first LFCs.

pattern, LFP2, which has the largest interhemispheric temperature contrast of all 25 LFPs, by about a factor 3. The relative contribution of LFP2 to the total interhemispheric temperature contrast was even more important during 1970-1990 (not shown). Further, a LFC associated with sulfate emissions should correlate well with Sahel precipitation. Figure 5-7 shows the correlation of the 10 first LFCs with a Sahel precipitation index (Joint Institute for the Study of the Atmosphere and Ocean, doi:10.6069/H5MW2F2Q) based on the dataset of (Becker et al., 2013). None of the LFCs correlate well with the Sahel precipitation index, except for LFC2 which has a correlation coefficient $R = 0.69$. Such a correlation coefficient is surprisingly large considering that the Sahel precipitation index timeseries extends back to 1900. Interestingly, correlating the whole summer main development region anomaly or the North-Atlantic SST index (NASSTI) with Sahel precipitation yields considerably smaller correlations ($R = 0.40$ and $R = 0.30$ respectively). This suggests a relation between LFC2 and Sahel precipitation, or a common driver, and strenghtens the argument that this AMO-like mode is associated with dust emissions. Finally, we will also add that the low-frequency variance of LFC2 during the first half of the record, from 1870 to 1950 is about half that during the period from 1950 to 2018, which is coherent with the results of (Si et al., 2020) and is expected from anthropogenic aerosol loading increasing in the second half of the 20th century.

5.4.2 The estimated effect of Sulfate-forced dust loading on SST

We will now compare the three independent analyses we performed. First, we rescaled summer dust measured at Barbados by measured aerosol optical depth over the main development region during the dusty period of the early 1980s. Based on the strong correlation between Sahel drought conditions and dust measurements at Barbados, we then used the Sahel precipitation index as a proxy to establish an es-

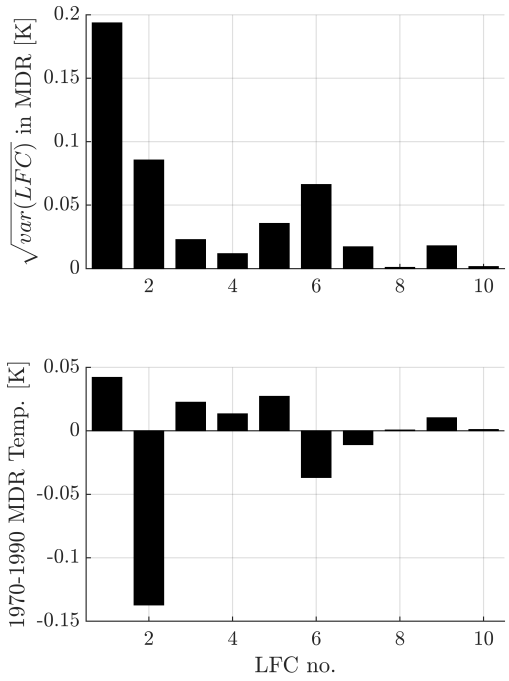

Figure 5-8: Top: Square root of the variance of SST in the main development region (MDR) for the 10 first low-frequency components (LFCs). Bottom: contribution of each of the 10 first LFCs to the main development region SST anomaly during the 1970s-1980s.

timate of aerosol optical depth variations over the last century (shown in Fig.5-3). Second, we tested the sensitivity of a SCM under a WTG constraint to dust loading. The dust optical properties were chosen to ensure that the dust radiative efficiency was similar to that obtained by state-of-the-art measurements and radiative transfer models. From these simulations, we obtained $(\delta SST/\delta\tau)_{SCM}$ = -1.4 K τ^{-1}. Third, we applied the low-frequency component analysis method to the HadISST dataset and obtained an AMO-like component consistent with a sulfate forcing and associated with Sahel drought (second low-frequency component).

It follows that this pattern must also be associated with dust variations above the main development region. To verify this, we regress the main development region-averaged SST variations associated with the second low-frequency component, LFC2, onto our century dust estimate over the main development region, and obtain a regression coefficient $(\delta SST/\delta\tau)_{reg} = -1.3 \pm 0.3$ K τ^{-1}, which is indistinguishable from that obtained using SCM simulations. We note that the SCM SST sensitivity to dust is only valid for a WTG-constrained system. Similar simulations without the WTG constraint, in which the system reaches radiative-convective equilibrium, yield an SST sensitivity that is an order-of-magnitude too large, suggesting that the WTG constraint is appropriate for the main development region, as shown by (Rousseau-Rizzi and Emanuel, In review).

This is a central result because it indicates that the SST variations associated with the AMO-like pattern are consistent with those expected from the estimated concurrent dust loading. Based on the fact that the AMO-like variability and the associated drought are likely caused by sulfate forcing (e.g., Mann et al., 2021; Biasutti, 2011), *we propose that the dominant effect of the sulfate aerosol emissions on the main development region SST is via their effect on dust lofting and transport.* This is also coherent with a somewhat reduced effect of anthropogenic sulfate aerosols over the main development region, due to scavenging by Saharan dust (Li-Jones and Prospero, 1998). Volcanic aerosols cannot be scavenged by dust due to the altitude difference.

Hence, the second low-frequency pattern, LFP2, is seen here as resulting from anthropogenic and volcanic sulfate forcing outside of the Saharan dust plume, and mostly from the dust feedback in the main development region. We note that, while our estimate of dust effects is sufficient to explain the LFC2 SST variations in the main development region, that estimate itself is uncertain. The effects of dust may include cloud feedbacks as well, as they have been invoked as a tropical North-Atlantic feedback (Evan et al., 2016; Bellomo et al., 2016). This cloud feedback may occur in response to changes in the boundary layer energy balance or to dust acting as condensation nuclei (e.g., Twohy et al., 2009). The tropical North-Atlantic pattern can also be likenened to the Atlantic Meridional Mode, an SST mode of variability that is proposed to be forced by dust (Evan et al., 2011).

5.4.3 Contribution of different modes of SST variability to hurricane activity

So far we have seen that the low-frequency component analysis method identifies the global warning pattern and an AMO-like pattern which we hypothesize to be due to sulfate forcing and dust feedbacks. To evaluate the contribution of those first two modes to total hurricane-season SSTs, we average the SST associated with each mode over the main development region and over the August-September-October period for each year. Then, the resulting yearly hurricane-season global warning and AMO-like SST signals are removed from the total hurricane season main development region SST. The remaining time series only has significant spectral peaks at $\sim$15 years periods or less. This remainder includes mostly higher-frequency modes like LFC6 and is hypothesized to be due to natural variability. Both the removed components and the remaining timeseries retain variance up to the $1/2$ yr^{-1} Nyquist frequency.

The results are illustrated in Fig.5-9, which shows the power spectral density for the sum of all low-frequency components (LFCs) but LFC1 (top panel) and the power

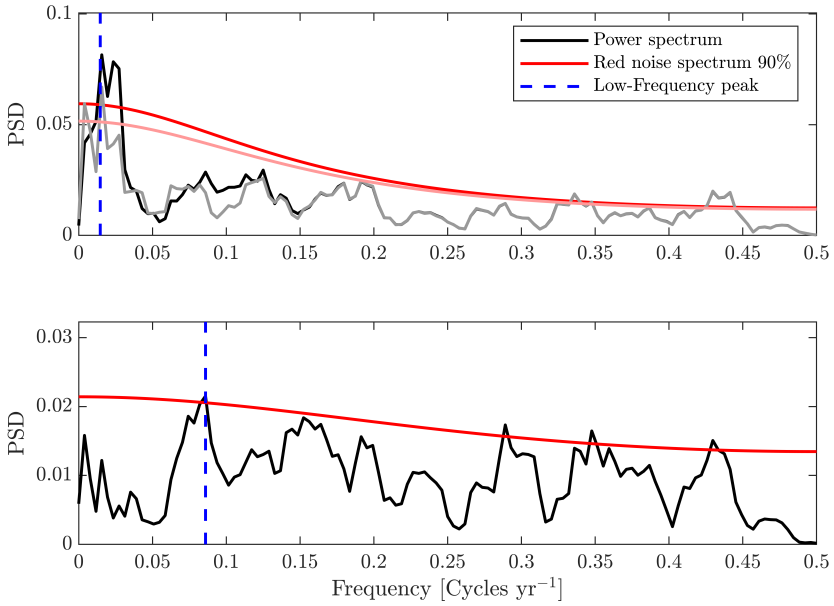

Figure 5-9: Top: Multitaper power spectral density estimate for yearly summer-averaged temperature for main development region SST minus the first low-frequency component (LFC1,black) with 90% confidence red noise spectrum (red) and lowest frequency spectral peak (dashed blue). Multitaper power spectral density estimate for yearly summer-averaged temperature for main development region SST minus LFC1 and estimated dust impact on SST (gray) with 90% confidence red noise spectrum (pink). Bottom: Multitaper power spectral density estimate for yearly summer-averaged temperature for main development region SST minus LFC1 and LFC2.

spectral density of all LFCs but LFC1 and LFC2 (bottom panel). In the first case, only the global warming signal has been removed, and we can see that the lowest-frequency peak is located around a period of 68 years, which is consistent with the literature on AMO-like variability. In the second case, the AMO-like LFC2 is removed as well, and the lowest-frequency significant peak is now found around a period of 12 years. Note that the power spectrum does not go to zero at periods of less than 7-year because we retained variance up to the Nyquist frequencies.

Since past sulfate forcing varied mostly on multidecadal timescales, the lack of a multidecadal peak when the AMO-like mode is removed reinforces the idea that the effects of the sulfate forcing that do not correlate with the global mean temperature are captured by the AMO-like mode. In addition, since Bellomo et al. (2018) showed

that Atlantic ocean SST variability at periods of less than 25 years did not differ significantly between historical and preindustrial simulations using the Community Earth System Model Large Ensemble, we will consider that all LFCs excluding LFC1 and LFC2 result from internal variability. We will not attempt to find a cause for these remaining LFCs but we will also point out that the shape of LFP6 is very similar to the climatological average wind speeds over the Atlantic, and that surface wind speed changes could explain the ∼10-15 years main development region SST variability. We will also point out that some of the significant 3-to 4-year peaks on the bottom of Fig.5-9 may be due to El-Nino Southern Oscillation.

Assuming that the peak around 68 years is due to African mineral dust mediated by anthropogenic and volcanic sulfate forcings, and the associated climate feedbacks, we then try to estimate the contribution of the dust forcing to the multidecadal component of the variance. To do so, we utilize Parceval's theorem and we evaluate the percentage of variance (P_v) that is associated with periods between 30 and 100 years. 30 years was loosely chosen as an upper frequency bound to define multidecadal variability. In effect, we compute a multidecadal-to-total variance ratio given by

$$P_v = \Big[\int_{f_l}^{f_h} PSD\, df \Big/ \int_{f_0}^{f_{nyq}} PSD\, df \Big] \times 100\%, \tag{5.3}$$

where $f_l = 1/100$ year^{-1}, $f_h = 1/30$ year^{-1}, f_0 is the lowest frequency that can be captured by the timeseries and f_{nyq} is the Nyquist frequency. When we consider main development region SST minus LFC1, we get $P_v = 17\%$, and the remainder of the variance is due to higher frequencies. If we then remove LFC2 and consider main development region SST minus LFC1 and LFC2, we get $P_v = 2\%$, which illustrates that, apart from from the global warming signal, the vast majority of the multidecadal variability associated with main development region SST is due to LFC2. This leads to the question of how much of the multidecadal variability is explained by dust forcing only. To answer that question, we evaluate P_v for all LFCs minus LFC1 and an

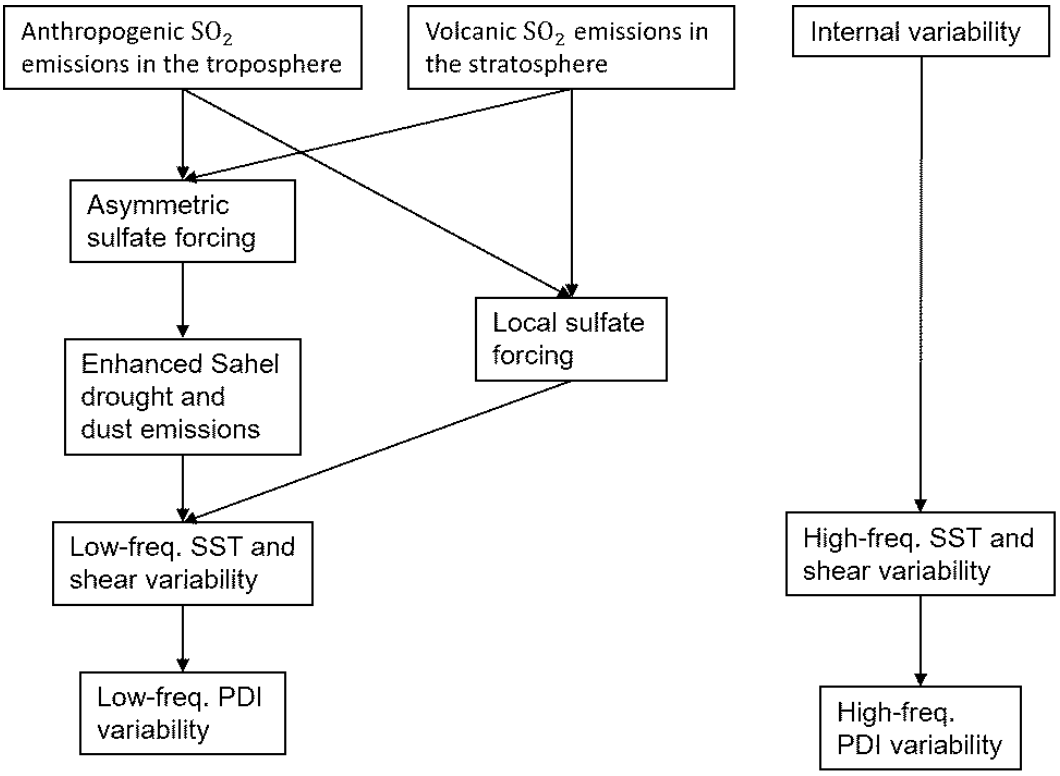

Figure 5-10: Causal diagram of the proposed mechanism

estimate of the direct effects of dust. This estimate is obtained by multiplying the dust Sahel precipitation index proxy by the SCM-derived coefficient $(\delta SST/\delta\tau)_{SCM}$ = 1.4 K τ^{-1}. The resulting power spectrum is shown in gray in the top panel of Fig.5-9. For that spectrum, We get P_v = 12%, which shows that subtracting the direct effects of dust decreases the multidecadal-to-total variance ratio by about 40%, compared to the case where dust is not subtracted. We surmise that the remainder of multidecadal variability is associated with the sulfate radiative forcing itself, and possibly to cloud feedbacks.

To sum up, Fig.5-10, presents the causal diagram of the proposed mechanism. It outlines the most important assumptions we made, such as separate roles for internal and forced variability, which are hypothesized to cause respectively low-frequency and high-frequency activity variations. In addition, it incorporates the novel proposed dust feedback.

We have also discussed that the signal associated with tropical warming, since it occurs at the same rate as main development region warming, cannot explain the observed magnitude of power dissipation index variations. For that reason, it is not included in the causal diagram. However, global warming can cause storms of similar intensity to produce more intense rainfall, which increases their destructiveness, even though it might not affect the power dissipation index (Knutson et al., 2010). In addition, midlatitude warming could allow category 1 and 2 hurricanes to travel further poleward, strongly impacting ill-prepared communities (e.g., Kossin et al., 2014). Since power dissipation index is dominated by major hurricanes, a poleward shift of weak hurricanes will not be captured by power dissipation index estimates, and is unlikely to depend much on main development region SST anomaly. In addition, since the power dissipation index correlates better with the full main development region SST anomaly than with any LFC alone (not shown), the higher frequency natural variability LFCs influencing SST must be considered as influencing power dissipation index, albeit on shorter time scales than the LFC2 AMO-like mode. Finally, on centennial timescale, it is likely that the global mode will become important for TC activity.

5.5 Conclusion

In this chapter, we introduced the idea that Saharan dust radiative forcing varies in response to sulfate aerosol hemispherically asymmetric forcing. This idea is supported by the fact that Saharan dust is known to covary with drought conditions in the Sahel, and that sulfate forcing from Europe in the 1970s-1980s contributed to Sahel drought in the second half of the 20th century. Such a feedback explains why models, most of which do not capture dust variability, struggle to capture the full variability of SST and hurricane activity in the North-Atlantic.

First, using a low-frequency component analysis method, we obtained objective com-

ponents of SST variability. The first component corresponds to global warming and can, within a few assumptions, mostly be ignored for the purpose of studying activity metrics like power dissipation index on multidecadal timescales. The remaining components correspond to SST anomalies, and the most important of these is an AMO-like mode which is associated with almost all of the SST variance in the main development region, on time scales longer than 30 years. The AMO-like mode correlates with drought conditions, and hence with eolian dust over the ocean, back to the early 1900. Since different low-frequency components are uncorrelated, the main development region anomaly associated with this mode must include the contribution of dust and of sulfate aerosols. Then, using SCM simulations, we show that the direct radiative effect of dust in a WTG-constrained system could explain about 40% of the multidecadal SST anomalies in the main development region during summer.

Since those SST anomalies are associated with significant changes in potential intensity and the genesis potential index, the evidence presented herein strongly suggests that the Atlantic hurricane drought of the 1970s and 1980s was caused by anthropogenic sulfur emissions mediated through Saharan drought and African mineral dust. Our results leave little room for a multidecadal natural oscillation of the system, but outline a potentially important role of natural, quasi-decadal variability. These results are consistent with the most recent research on the Atlantic basin multidecadal variability.

Chapter 6

Conclusion

6.1 Summary

This thesis is meant to advance my understanding of tropical cyclones on two different fronts, and to contribute to the scientific knowledge on the topic. To do so, I first studied tropical cyclone thermodynamics with the goal of advancing fundamental tropical meteorology. Then, I transferred that knowledge to the study of tropical cyclone activity climate variability with the goal of addressing a pressing societal problem.

In chapter 2, "An Evaluation of Hurricane Superintensity in Axisymmetric Numerical Models", my coauthor and I worked towards reconciling idealized numerical simulations of tropical cyclones with potential intensity theories. To do so, we compared potential intensity bounds on gradient wind, azimuthal wind, and the magnitude of the surface winds to the corresponding simulated values in axisymmetric simulations with various parameterized mixing lengths. As parameterized mixing decreases, simulated intensities increase, approaching the corresponding PI bound. In some cases, the PI bound is exceeded by up to 5% which is small and may be due to differences between the representation of thermodynamic disequilibrium in PI theories and in the numerical models. In general, **PI is found to be an appropriate bound on TC intensity in idealized simulations**. This result is important because it reaf-

firms that PI can be useful in predicting how strong a TC can become in a given environment. In addition, having a set of idealized simulations which are coherent with theory allows to quantify how the representation of more realistic processes in those simulations can make the simulated intensity depart from theory.

In chapter 3, "A Thermodynamic Perspective on Steady-State Tropical Cyclones", we attempted to clarify the meaning of "steady state" in tropical cyclone simulations and theories by establishing two categories of definitions frequently used in the literature: core steady-state and equilibrium steady-state. Core steady-state (CS) is usually reached early, in a tropical cyclone life, as its intensity peaks, and applies to situations where balance in the inner core of the storm is required, but the environment can still evolve slowly. Equilibrium steady-state (ES) is reached after a decay occuring over tens of days and requires the tropical cyclone environment far from the core to have reached equilibrium with the core. **The difference between ES and CS was found to be mostly due to the drying of the environment in the subsidence region, which caused low-entropy air to mix with the boudary layer inflow of the storm.** Moistening the subsidence region or simulating a completely dry tropical cyclone removes the intensity difference between CS and ES. This contradicts the previous hypothesis presented in the literature (e.g., Smith et al., 2014), that simulated tropical cyclones decay because they run out of angular momentum, and instead suggests that the decrease in angular momentum in the inner core, as the tropical cyclone decays, is due to the system not producing enough work to draw high angular momentum air inwards. These findings are useful because they categorize which theories should be compared to which stages in the life-cycle of the storm. Most potential intensity theories can be compared to the CS period, while most theories for the TC structure far from the core of the storm need to be compared to the ES period.

In Chapter 4, "A Weak Temperature Gradient Framework to Quantify the Causes of Potential Intensity Variability in the Tropics", we tried to understand why PI varies

in nature. To do so, we developed a linear model for PI, based on two predictors: the local SST, which is well observed and studied, and the tropical average midlevel saturation MSE. The linear model partitions PI into two components, which correspond to global and local environmental changes respectively. The first one is consistent with a tropical atmosphere-ocean system in RCE and the second one represents a departure from that RCE state. Model coefficients are obtained from single-column model simulations sensitivity experiments in RCE and under a WTG constraint. The linear model captures between 80% and 96% of the PI variance, depending on the ocean basin. **Further, it shows that, during the last four decades, in the tropical Atlantic, global changes have accounted for only about 10% of the PI variability, the rest being due to local changes.** These results explain why local SST anomalies are such a good predictor of PI, and by extension, of tropical cyclone activity. The fact that PI is shown to vary very linearly with SST and midlevel saturation MSE means that we can evaluate the contribution of different environmental mechanism to the total PI change, via their contribution to the SST change.

Finally, in chapter 5 entitled "Natural and Forced Contributions to the Hurricane Drought of the 1970s-1980s", we utilized the relation between local SST anomalies and hurricane activity to investigate the causes of a large and poorly explained decrease in Atlantic hurricane activity during the 1970s and 1980s. Using objective component analysis we show that the most important mode of SST anomaly variability is an AMO-like mode which includes almost all of the SST variability at multidecadal timescales. This mode of variability correlates well with drought conditions in the Sahel, and hence with dust cover over the North-Atlantic main development region. **In that region, we estimate that dust direct radiative effects during summer can explain up about** 40% **of the multidecadal SST variability.** Since both multidecadal SST variability and the drought in the Sahel have been shown in the literature to be due to sulfate forcing, we propose that the dust variability and its effects on SST are in fact a feedback to anthropogenic forcing. The circumstantial

evidence tying dust variability back to anthropogenic forcing has important implications because, since the sulfate forcing responsible for dust variations peaked due to pollution and declined due to clean air regulations, it means that the hurricane drought of the 1970s and 1980s was a one-time event, not a recurring natural oscillation. In other words, we should expect TC activity to remain high in the upcoming decades, and not decrease back again.

6.2 Future work

Nearing the end of this thesis, we recall that it is but a very small step on the path to understanding tropical cyclones and our climate in general. It provided a few answers but many questions which, although less visible than answers, are as valuable a part of the scientific progress. To close this thesis, we introduce a few questions that arise from the results of chapters 3, 4 and 5, along with ideas on how to answer them.

6.2.1 Follow-up to chapter 3

In this chapter, we have shown that a subsidence-induced decrease in simulated tropical cyclone environmental moisture leads to a decrease in tropical cyclone peak intensity, and to a long intensity decay afterwards. This result raises the question of how much environmental moisture fluxes, or equivalently transient moisture decrease, contribute to the energy budget of real tropical cyclones. In general, studies of tropical cyclone thermodynamic cycles use a differential form of the first law of thermodynamics applied during the period of peak intensity to identify the sources of energy of the cycle or compute its efficiency (e.g., Pauluis and Zhang, 2017). The integration of a differential form of the first law along the secondary circulation assumes steady-state. Hence, its application to the period of peak intensity, where we have shown the thermodynamic cycle not to be in steady-state, obscures the contribution of transient effects like environmental moisture decreases to the thermodynamic cycle. Here we propose using a general form of the first law to evaluate how much of the enthalpy exported by the system originates in the environment versus the ocean surface.

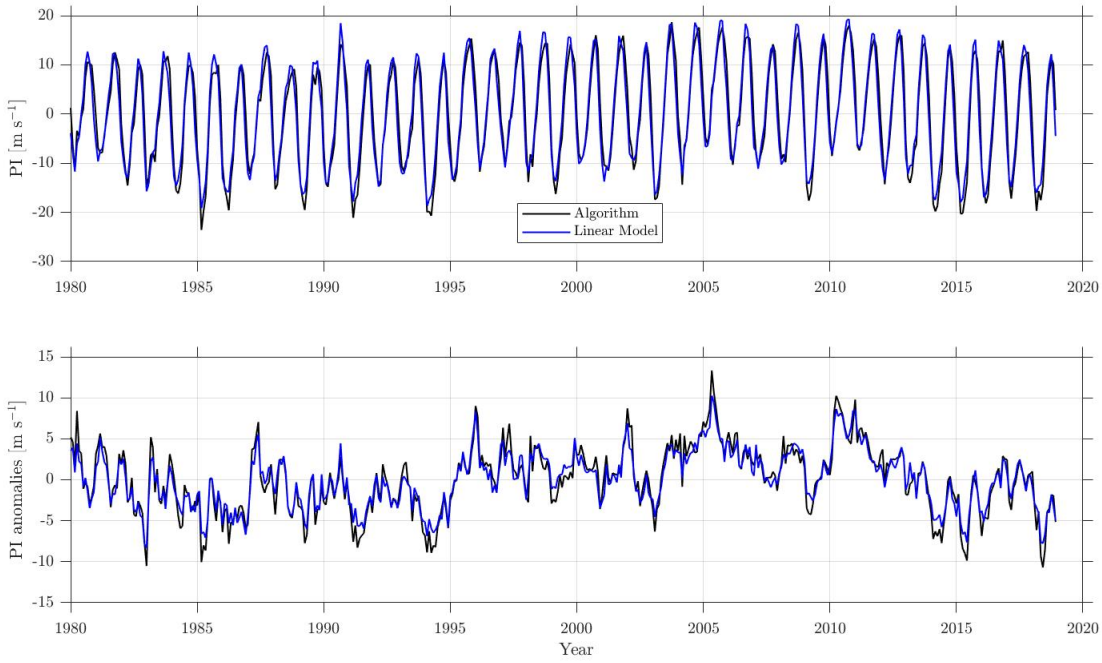

Figure 6-1: Top panel: North-Atlantic PI monthly values computed using a nonlinear algorithm (black) and with the newly introduced linear model (blue). Bottom panel: North-Atlantic PI anomalies with respect to the seasonal cycle, computed using a nonlinear algorithm (black) and with the newly introduced linear model (blue).

6.2.2 Follow-up to chapter 4

In this chapter we have shown that interannual PI variations can be captured by a linear model that depends only on SST and mid-tropospheric saturation MSE variations. As shown in Fig.6-1 the linear model happens to also capture well the PI seasonal cycle, and anomalies with respect to the seasonal cycle, especially in the Atlantic. This means that the effects of midlevel entropy changes on PI can be captured even at monthly time scales. Since the mechanisms controlling the thermodynamic effects of ENSO on tropical cyclones are still poorly understood, we suggest using this framework to try to understand how the tropical atmosphere stabilization brought about by ENSO can impact potential intensity.

To illustrate this concept, on Fig. we show a preliminary composite of the effect of the three strongest El-Nino events captured by the ERA5 record, on the Atlantic PI. As we can see, as the global contribution to SST increases, due to a midlevel increase

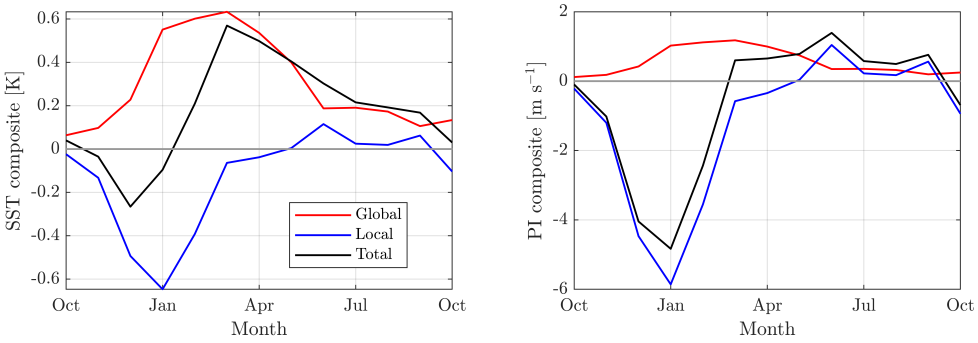

Figure 6-2: Left: Right:

in entropy, the local SST anomaly component becomes negative. Starting in January, as the increase of the global component slows down, the local component of SST starts increasing again towards zero, possibly due to reduced turbulent surface fluxes. Eventually, after the month of April, the Atlantic SST has more or less equilibrated with the large scale and the local anomaly is near zero. From the PI perspective, what this means is that immediately after a sharp increase in the strength of an El-Nino event, PI drops abruptly (~ 5 m s^{-1} here). However, as time goes on and the surface temperature adjusts to the midlevel change, PI reincreases and the PI perturbation even exceeds zero. All three El-Nino events composited here peaked in March and do not have much relevance for TC season. However, this preliminary result suggests that PI changes associated with midlevel perturbations in the Atlantic are only very transiently a function of the magnitude of the perturbation.

6.2.3 Follow-up to chapter 5

In chapter 5, we have sought to relate anthropogenic sulfate aerosol radiative forcing to the hurricane drought of the 1970s-1980s. To refine our nascent understanding of the relation between sulfate aerosol forcing and dust emissions, we need to address the failure of most GCMs to represent dust emissions due to the low mean and variance of grid-scale surface winds (Evan, 2018). To do so, two possibilities are to:

1. Modify the dust emission schemes of existing geochemical transport models to account for the subgrid scale distribution of wind speeds. This was done with

some success by (Ridley et al., 2013, 2014) who developed a scale-aware parameterization using a Weibull probability density function with MERRA reanalysis winds to drive the GEOS-Chem model. My suggestion here is to similarly modify the output of CMIP5 models to force GEOS-Chem with wind distributions derived from ensembles of simulations with and without anthropogenic aerosols, to assess the effect of the aerosols on dust emissions.

2. Downscale surface winds in the Sahel by running the regional climate configuration of the WRF model (Liang et al., 2012), which is shown to adequately represent precipitation variability in the Sahel (Kim et al., 2014), forced by CMIP5 simulation outputs with and without anthropogenic aerosols. This is a computationnally expensive option which would allow to obtain more resolved variability in near surface winds, to force a dust emission scheme.

I expect the results to confirm that the sulfate radiative forcing of the 70s and 80s caused a sufficiently large enhancement of dust production to explain most of the tropical North-Altantic PI decrease during that period. A caveat is that the methods suggested here cannot capture an eventual feedback of dust radiative forcing on dust production.

Bibliography

Ackerley, D., B. B. Booth, S. H. Knight, E. J. Highwood, D. J. Frame, M. R. Allen, and D. P. Rowell, 2011: Sensitivity of twentieth-century sahel rainfall to sulfate aerosol and co2 forcing. *Journal of Climate*, **24 (19)**, 4999–5014.

Allen, R. J., A. T. Evan, and B. B. Booth, 2015: Interhemispheric aerosol radiative forcing and tropical precipitation shifts during the late twentieth century. *Journal of Climate*, **28 (20)**, 8219–8246.

Ammann, C. M., and P. Naveau, 2003: Statistical analysis of tropical explosive volcanism occurrences over the last 6 centuries. *Geophysical Research Letters*, **30 (5)**.

Arakawa, A., and W. H. Schubert, 1974: Interaction of a cumulus cloud ensemble with the large-scale environment, part i. *Journal of the Atmospheric Sciences*, **31 (3)**, 674–701.

Bauer, S. E., and Coauthors, 2020: Historical (1850–2014) aerosol evolution and role on climate forcing using the giss modele2. 1 contribution to cmip6. *Journal of Advances in Modeling Earth Systems*, **12 (8)**, e2019MS001 978.

Becker, A., P. Finger, A. Meyer-Christoffer, B. Rudolf, K. Schamm, U. Schneider, and M. Ziese, 2013: A description of the global land-surface precipitation data products of the global precipitation climatology centre with sample applications including centennial (trend) analysis from 1901–present. *Earth System Science Data*, **5 (1)**, 71–99.

Bell, G. D., and Coauthors, 2000: Climate assessment for 1999. *Bulletin of the American Meteorological Society*, **81 (6)**, S1 – S50, doi:10.1175/1520-0477(2000)81[s1:CAF]2.0.CO;2, URL https://journals.ametsoc.org/view/journals/bams/81/6/1520-0477_2000_81_s1_caf_2_0_co_2.xml.

Bellomo, K., A. C. Clement, L. N. Murphy, L. M. Polvani, and M. A. Cane, 2016: New observational evidence for a positive cloud feedback that amplifies the atlantic multidecadal oscillation. *Geophysical Research Letters*, **43 (18)**, 9852–9859.

Bellomo, K., L. N. Murphy, M. A. Cane, A. C. Clement, and L. M. Polvani, 2018: Historical forcings as main drivers of the atlantic multidecadal variability in the cesm large ensemble. *Climate Dynamics*, **50 (9)**, 3687–3698.

Biagio, C. D., and Coauthors, 2017: Global scale variability of the mineral dust longwave refractive index: a new dataset of in situ measurements for climate modeling and remote sensing. *Atmospheric Chemistry and Physics*, **17 (3)**, 1901–1929.

Biasutti, M., 2011: Atmospheric science: A man-made drought. *Nature Climate Change*, **1 (4)**, 197.

Birkel, S. D., P. A. Mayewski, K. A. Maasch, A. V. Kurbatov, and B. Lyon, 2018: Evidence for a volcanic underpinning of the atlantic multidecadal oscillation. *NPJ Climate and Atmospheric Science*, **1 (1)**, 1–7.

Bister, M., and K. A. Emanuel, 1998: Dissipative heating and hurricane intensity. *Meteorology and Atmospheric Physics*, **65 (3-4)**, 233–240.

Bister, M., and K. A. Emanuel, 2002: Low frequency variability of tropical cyclone potential intensity 1. interannual to interdecadal variability. *Journal of Geophysical Research: Atmospheres*, **107 (D24)**.

Bony, S., and K. A. Emanuel, 2001: A parameterization of the cloudiness associated with cumulus convection; evaluation using toga coare data. *Journal of the atmospheric sciences*, **58 (21)**, 3158–3183.

Booth, B. B., N. J. Dunstone, P. R. Halloran, T. Andrews, and N. Bellouin, 2012: Aerosols implicated as a prime driver of twentieth-century north atlantic climate variability. *Nature*, **484 (7393)**, 228.

Bozlaker, A., J. M. Prospero, J. Price, and S. Chellam, 2018: Linking barbados mineral dust aerosols to north african sources using elemental composition and radiogenic sr, nd, and pb isotope signatures. *Journal of Geophysical Research: Atmospheres*, **123 (2)**, 1384–1400.

Brown, B. R., and G. J. Hakim, 2013: Variability and predictability of a three-dimensional hurricane in statistical equilibrium. *Journal of the Atmospheric Sciences*, **70 (6)**, 1806–1820.

Bryan, G. H., 2008: On the computation of pseudoadiabatic entropy and equivalent potential temperature. *Monthly Weather Review*, **136 (12)**, 5239–5245.

Bryan, G. H., 2012: Effects of surface exchange coefficients and turbulence length scales on the intensity and structure of numerically simulated hurricanes. *Monthly Weather Review*, **140 (4)**, 1125–1143.

Bryan, G. H., and J. M. Fritsch, 2002: A benchmark simulation for moist nonhydrostatic models. *Mon. Wea. Rev.*, **130**, 2917–2928.

Bryan, G. H., and R. Rotunno, 2009a: Evaluation of an analytical model for the maximum intensity of tropical cyclones. *Journal of the Atmospheric Sciences*, **66 (10)**, 3042–3060.

Bryan, G. H., and R. Rotunno, 2009b: The influence of near-surface, high-entropy air in hurricane eyes on maximum hurricane intensity. *Journal of the Atmospheric Sciences*, **66 (1)**, 148–158.

Bryan, G. H., and R. Rotunno, 2009c: The maximum intensity of tropical cyclones in axisymmetric numerical model simulations. *Monthly Weather Review*, **137 (6)**, 1770–1789.

Bu, Y. P., R. G. Fovell, and K. L. Corbosiero, 2014: Influence of cloud–radiative forcing on tropical cyclone structure. *Journal of the Atmospheric Sciences*, **71 (5)**, 1644–1662.

Chavas, D. R., and K. Emanuel, 2014: Equilibrium tropical cyclone size in an idealized state of axisymmetric radiative–convective equilibrium. *Journal of the Atmospheric Sciences*, **71 (5)**, 1663–1680.

Clement, A., K. Bellomo, L. N. Murphy, M. A. Cane, T. Mauritsen, G. Rädel, and B. Stevens, 2015: The atlantic multidecadal oscillation without a role for ocean circulation. *Science*, **350 (6258)**, 320–324.

Colarco, P. R., E. P. Nowottnick, C. A. Randles, B. Yi, P. Yang, K.-M. Kim, J. A. Smith, and C. G. Bardeen, 2014: Impact of radiatively interactive dust aerosols in the nasa geos-5 climate model: Sensitivity to dust particle shape and refractive index. *Journal of Geophysical Research: Atmospheres*, **119 (2)**, 753–786.

DeMaria, M., C. R. Sampson, J. A. Knaff, and K. Musgrave, 2014: Is tropical cyclone intensity guidance improving? *Bull. Amer. Meteor. Soc.*, **95**, 387–398.

Doherty, O. M., and A. T. Evan, 2014: Identification of a new dust-stratocumulus indirect effect over the tropical north atlantic. *Geophysical Research Letters*, **41 (19)**, 6935–6942.

Doherty, O. M., N. Riemer, and S. Hameed, 2014: Role of the convergence zone over west africa in controlling saharan mineral dust load and transport in the boreal summer. *Tellus B: Chemical and Physical Meteorology*, **66 (1)**, 23 191.

Donelan, M., B. K. Haus, N. Reul, W. Plant, M. Stiassnie, H. C. Graber, O. Brown, and E. Saltzman, 2004: On the limiting aerodynamic roughness of the ocean in very strong winds. *Geophysical Research Letters*, **31 (18)**.

Drennan, W. M., J. A. Zhang, J. R. French, C. McCormick, and P. G. Black, 2007: Turbulent fluxes in the hurricane boundary layer. part ii: Latent heat flux. *Journal of the atmospheric sciences*, **64 (4)**, 1103–1115.

Dubovik, O., and Coauthors, 2006: Application of spheroid models to account for aerosol particle nonsphericity in remote sensing of desert dust. *Journal of Geophysical Research: Atmospheres*, **111 (D11)**.

Dunion, J. P., and C. S. Velden, 2004: The impact of the saharan air layer on atlantic tropical cyclone activity. *Bulletin of the American Meteorological Society*, **85 (3)**, 353–366.

Dunstone, N., D. Smith, B. Booth, L. Hermanson, and R. Eade, 2013: Anthropogenic aerosol forcing of atlantic tropical storms. *Nature Geoscience*, **6 (7)**, 534.

Eliassen, A., and E. Kleinschmidt, 1957: Dynamic meteorology. *Geophysik II/Geophysics II*, Springer, 1–154.

Emanuel, K., 2000: A statistical analysis of tropical cyclone intensity. *Monthly Weather Review*, **128 (4)**, 1139–1152.

Emanuel, K., 2005: Increasing destructiveness of tropical cyclones over the past 30 years. *Nature*, **436 (7051)**, 686–688.

Emanuel, K., 2007: Environmental factors affecting tropical cyclone power dissipation. *Journal of Climate*, **20 (22)**, 5497–5509.

Emanuel, K., 2018: 100 years of progress in tropical cyclone research. *Meteorological Monographs*.

Emanuel, K., and D. S. Nolan, 2004: Tropical cyclone activity and the global climate system. *26th Conference on Hurricanes and Tropical Meteorolgy*.

Emanuel, K., and R. Rotunno, 2011: Self-stratification of tropical cyclone outflow. part i: Implications for storm structure. *Journal of the Atmospheric Sciences*, **68 (10)**, 2236–2249.

Emanuel, K., and R. Rousseau-Rizzi, 2020: Reply to "comments on 'an evaluation of hurricane superintensity in axisymmetric numerical models'". *Journal of Atmospheric Sciences*, **77 (11)**, 3977–3980.

Emanuel, K., and A. Sobel, 2013: Response of tropical sea surface temperature, precipitation, and tropical cyclone-related variables to changes in global and local forcing. *Journal of Advances in Modeling Earth Systems*, **5 (2)**, 447–458.

Emanuel, K. A., 1986: An air-sea interaction theory for tropical cyclones. part i: Steady-state maintenance. *Journal of the Atmospheric Sciences*, **43 (6)**, 585–605.

Emanuel, K. A., 1988: The maximum intensity of hurricanes. *Journal of the Atmospheric Sciences*, **45 (7)**, 1143–1155.

Emanuel, K. A., 1994: *Atmospheric Convection*. Oxford University Press, 580 pp.

Emanuel, K. A., 2017: Will global warming make hurricane forecasting more difficult? *Bull. Amer. Meteor. Soc.*, **98**, 495–501.

Emanuel, K. A., and M. Živković-Rothman, 1999: Development and evaluation of a convection scheme for use in climate models. *Journal of the Atmospheric Sciences*, **56 (11)**, 1766–1782.

Evan, A., 2018: Surface winds and dust biases in climate models. *Geophysical Research Letters*, **45 (2)**, 1079–1085.

Evan, A. T., R. J. Allen, R. Bennartz, and D. J. Vimont, 2013: The modification of sea surface temperature anomaly linear damping time scales by stratocumulus clouds. *Journal of Climate*, **26 (11)**, 3619–3630.

Evan, A. T., C. Flamant, S. Fiedler, and O. Doherty, 2014: An analysis of aeolian dust in climate models. *Geophysical Research Letters*, **41 (16)**, 5996–6001.

Evan, A. T., C. Flamant, M. Gaetani, and F. Guichard, 2016: The past, present and future of african dust. *Nature*, **531 (7595)**, 493.

Evan, A. T., G. R. Foltz, D. Zhang, and D. J. Vimont, 2011: Influence of african dust on ocean–atmosphere variability in the tropical atlantic. *Nature Geoscience*, **4 (11)**, 762.

Evan, A. T., and S. Mukhopadhyay, 2010: African dust over the northern tropical atlantic: 1955–2008. *Journal of Applied Meteorology and Climatology*, **49 (11)**, 2213–2229.

Fairall, C., E. F. Bradley, J. Hare, A. Grachev, and J. Edson, 2003: Bulk parameterization of air–sea fluxes: Updates and verification for the coare algorithm. *Journal of climate*, **16 (4)**, 571–591.

Fouquart, Y., and Coauthors, 1980: Computations of solar heating of the earth's atmosphere: A new parameterization.

Frisius, T., 2015: What controls the size of a tropical cyclone? investigations with an axisymmetric model. *Quarterly Journal of the Royal Meteorological Society*, **141 (691)**, 2457–2470.

Giannini, A., and A. Kaplan, 2019: The role of aerosols and greenhouse gases in sahel drought and recovery. *Climatic change*, **152 (3)**, 449–466.

Giannini, A., R. Saravanan, and P. Chang, 2003: Oceanic forcing of sahel rainfall on interannual to interdecadal time scales. *Science*, **302 (5647)**, 1027–1030.

Gilford, D. M., 2020: pypi (v1. 3): Tropical cyclone potential intensity calculations in python. *Geoscientific Model Development Discussions*, 1–30.

Grist, J. P., and S. E. Nicholson, 2001: A study of the dynamic factors influencing the rainfall variability in the west african sahel. *Journal of climate*, **14 (7)**, 1337–1359.

Hakim, G. J., 2011: The mean state of axisymmetric hurricanes in statistical equilibrium. *Journal of the Atmospheric Sciences*, **68 (6)**, 1364–1376.

Hausman, S. A., 2001: Formulation and sensitivity analysis of a nonhydrostatic, axisymmetric tropical cyclone model. Tech. rep., Air Force Institute Of Technology Wright-Patterson OH.

Haywood, J. M., A. Jones, N. Bellouin, and D. Stephenson, 2013: Asymmetric forcing from stratospheric aerosols impacts sahelian rainfall. *Nature Climate Change*, **3 (7)**, 660–665.

Held, I., T. Delworth, J. Lu, K. u. Findell, and T. Knutson, 2005: Simulation of sahel drought in the 20th and 21st centuries. *Proceedings of the National Academy of Sciences*, **102 (50)**, 17 891–17 896.

Hersbach, H., and Coauthors, 2020: The era5 global reanalysis. *Quarterly Journal of the Royal Meteorological Society*, **146 (730)**, 1999–2049.

Hill, S. A., Y. Ming, I. M. Held, and M. Zhao, 2017: A moist static energy budget–based analysis of the sahel rainfall response to uniform oceanic warming. *Journal of Climate*, **30 (15)**, 5637–5660.

Hill, S. A., Y. Ming, and M. Zhao, 2018: Robust responses of the sahelian hydrological cycle to global warming. *Journal of Climate*, **31 (24)**, 9793–9814.

Hoesly, R. M., and Coauthors, 2018: Historical (1750-2014) anthropogenic emissions of reactive gases and aerosols from the community emission data system (ceds). *Geoscientific Model Development*, **11**, 369–408.

Houze Jr, R. A., 2010: Clouds in tropical cyclones. *Monthly Weather Review*, **138 (2)**, 293–344.

Jeevanjee, N., and D. M. Romps, 2018: Mean precipitation change from a deepening troposphere. *Proceedings of the National Academy of Sciences*, **115 (45)**, 11 465–11 470.

Jordan, A. K., A. Gnanadesikan, and B. Zaitchik, 2018: Simulated dust aerosol impacts on western sahelian rainfall: Importance of ocean coupling. *Journal of Climate*, **(2018)**.

Kallos, G., M. Astitha, P. Katsafados, and C. Spyrou, 2007: Long-range transport of anthropogenically and naturally produced particulate matter in the mediterranean and north atlantic: Current state of knowledge. *Journal of Applied Meteorology and Climatology*, **46 (8)**, 1230–1251.

Kepert, J. D., 2006: Observed boundary layer wind structure and balance in the hurricane core. part ii: Hurricane mitch. *Journal of the atmospheric sciences*, **63 (9)**, 2194–2211.

Kim, J., and Coauthors, 2014: Evaluation of the cordex-africa multi-rcm hindcast: systematic model errors. *Climate dynamics*, **42 (5)**, 1189–1202.

Knaff, J. A., J. P. Kossin, and M. DeMaria, 2003: Annular hurricanes. *Weather and Forecasting*, **18 (2)**, 204–223.

Knapp, K. R., M. C. Kruk, D. H. Levinson, H. J. Diamond, and C. J. Neumann, 2010: The international best track archive for climate stewardship (ibtracs) unifying tropical cyclone data. *Bulletin of the American Meteorological Society*, **91 (3)**, 363–376.

Knutson, T. R., and Coauthors, 2010: Tropical cyclones and climate change. *Nature geoscience*, **3 (3)**, 157–163.

Kok, J. F., and Coauthors, 2017: Smaller desert dust cooling effect estimated from analysis of dust size and abundance. *Nature Geoscience*, **10 (4)**, 274.

Kossin, J. P., K. A. Emanuel, and G. A. Vecchi, 2014: The poleward migration of the location of tropical cyclone maximum intensity. *Nature*, **509 (7500)**, 349–352.

Kuciauskas, A. P., P. Xian, E. J. Hyer, M. I. Oyola, and J. R. Campbell, 2018: Supporting weather forecasters in predicting and monitoring saharan air layer dust events as they impact the greater caribbean. *Bulletin of the American Meteorological Society*, **99 (2)**, 259–268.

Kutzbach, J. E., and Z. Liu, 1997: Response of the african monsoon to orbital forcing and ocean feedbacks in the middle holocene. *Science*, **278 (5337)**, 440–443.

Lelieveld, J., and Coauthors, 2002: Global air pollution crossroads over the mediterranean. *Science*, **298 (5594)**, 794–799.

Li, X., H. Maring, D. Savoie, K. Voss, and J. Prospero, 1996: Dominance of mineral dust in aerosol light-scattering in the north atlantic trade winds. *Nature*, **380 (6573)**, 416.

Li-Jones, X., and J. Prospero, 1998: Variations in the size distribution of non-sea-salt sulfate aerosol in the marine boundary layer at barbados: Impact of african dust. *Journal of Geophysical Research: Atmospheres*, **103 (D13)**, 16 073–16 084.

Liang, X.-Z., and Coauthors, 2012: Regional climate–weather research and forecasting model. *Bulletin of the American Meteorological Society*, **93 (9)**, 1363–1387.

Lilly, D. K., unpublished manuscript: A steady-state hurricane model.

Mahowald, N. M., and Coauthors, 2010: Observed 20th century desert dust variability: impact on climate and biogeochemistry. *Atmospheric Chemistry and Physics*, **10 (22)**, 10 875–10 893.

Manabe, S., and R. F. Strickler, 1964: Thermal equilibrium of the atmosphere with a convective adjustment. *Journal of the Atmospheric Sciences*, **21 (4)**, 361–385.

Mann, M. E., and K. A. Emanuel, 2006: Atlantic hurricane trends linked to climate change. *Eos, Transactions American Geophysical Union*, **87 (24)**, 233–241.

Mann, M. E., B. A. Steinman, D. J. Brouillette, and S. K. Miller, 2021: Multidecadal climate oscillations during the past millennium driven by volcanic forcing. *Science*, **371 (6533)**, 1014–1019.

Mann, M. E., B. A. Steinman, and S. K. Miller, 2020: Absence of internal multidecadal and interdecadal oscillations in climate model simulations. *Nature communications*, **11 (1)**, 1–9.

Marmer, E., B. Langmann, H. Fagerli, and V. Vestreng, 2007: Direct shortwave radiative forcing of sulfate aerosol over europe from 1900 to 2000. *Journal of Geophysical Research: Atmospheres*, **112 (D23)**.

Martin, E. R., C. Thorncroft, and B. B. Booth, 2014: The multidecadal atlantic sst sahel rainfall teleconnection in cmip5 simulations. *Journal of Climate*, **27 (2)**, 784–806.

Miller, R., and I. Tegen, 1998: Climate response to soil dust aerosols. *Journal of climate*, **11 (12)**, 3247–3267.

Miller, R. L., and Coauthors, 2021: Cmip6 historical simulations (1850–2014) with giss-e2. 1. *Journal of Advances in Modeling Earth Systems*, **13 (1)**, e2019MS002 034.

Mitchell, T., 2013: Sahel precipitation index. *Joint Institute for the Study of the Atmosphere and Ocean, Univ. of Washington, doi*, **10**, H5MW2F2Q.

Montgomery, M. T., M. M. Bell, S. D. Aberson, and M. L. Black, 2006: Hurricane isabel (2003): New insights into the physics of intense storms. part i: Mean vortex structure and maximum intensity estimates. *Bulletin of the American Meteorological Society*, **87 (10)**, 1335–1348.

Morcrette, J.-J., 1991: Radiation and cloud radiative properties in the european centre for medium range weather forecasts forecasting system. *Journal of Geophysical Research: Atmospheres*, **96 (D5)**, 9121–9132.

Murphy, L. N., K. Bellomo, M. Cane, and A. Clement, 2017: The role of historical forcings in simulating the observed atlantic multidecadal oscillation. *Geophysical Research Letters*, **44 (5)**, 2472–2480.

Mylona, S., 1996: Sulphur dioxide emissions in europe 1880–1991 and their effect on sulphur concentrations and depositions. *Tellus B*, **48 (5)**, 662–689.

Newell, R. E., and J. W. Kidson, 1984: African mean wind changes between sahelian wet and dry periods. *Journal of Climatology*, **4 (1)**, 27–33.

Nicholson, S. E., 2009: A revised picture of the structure of the "monsoon" and land itcz over west africa. *Climate Dynamics*, **32 (7)**, 1155–1171, doi:10.1007/s00382-008-0514-3, URL https://doi.org/10.1007/s00382-008-0514-3.

Nicholson, S. E., A. K. Dezfuli, and D. Klotter, 2012: A two-century precipitation dataset for the continent of africa. *Bulletin of the American Meteorological Society*, **93 (8)**, 1219–1231.

Office For Coastal Management, 2018: Assessing the u.s. climate in 2017. Tech. rep. [Available online at https://www.ncei.noaa.gov/news/national-climate-201712.].

O'Gorman, P. A., and T. Schneider, 2008: The hydrological cycle over a wide range of climates simulated with an idealized gcm. *Journal of Climate*, **21 (15)**, 3815–3832.

Pauluis, O. M., and F. Zhang, 2017: Reconstruction of thermodynamic cycles in a high-resolution simulation of a hurricane. *Journal of the Atmospheric Sciences*, **74 (10)**, 3367–3381.

Pausata, F. S., K. A. Emanuel, M. Chiacchio, G. T. Diro, Q. Zhang, L. Sushama, J. C. Stager, and J. P. Donnelly, 2017: Tropical cyclone activity enhanced by sahara greening and reduced dust emissions during the african humid period. *Proceedings of the National Academy of Sciences*, **114 (24)**, 6221–6226.

Pausata, F. S., G. Messori, and Q. Zhang, 2016: Impacts of dust reduction on the northward expansion of the african monsoon during the green sahara period. *Earth and Planetary Science Letters*, **434**, 298–307.

Persing, J., and M. T. Montgomery, 2003: Hurricane superintensity. *Journal of the atmospheric sciences*, **60 (19)**, 2349–2371.

Persing, J., M. T. Montgomery, R. K. Smith, and J. C. McWilliams, 2019: Quasi steady-state hurricanes revisited. *Tropical Cyclone Research and Review*, **8 (1)**, 1–17.

Preunkert, S., M. Legrand, and D. Wagenbach, 2001: Sulfate trends in a col du dome (french alps) ice core: A record of anthropogenic sulfate levels in the european midtroposphere over the twentieth century. *Journal of Geophysical Research: Atmospheres*, **106 (D23)**, 31 991–32 004.

Prospero, J. M., 2015: Characterizing the temporal and spatial variability of african dust over the atlantic. *DUST*, **24**, 68.

Prospero, J. M., and T. N. Carlson, 1972: Vertical and areal distribution of saharan dust over the western equatorial north atlantic ocean. *Journal of Geophysical Research*, **77 (27)**, 5255–5265.

Prospero, J. M., F.-X. Collard, J. Molinié, and A. Jeannot, 2014: Characterizing the annual cycle of african dust transport to the caribbean basin and south america and its impact on the environment and air quality. *Global Biogeochemical Cycles*, **28 (7)**, 757–773.

Prospero, J. M., and P. J. Lamb, 2003: African droughts and dust transport to the caribbean: Climate change implications. *Science*, **302 (5647)**, 1024–1027.

Ramsay, H. A., and A. H. Sobel, 2011: Effects of relative and absolute sea surface temperature on tropical cyclone potential intensity using a single-column model. *Journal of Climate*, **24 (1)**, 183–193.

Rayner, N., D. E. Parker, E. Horton, C. K. Folland, L. V. Alexander, D. Rowell, E. Kent, and A. Kaplan, 2003: Global analyses of sea surface temperature, sea ice, and night marine air temperature since the late nineteenth century. *Journal of Geophysical Research: Atmospheres*, **108 (D14)**.

Ridley, D., C. Heald, and J. Prospero, 2014: What controls the recent changes in african mineral dust aerosol across the atlantic? *Atmospheric Chemistry and Physics*, **14 (11)**, 5735–5747.

Ridley, D. A., C. L. Heald, J. Pierce, and M. Evans, 2013: Toward resolution-independent dust emissions in global models: Impacts on the seasonal and spatial distribution of dust. *Geophysical Research Letters*, **40 (11)**, 2873–2877.

Rotstayn, L. D., and U. Lohmann, 2002: Tropical rainfall trends and the indirect aerosol effect. *Journal of Climate*, **15 (15)**, 2103–2116.

Rotunno, R., and G. H. Bryan, 2012: Effects of parameterized diffusion on simulated hurricanes. *Journal of the Atmospheric Sciences*, **69 (7)**, 2284–2299.

Rotunno, R., Y. Chen, W. Wang, C. Davis, J. Dudhia, and G. Holland, 2009: Large-eddy simulation of an idealized tropical cyclone. *Bulletin of the American Meteorological Society*, **90 (12)**, 1783–1788.

Rotunno, R., and K. A. Emanuel, 1987: An air–sea interaction theory for tropical cyclones. part ii: Evolutionary study using a nonhydrostatic axisymmetric numerical model. *Journal of the Atmospheric Sciences*, **44 (3)**, 542–561.

Rousseau-Rizzi, R., and K. Emanuel, 2019: An evaluation of hurricane superintensity in axisymmetric numerical models. *Journal of the Atmospheric Sciences*, **76 (6)**, 1697–1708.

Rousseau-Rizzi, R., and K. Emanuel, 2020: Reply to "comments on 'an evaluation of hurricane superintensity in axisymmetric numerical models'". *Journal of the Atmospheric Sciences*, **77 (5)**, 1893–1896.

Rousseau-Rizzi, R., and K. Emanuel, In review: A weak temperature gradient framework to quantify the causes of potential intensity variability in the tropics. *Journal of Climate*.

Rousseau-Rizzi, R., R. Rotunno, and G. Bryan, 2021: A thermodynamic perspective on steady-state tropical cyclones. *Journal of the Atmospheric Sciences*, **78 (2)**, 583–593.

Ryder, C., E. Highwood, T. Lai, H. Sodemann, and J. H. Marsham, 2013a: Impact of atmospheric transport on the evolution of microphysical and optical properties of saharan dust. *Geophysical Research Letters*, **40 (10)**, 2433–2438.

Ryder, C. L., and Coauthors, 2013b: Optical properties of saharan dust aerosol and contribution from the coarse mode as measured during the fennec 2011 aircraft campaign. *Atmospheric Chemistry and Physics*, **13 (1)**, 303–325.

Si, D., D. Jiang, and H. Wang, 2020: Intensification of the atlantic multidecadal variability since 1870: implications and possible causes. *Journal of Geophysical Research: Atmospheres*, **125 (11)**, e2019JD030 977.

Smagorinsky, J., 1963: General circulation experiments with the primitive equations: I. the basic experiment. *Monthly weather review*, **91 (3)**, 99–164.

Smith, R. K., M. T. Montgomery, and J. Persing, 2014: On steady-state tropical cyclones. *Quarterly Journal of the Royal Meteorological Society*, **140 (685)**, 2638–2649.

Smith, S. J., J. v. Aardenne, Z. Klimont, R. J. Andres, A. Volke, and S. Delgado Arias, 2011: Anthropogenic sulfur dioxide emissions: 1850–2005. *Atmospheric Chemistry and Physics*, **11 (3)**, 1101–1116.

Sobel, A. H., and C. S. Bretherton, 2000: Modeling tropical precipitation in a single column. *Journal of climate*, **13 (24)**, 4378–4392.

Sobel, A. H., S. J. Camargo, and M. Previdi, 2019: Aerosol versus greenhouse gas effects on tropical cyclone potential intensity and the hydrologic cycle. *Journal of Climate*, **32 (17)**, 5511–5527.

Song, Q., Z. Zhang, H. Yu, S. Kato, P. Yang, P. Colarco, L. A. Remer, and C. L. Ryder, 2018: Net radiative effects of dust in the tropical north atlantic based on integrated satellite observations and in situ measurements. *Atmospheric Chemistry and Physics*, **18 (15)**, 11 303–11 322.

Strong, J. D., G. A. Vecchi, and P. Ginoux, 2015: The response of the tropical atlantic and west african climate to saharan dust in a fully coupled gcm. *Journal of Climate*, **28 (18)**, 7071–7092.

Strong, J. D., G. A. Vecchi, and P. Ginoux, 2018: The climatological effect of saharan dust on global tropical cyclones in a fully coupled gcm. *Journal of Geophysical Research: Atmospheres*, **123 (10)**, 5538–5559.

Tang, B., and K. Emanuel, 2012: Sensitivity of tropical cyclone intensity to ventilation in an axisymmetric model. *Journal of the Atmospheric Sciences*, **69 (8)**, 2394–2413.

Thomason, L. W., and Coauthors, 2018: A global space-based stratospheric aerosol climatology: 1979–2016. *Earth System Science Data*, **10 (1)**, 469–492.

Tierney, J. E., F. S. Pausata, and P. B. deMenocal, 2017: Rainfall regimes of the green sahara. *Science advances*, **3 (1)**, e1601 503.

Ting, M., Y. Kushnir, R. Seager, and C. Li, 2009: Forced and internal twentieth-century sst trends in the north atlantic. *Journal of Climate*, **22 (6)**, 1469–1481.

Trenberth, K. E., and A. Dai, 2007: Effects of mount pinatubo volcanic eruption on the hydrological cycle as an analog of geoengineering. *Geophysical Research Letters*, **34 (15)**.

Trenberth, K. E., and D. J. Shea, 2006: Atlantic hurricanes and natural variability in 2005. *Geophysical research letters*, **33 (12)**.

Twohy, C. H., and Coauthors, 2009: Saharan dust particles nucleate droplets in eastern atlantic clouds. *Geophysical Research Letters*, **36 (1)**.

Vecchi, G. A., and B. J. Soden, 2007: Effect of remote sea surface temperature change on tropical cyclone potential intensity. *Nature*, **450 (7172)**, 1066–1070.

Villarini, G., and G. A. Vecchi, 2012: North atlantic power dissipation index (pdi) and accumulated cyclone energy (ace): Statistical modeling and sensitivity to sea surface temperature changes. *Journal of climate*, **25 (2)**, 625–637.

Villarini, G., and G. A. Vecchi, 2013: Projected increases in north atlantic tropical cyclone intensity from cmip5 models. *Journal of Climate*, **26 (10)**, 3231–3240.

Wang, C., S. Dong, A. T. Evan, G. R. Foltz, and S.-K. Lee, 2012: Multidecadal covariability of north atlantic sea surface temperature, african dust, sahel rainfall, and atlantic hurricanes. *Journal of Climate*, **25 (15)**, 5404–5415.

Wang, W., A. T. Evan, C. Flamant, and C. Lavaysse, 2015: On the decadal scale correlation between african dust and sahel rainfall: The role of saharan heat low–forced winds. *Science advances*, **1 (9)**, e1500 646.

Westervelt, D., and Coauthors, 2017: Multimodel precipitation responses to removal of us sulfur dioxide emissions. *Journal of Geophysical Research: Atmospheres*, **122 (9)**, 5024–5038.

Westervelt, D. M., and Coauthors, 2018: Connecting regional aerosol emissions reductions to local and remote precipitation responses. *Atmospheric Chemistry and Physics*, **18 (16)**, 12 461–12 475.

Wicker, L. J., and W. C. Skamarock, 2002: Time splitting methods for elastic models using forward time schemes. *Mon. Wea. Rev.*, **130**, 2088–2097.

Williams, R. H., and Coauthors, 2016: Glacial to holocene changes in trans-atlantic saharan dust transport and dust-climate feedbacks. *Science advances*, **2 (11)**, e1600 445.

Willoughby, H. E., 1990: Gradient balance in tropical cyclones. *Journal of the Atmospheric Sciences*, **47 (2)**, 265–274.

Wills, R. C., K. C. Armour, D. S. Battisti, and D. L. Hartmann, 2019: Ocean–atmosphere dynamical coupling fundamental to the atlantic multidecadal oscillation. *Journal of Climate*, **32 (1)**, 251–272.

Wills, R. C., T. Schneider, J. M. Wallace, D. S. Battisti, and D. L. Hartmann, 2018: Disentangling global warming, multidecadal variability, and el niño in pacific temperatures. *Geophysical Research Letters*, **45 (5)**, 2487–2496.

Wing, A. A., K. Emanuel, and S. Solomon, 2015: On the factors affecting trends and variability in tropical cyclone potential intensity. *Geophysical Research Letters*, **42 (20)**, 8669–8677.

Xue, Y., and Coauthors, 2016: West african monsoon decadal variability and surface-related forcings: second west african monsoon modeling and evaluation project experiment (wamme ii). *Climate dynamics*, **47 (11)**, 3517–3545.

Yang, B., Y. Wang, and B. Wang, 2007: The effect of internally generated inner-core asymmetries on tropical cyclone potential intensity. *Journal of the atmospheric sciences*, **64 (4)**, 1165–1188.

Yu, K., P. D'Odorico, A. Bhattachan, G. S. Okin, and A. T. Evan, 2015: Dust-rainfall feedback in west african sahel. *Geophysical Research Letters*, **42 (18)**, 7563–7571.

Zeng, N., 2003: Drought in the sahel. *Science*, **302 (5647)**, 999–1000.

Zhang, R., and T. L. Delworth, 2006: Impact of atlantic multidecadal oscillations on india/sahel rainfall and atlantic hurricanes. *Geophysical Research Letters*, **33 (17)**.

Zhang, R., and Coauthors, 2013: Have aerosols caused the observed atlantic multidecadal variability? *Journal of the Atmospheric Sciences*, **70 (4)**, 1135–1144.

Zhou, M., H. Yu, R. Dickinson, O. Dubovik, and B. Holben, 2005: A normalized description of the direct effect of key aerosol types on solar radiation as estimated from aerosol robotic network aerosols and moderate resolution imaging spectroradiometer albedos. *Journal of Geophysical Research: Atmospheres*, **110 (D19)**.